Earth-Science Reviews 272 (2026) 105322

Contents lists available at ScienceDirect

Earth-Science Reviews

journal homepage: www.elsevier.com/locate/earscirev

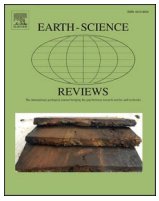

Review Article

Regimes of bedforms created by down-slope density currents

Octavio E. Sequeiros [a,*], Benoit Spinewine [b,c], Gary Parker [d,e], Carlos Pirmez [f], Enrica Viparelli [g,h], Juan J. Fedele [i], Marcelo H. García [d], Débora Koller [j], Michele Bolla Pittaluga [k], Miwa Yokokawa [l]

[a] Shell Global Solutions International B.V., Carel van Bylandtlaan 30, 2596 HR The Hague, The Netherlands
[b] Fugro Belgium SRL, Rue du Bosquet 9, 1348 Louvain-la-Neuve, Belgium
[c] Dept. Civil & Environnemental Engineering, Université catholique de Louvain, Place du Levant 1, 1348 Louvain-la-Neuve, Belgium
[d] Dept. of Civil and Environmental Engineering, University of Illinois, 205 N Mathews Ave, Urbana, IL 61081, USA
[e] Dept. of Geology, University of Illinois, 1301 W Green St, Urbana, IL 61801, USA
[f] Weather Water Sand, Via Montallegro 1, Genova, GE 16145, Italy
[g] Dipartimento di Scienze della Terra, dell'Ambiente e delle Risorse, Università degli Studi di Napoli Federico II, Via Vicinale Cupa Cinthia 21, 80126 Naples, Italy
[h] Dept. of Civil and Environmental Engineering, University of South Carolina, 300 Main Street, Columbia, SC 29208, USA
[i] Exploration & New Ventures ExxonMobil Houston Campus, 22777 Springwoods Village Parkway Spring, TX, 77389, USA
[j] Instituto de Pesquisas Hidráulicas - Universidade Federal do Rio Grande do Sul, Bento Gonçalves Avenue, 9500, 91501-970 Porto Alegre, RS, Brazil.
[k] Dept. of Civil, Chemical and Environmental Engineering, Università di Genova, Via Montallegro 1, Genova, GE 16145, Italy.
[l] Faculty of Information Science and Technology, Osaka Institute of Technology, 1-79-1 Kitayama, Hirakata, Osaka 576-0196, Japan

ARTICLE INFO

Keywords:
Bedform classification
Density current
Turbidity current
Dune
Antidune
Ripple
Cyclic step
River
Submarine canyon
Continental slope
Levee
Fan
Sediment wave
Sediment transport
Fluid mechanics
Subaqueous bedform

ABSTRACT

Bedforms in rivers have been extensively studied for decades. Turbidite outcrops also display bedforms emplaced subaqueously by turbidity currents. Recent breakthroughs in the attainable resolution of deep underwater bathymetric/seismic mapping have revealed that bedforms in submarine environments may be as widespread and diverse as those associated with fluvial flows. Turbidity currents that emplace subaqueous bedforms run down submarine canyons, traverse and overflow leveed channels on submarine fans, or manifest themselves as sheet turbidity currents along continental margins. Submarine bedforms present features that appear to be analogous to their fluvial counterparts. Submarine bedforms have traditionally been interpreted with the use of tools, and in particular phase diagrams, that were developed solely for fluvial bedforms. The use of such tools is motivated by the fact that simultaneous observation of the bedforms as they evolve in the field and the turbidity currents that create them remains at the edge of present capabilities. We fill this gap in part with a technique that has been successfully implemented for fluvial bedforms, i.e. experimentation. We present observations of bedforms emplaced by saline and turbidity currents in laboratory flumes. The experimental flows span a wide range of densimetric Froude numbers, including both subcritical and supercritical regimes, and produced various bedform types including subcritical and supercritical-regime ripples/dunes, upstream-migrating and downstream-migrating antidunes, and cyclic steps. We have gathered a comprehensive set of fluvial and submarine field bedforms worldwide from multiple environments including submarine canyons, levees, slopes, and fans; some of which include associated flow observations. The data are summarized in a set of bedform dimensions and regime diagrams, which are applicable to saline and/or turbidity currents, and generally to any down-slope moving bottom flow. The regimes for submarine bedforms show both similarities and differences with fluvial regimes. Our diagrams and guidelines constitute a new tool for the interpretation of field-scale bedforms generated by turbidity currents.

* Corresponding author at: Shell Global Solutions International B.V, Carel van Bylandtlaan 30, 2596 HR The Hague, The Netherlands
E-mail address: octavio.e.sequeiros@shell.com (O.E. Sequeiros).

https://doi.org/10.1016/j.earscirev.2025.105322
Received 12 March 2025; Received in revised form 3 November 2025; Accepted 4 November 2025
Available online 11 November 2025

Contents

1. Introduction . . . 2
   1.1. Background . . . 2
   1.2. Rationale . . . 3
   1.3. Scope . . . 4
2. Fluvial bedforms . . . 4
   2.1. Bedform types . . . 4
   2.2. Bedforms in subcritical regime . . . 4
   2.3. Bedforms in supercritical regime . . . 5
   2.4. Lower and upper plane bed regimes . . . 5
   2.5. Bedform regime diagrams . . . 6
3. Data compendium . . . 6
   3.1. Froude and wavenumber . . . 6
   3.2. Dimensionless grain size . . . 7
   3.3. Bed shear stress and Shields number . . . 7
   3.4. Bedform characteristics . . . 8
   3.5. Uncertainty assessment . . . 8
4. Experimental density current bedforms . . . 8
   4.1. Ripples . . . 8
   4.2. Dunes . . . 9
   4.3. Supercritical-regime ripples and dunes, downstream-migrating antidunes . . . 9
   4.4. Upstream-migrating antidunes . . . 11
   4.5. Cyclic steps . . . 12
   4.6. Lower and upper plane bed regimes . . . 12
5. Bedform classification . . . 13
   5.1. Bedform dimension diagrams . . . 13
   5.2. Regime diagrams . . . 14
   5.3. Dimensionless flowless diagrams . . . 16
6. Field-scale density current bedforms . . . 16
   6.1. Locations and settings . . . 16
   6.2. Estimation criteria . . . 17
   6.3. Cyclic steps . . . 19
   6.4. Upstream migrating antidunes . . . 24
   6.5. Downstream migrating antidunes . . . 25
   6.6. Supercritical-regime dunes . . . 25
   6.7. Dunes . . . 25
7. Discussion . . . 26
   7.1. Terminology: bedforms, sediment waves, gravel-, sand-, and mudwaves . . . 26
   7.2. Fluvial and submarine bedforms biases . . . 27
   7.3. Total or basal Froude number? . . . 28
   7.4. Flow control . . . 28
   7.5. Slope control . . . 30
   7.6. Grain size control . . . 32
   7.7. Ripples or dunes? . . . 32
   7.8. Ripples and dunes in supercritical regime? . . . 32
   7.9. Cyclic steps or upstream migrating antidunes? . . . 33
   7.10. When antidunes become cyclic steps . . . 34
   7.11. Upstream or downstream migrating antidunes? . . . 34
   7.12. Downstream migrating antidunes or supercritical-regime dunes? . . . 35
   7.13. Bedform development and transition . . . 35
   7.14. Migration direction and concavity of bedforms . . . 36
   7.15. Bedload and suspended load . . . 36
   7.16. What has been excluded . . . 36
8. Conclusions . . . 37
   Declaration of competing interest . . . 38
   Acknowledgments . . . 38
   Supplementary data . . . 38
   Data availability . . . 38
   References . . . 38

1. Introduction

1.1. Background

Alluvial river flows sculpt a wide variety of sedimentary bedforms. These bedforms are in some cases optically observable in the field as they interact with the flow (e.g., Mohrig and Smith, 1996) and can often be imaged using acoustic techniques such as multibeam sonar (e.g., Parsons et al., 2005; Best, 2005; Nittrouer et al., 2008). They can also be created and studied in the laboratory under controlled conditions (e.g., Gilbert, 1914; Guy et al., 1966; Coleman and Melville, 1994; Coleman et al., 2003).

A free-surface or open-channel flow can be a river or a flume. We use the encompassing term “fluvial” to refer to these flows. Laboratory data

on fluvial bedforms have been used to construct phase diagrams that indicate regimes for and/or characteristics of each type of bedform or bed state (e.g., Vanoni, 1974; Middleton and Southard, 1984). These regime diagrams and related bedform predictors have been extended using field data (e.g., van den Berg and van Gelder, 1993; Julien and Klaassen, 1995). They have proved valuable for the reconstruction of paleoflows from the sedimentary structures observed in cores and outcrops, where the bedforms can be identified but little direct information is available about the flows that created them (e.g., Middleton and Southard, 1984; Southard and Boguchwal, 1990; Ashley, 1990).

In the laboratory, turbidity currents and saline underflows passing over erodible beds appear to be capable of producing all the bedform types seen in rivers (e.g., García and Parker, 1993; Parker et al., 1987; Imran et al., 2002; Kostic and Parker, 2003; Straub et al., 2008; Sequeiros et al., 2009, 2010a, 2010b, 2018; Spinewine et al., 2009, 2010; Fedele and García, 2009; Fedele et al., 2009, 2011, 2016; Koller, 2020; Koller et al., 2017, 2019, 2022; de Cala et al., 2020; Ono et al., 2023; Ohata et al., 2023; Maggi et al., 2024).

Contemporaneous field observations of turbidity currents and associated bedforms, however, are recent, rare, and only in a few cases observed strictly at the same time (e.g., Monterey Canyon: Xu et al., 2004, 2008, 2014; Xu, 2010; Paull et al., 2010, 2011; Squamish Prodelta: Hughes Clarke, 2016; Hage et al., 2018; Fraser Delta: Hill, 2012; Lintern et al., 2016; Hill and Lintern, 2022; Bute Inlet: Zeng et al., 1991, Heijnen et al., 2020, Chen et al., 2021). Although bedforms associated with turbidity currents have been observed in laboratory studies as well as the field, the delineation of regime diagrams equivalent to those available for fluvial bedforms has remained elusive. As a result, researchers have had to rely on the direct application of results from the fluvial setting, including phase diagrams, assuming that the flow parameters are equivalent, to interpret paleoflow characteristics from the structure of turbidite outcrops (e.g., Komar, 1985; Allen, 1991; Endo and Masuda, 1997; Baas et al., 2000; Xu et al., 2008). The basis for this application consists of plausible analogies which are nevertheless lacking in specific physical justification. Indeed, Komar (1985) made the following observation: "There is the possibility that the bedform phase diagrams such as Allen (1982) are inappropriate to the present analysis of turbidites." Relatively little has been done since then to remedy this state of affairs, the main exceptions being Cartigny et al. (2014), and Fedele et al. (2016). Fedele et al. (2016) highlighted the existence of supercritical-regime dunes, a type of bedform observed in flume density currents that is rather elusive in fluvial flows.

1.2. Rationale

The present study represents an attempt to systematically investigate the flow parameters associated with the formation of bedforms under density and turbidity currents and address the lack of dedicated diagrams that can be used to evaluate bedforms under these types of flows. We report experimental results on bedforms created in the laboratory by bottom density flows moving over erodible beds composed of different types of loose non-cohesive sediment. Most of the density flows under consideration were saline flows, but some of them were hybrid saline-turbidity and pure turbidity currents. We used saline underflows as surrogates for turbidity currents driven by fine mud flowing over a coarser, non-cohesive bed. The dataset is based on studies by García and Parker (1993), Spinewine et al. (2009, 2010), Sequeiros et al. (2010a, 2010b, 2018), Fedele et al. (2016), Koller et al. (2017, 2019, 2022), de Cala et al. (2020), Ohata et al. (2023), Ono et al. (2023), and Maggi et al. (2024), gathering the largest and more comprehensive collection of laboratory experiments of bedforms by density currents spanning more than 360 data points. They encompass all known bedforms formed under subcritical and supercritical flow regimes, under a diverse array of non-cohesive sediment sizes and densities.

Here we use these data to construct dimensional and dimensionless bedform characteristics and regime diagrams that may be more specifically applicable to the interpretation of turbidite outcrops than ones based purely on fluvial settings. We compare and contrast our results against a compilation of fluvial bedform data from Kennedy (1960), Guy et al. (1966), Brownlie (1981), Gabel (1993), Harbor (1998), Wieprecht (2001), Parsons et al. (2005), Taki and Parker (2005), Frings (2007), Recking et al. (2009), Yokokawa et al. (2011a, 2011b), Núñez-González (2012), Lefebvre et al. (2016), de Almeida et al. (2016), Hernández Moreira (2016), Bradley and Venditti (2017), Lapotre et al. (2017), Hernández-Moreira et al. (2020), Jafarinik (2022), Sanders et al. (2023). All together these correspond to more than 4700 data points, and span laboratory and field scale fluvial bedforms in natural sand and lightweight plastic granular material.

We conclude with a wide-ranging review and analysis of field scale submarine bedforms observed in canyons, levees, slopes, rises, basins, valleys, fans, deltas, and fjords (more than 220 data points). Some of these field bedforms also have associated flow observations which allow

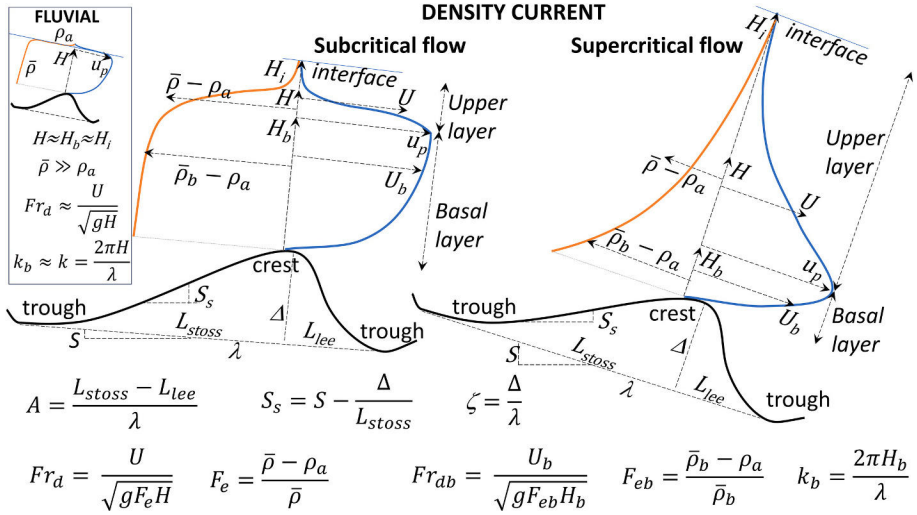

Fig. 1. Sketches of typical sub (left) and supercritical (right) density currents with velocity (blue) and density (brown) profiles, bedform and relevant parameters. Note the different proportions between basal and upper layer in both regimes. Inset: sketch of typical fluvial profiles where the upper layer is assumed to be negligible and due to the large density differences between water and air the Froude number is reduced to a simpler form. Not at scale. (For interpretation of the references to color in this figure legend, the reader is referred to the web version of this article.)

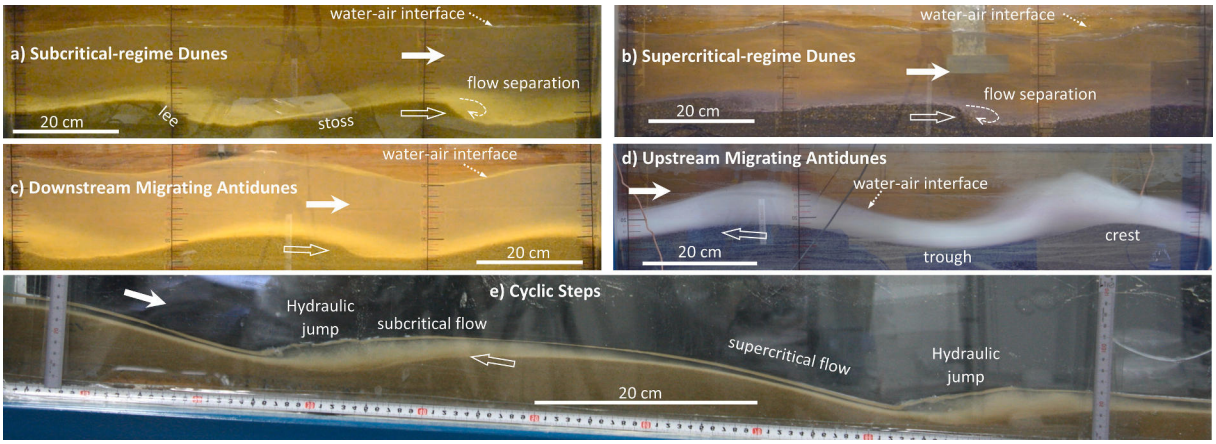

Fig. 2. Side view photos of open-channel flow bedforms over sand. a) Subcritical-regime dunes with S = 0.59 %, d_{50} = 1.11 mm, Fr_d = 0.56; b) supercritical-regime dunes with S = 1.03 %, d_g = 0.95 mm, Fr_d = 1.14; c) downstream-migrating antidunes with S = 1.03 %, d_{50} = 1.11 mm, Fr_d = 0.99; d) upstream-migrating antidunes with S = 1.8 %, d_g = 0.34 mm, Fr_d = 1.24; e) cyclic steps, bonded by hydraulic jumps with average S = 8.7 %, d_{50} = 0.20 mm, Fr_d = 3.51 in the supercritical segments and Fr_d < 1 in the subcritical segments. Note the asymmetry of dunes as opposed to the symmetry and sinusoidal shape of antidunes. Note how the ratio of flow thickness to bedform size (whether λ or Δ) decreases from a) to e). In contrast to the other bedforms, subcritical-regime dunes are unlikely to develop on bed slopes steeper than ~ 1 %. Dunes on both regimes have flow separation on the steep lee side. Only antidunes are in phase with the interface. Upstream-migrating antidunes are the only bedforms where the flow is thicker at the crest and thinner at the trough. Ripples (not shown), resemble dunes in all respects but are smaller, form in finer grain sizes, and do not affect the flow interface. Filled and empty arrows indicate direction of flow and bedform migration respectively. a) to d) adapted from Hernández Moreira (2016), Hernández-Moreira et al., 2020, and Sanders et al. (2023), e) from Yokokawa et al. (2011a).

for a more comprehensive characterization.

The gathering and assessing of datasets developed by different researchers in different laboratories, with different measurements techniques is another differentiating factor of this study with respect to previous efforts, which by limiting themselves to work with datasets of single origin might have been marred by selection, availability, instrumentation, measurement, and confirmation biases that result in high epistemic uncertainty.

1.3. Scope

We aim to identify the formative flows of bedforms; that is, the flow responsible for creating the bedform, rather than other weaker flows that may slightly modify it. We look into the main or defining bedform, not occasional smaller second-order bedforms that might develop superimposed to the main one. In all cases, the flows considered here are turbulent unidirectional flows. Bedforms associated with tidal flows, oscillatory flows, internal waves, and wave-current boundary layers are not included. We consider predominantly down-slope currents, such as turbidity or thermohaline density/bottom currents; but exclude along-slope currents such as contour or geostrophic currents that occur in deep waters, or wind and wave induced alongshore currents that prevail in shallow waters. All bedforms considered are transverse to the flow, not longitudinal such as grooves, ribbons and furrows. We exclude single-row and multiple-row alternate bars, point bars and other bedforms that scale with the dimensions of channel width or larger and have no expression in the absence of systematic transverse variation. This study does not address knickpoints which may control or modulate flows and bedforms; also excluded are phenomena such as slope failures, slumps, creep, compaction, and deformation that may result in features that resemble bedforms but have a different cause.

The bedforms under consideration here are ripples, dunes, upstream-migrating antidunes, downstream-migrating antidunes and cyclic steps. In addition, we consider the plane-bed state corresponding to the absence of bedforms. The bedforms may have a 2D expression, for which their surfaces are defined in terms of bed elevation that varies downstream, or a 3D expression, for which variation in the transverse direction is present as well. They may be depositional (or aggrading), erosional or a hybrid of both.

2. Fluvial bedforms

2.1. Bedform types

The precise definitions of bedforms and bedform states vary from author to author. It is thus useful to provide working definitions here based on the fluvial case. Fluvial flows, whether from the laboratory or the field, are bounded above by a sharp water-air interface (water surface). Subaqueous flows that are the focus of this paper are underflows driven by an excess density caused by dissolved salt or suspended sediment. Dissolved salt serves as an imperfect but useful substitute for fine suspended mud that can drive the flow and does not easily settle out on the bed. We refer to both types of subaqueous bottom flows as density currents. They are bounded above by an interface between saline-turbid water and ambient clear water. The sharpness of this interface depends upon flow conditions, and in particular upon the densimetric Froude number, but it is in general more diffuse than the water-air interface of fluvial flows (Fig. 1). Both the subaqueous and fluvial flows considered here are bounded below by a loose granular bed. We note that the Froude number is a property of the flow; however, for brevity, we often describe bedforms as subcritical or supercritical according to the flow regime under which they form. Furthermore, ripples and dunes indicate by default bedforms formed under subcritical flow regime.

2.2. Bedforms in subcritical regime

Dunes are lower-regime fluvial bedforms associated with an interface that is usually weakly out of phase with the bed (e.g., Kennedy, 1963). The response of the interface may be so weak as to be undetectable to the naked eye (Fig. 2a). Dunes migrate downstream, and most often show asymmetry with a longer gentler stoss face and shorter steeper lee face, though in big rivers their shape can be complex (Cisneros et al., 2020). They are the dominant bedform type in sand-bed rivers under morphologically active flows (e.g., Best, 2005). They are also observed in gravel-bed rivers (Dinehart, 1992; Carling, 1999), although less commonly, largely because the larger grain sizes bias morphologically active flows toward higher values of Froude number, as seen in data from bankfull alluvial rivers by Czapiga et al. (2019).

The literature on lower-regime fluvial bedforms commonly makes a distinction between dunes and ripples (e.g. Engelund and Fredsoe,

1982). These two bedform types have the same asymmetry and the same tendency to migrate downstream. They are both associated with Froude-subcritical flows, but ripples show no interaction with the water surface. Bedforms classified as ripples tend to be smaller than those classified as dunes (e.g., Charru et al., 2013) and a wavelength of ~0.6 m has been suggested as an approximate boundary between them (Simons and Richardson, 1966; Allen, 1982; Ashley, 1990; Lapotre et al., 2017). Vanoni (1975) observed that ripples are rarely formed in sediment coarser than 0.6 mm.

The distinction between ripples and dunes is, however, a matter of debate. One of several characterizations offered by Yalin (1964, 1965) indicates that ripples have wavelengths λ that scale as 1000 d, where d denotes grain size, and dunes have waveheights Δ that scale with flow depth as $H/6$ (García, 2008). As summarized by Raudkivi (1997), as sediment size increases, the wavelength of ripples decreases and the ratio λ/d decreases, ranging from 1000 for a grain size of 0.015 mm, all the way to about 180 for a grain size of 0.83 mm. Based on Babakaiff and Hickin (1996), Best (2005) notes that only when the ratio of waveheight to flow depth Δ/H exceeds ~1/6 is the largest and more chaotic bedform-induced turbulence upwelling observed on the water surface, and furthermore above said threshold the upwelling or "boiling" periodicity becomes persistent, providing support for a reasonable identification of the ripple-dune transition.

Allen (1970) and Bridge (2003) found that dune wavelengths scale with flow depth as $\lambda/H \sim 5$, though the factor can be as large as 10. They also found that, unlike dunes, ripple wavelengths scale with grain size such that the ratio λ/d is in the order of ~1000 (but could well be as high as 2000). We note that for the above-mentioned ripple/dune boundary $\lambda \sim 0.6$ m the 1000 ratio corresponds to a 0.6 mm grain size, coarse sand, which is the ripple threshold pointed out by Vanoni (1975).

The ripple-dune transition is also characterized by an increase in the transport of bed and suspended load related to the increasing importance of the separation zone shear layer and wake region (Schindler and Robert, 2004), and significant changes in the mean and turbulent flow field that causes large changes in the sediment transport over the bedforms (Bennett and Best, 1996; Schindler and Robert, 2004, 2005; Fernandez et al., 2006).

Based on linear stability analysis, Colombini and Stocchino (2011) show that the main mechanism driving instability and formation for both ripples and dunes is the phase lag between bed shear stress and bed elevation. Ripples are shown to be confined to relatively low values of the Shields number and of the particle Reynolds number. For higher values of the Shields number and of the particle Reynolds number ripples are replaced by dunes. At intermediate values of Shields number, they may coexist. Flow depth plays a role in determining bedform wavelength in both cases, but in ripples viscosity is also a controlling factor.

Indeed, other approaches focus on the distinction between ripples and dunes based on the viscous sublayer. Engelund and Hansen (1967) and van den Berg and van Gelder (1993) have associated ripples with the existence of a residual viscous sublayer near the bed, and dunes with the absence of this layer. Thus, ripples will develop for mostly fine-grained sediment in the presence of a viscous sublayer formed along the stoss side, and above which the flow is turbulent (Richards, 1980). If the viscous sublayer is disrupted by coarse sediment particles, then, dunes will be the most common type of bedform. According to this theory the boundary between ripples and dunes is quantified by the ratio between the viscous sublayer thickness (a function of the kinematic viscosity and the shear velocity $\sim 11.6\ \nu/u_*$) and a characteristic bed grain size, typically d_{90}. If the former exceeds the latter ripples will prevail, otherwise dunes will form (García, 2008).

Conversely, Lapotre et al. (2017) and Zanke and Roland (2021) developed further distinctions between ripples and dunes based on the Yalin number $\chi = Re^* \sqrt{\tau^*}$ —involving the shear Reynolds number and the Shields parameter— and a dimensionless bedform wavelength. The Yalin number can be interpreted as a metric for the susceptibility of a grain on the bed to be entrained by fluid flow, which not only depends on flow strength relative to the particle weight, but also on the degree to which the particle is immersed within the viscous sublayer. Lapotre et al. (2017) proposed that ripples develop when $\chi < 4$, dunes are formed when $\chi > 9$, and transitional bedforms fall in between. This resembles Vanoni (1975) criterion dividing ripples from dunes with a line given by $\tau^* = 317 Re^{*-2.8}$, which supports the idea that the presence of a viscous sublayer enhances the development of ripples.

Finally, Jerolmack and Mohrig (2005), Bartholdy et al. (2015) and Flemming (2022) have questioned the basis for any distinction between ripples and dunes, pointing to the existence of a continuum of scales of all wavelengths below the largest dunes.

A pragmatic definition for the distinction between ripples and dunes is introduced in section 4.1, but the above ambiguities must be borne in mind for the resulting interpretation. This is all the more so because the above criteria are not necessarily consistent with each other.

2.3. Bedforms in supercritical regime

The characteristic fluvial bedform of upper regime, i.e. the antidune, is defined in terms of an interface with undulations that are in phase with bed undulations (e.g., Kennedy, 1963). This phasing is typically easy to recognize in the laboratory. The most commonly observed type of antidune migrates upstream (Fig. 2d), showing a relatively symmetrical and sinusoidal shape. Trains of these antidunes can migrate upstream in echelon, but more commonly they are subject to cyclic collapse and reformation (e.g., Kubo and Yokokawa, 2001; Izumi and Parker, 2009). Downstream-migrating antidunes have also been observed (e.g., Carling and Shvidchenko, 2002; Núñez-González and Martín-Vide, 2011) and tend to be rather symmetrical as well (Fig. 2c). Supercritical dunes have been only recently investigated (e.g., Hernández-Moreira et al., 2020; Sanders et al., 2023) and sometimes classified as downstream-migrating antidunes (Fig. 2b).

Cyclic steps are upstream-migrating transcritical bedforms (Fig. 2e). They occur in trains, such that each bedform is bounded by hydraulic jumps upstream and downstream, with the flow being Froude-subcritical mostly on the stoss side and Froude-supercritical on the lee side, hence transcritical (e.g., Taki and Parker, 2005; Yokokawa et al., 2009; Kostic et al., 2010). Cyclic steps require supercritical flow conditions to trigger their formation. In other words, corresponding uniform flows that would develop over a fixed sloping bed averaged over the extent of the bedforms would be supercritical. The flow averaged over cyclic steps once they have formed, however, may be modestly super- or subcritical depending on the relative lengths of the stoss and lee sides (Spinewine et al., 2009). Once formed, cyclic steps typically have significantly smaller wavenumbers (i.e. longer wavelengths) than antidunes but are more stable and migrate upstream at a slower pace than antidunes.

Chutes-and-pools are trains of upstream-migrating antidunes that break and form transient hydraulic jumps. They are hybrid bedforms that occur in upper-flow-regime conditions, populating the field between antidunes and cyclic steps (Cartigny et al., 2014; Slootman et al., 2021). Sometimes they are just classified as cyclic steps.

2.4. Lower and upper plane bed regimes

Under some conditions, a mobile bed of sediment can remain plane. Two plane-bed regimes are commonly recognized for fluvial flows: lower and upper plane bed regime.

Lower regime plane bed (LPB) is an indication of minimal bedload transport rates, usually observed when the bed shear stress induced by the flow is just above the threshold for motion. For sand dunes LPB is a necessary first step before they begin to form; while with fine sediment, ripples may form directly with no observable LPB in between (Southard

Table 1
Summary of sediment types and sources of experimental density current data.

Name	Type	Density [kg/m3]	d_{16} [μm]	d_{50} [μm]	d_{84} [μm]	d_{90} [μm]	σ_g [−]	Reference
P1	plastic	1530	52	68	85	95	1.28	
S1	sand	2650	192	246	339	365	1.33	
P2	plastic	1530	185	206	241	248	1.14	Sequeiros et al. (2010a, 2010b)
P3	plastic	1530	1153	1447	1781	1875	1.24	
P4	plastic	1530	967	1623	2606	2870	1.64	
M1*	plastic	1530	230	1499	2811	3102	4.20	Spinewine et al. (2010)
P5	plastic	1530	182	210	237	248	1.15	Spinewine et al. (2009)
C1	coal	1350	59	101	150	165	1.56	García and Parker (1993)
C2	coal	1350	108	184	250	270	1.51	
P6	plastic	1530	42	57	77	90	1.37	Sequeiros et al. (2018)
P7	plastic	1500	182	245	360	410	1.41	
P8	plastic	1500	210	310	440	487	1.45	
S2	sand	2600	150	206	290	324	1.39	
S3	sand	2600	270	480	715	790	1.63	Koller et al. (2017, 2019)
G1	glass	2544	78	111	153	157	1.39	Koller et al. (2022)
G2	glass	2544	39	68	99	109	1.60	
P9	plastic	1500	310	427	590	649	1.38	de Cala et al. (2020)
P10	plastic	1500	85	120	155	–	1.35	
P11	plastic	1500	163	230	297	–	1.35	
P12	plastic	1500	213	300	387	–	1.35	
P13	plastic	1500	325	458	592	–	1.35	Fedele et al. (2016)
P14	plastic	1500	130	184	238	–	1.35	Fedele (unpub.)
S4	sand	2650	223	300	377	–	1.30	
S5	sand	2650	260	350	440	–	1.30	
S6	sand	2650	372	500	628	–	1.30	
P15	plastic	1040	230	300	375	380	1.28	Maggi et al. (2024)
C3	coal	1400	–	79	–	–	–	Manica (unpub.)
S7	sand	2650	–	~100	–	–	–	
P16	Plastic	1500	125	177	233	241	1.37	Ono et al. (2023)
P17	Plastic	1500	184	254	348	382	1.37	Ohata et al. (2023)
P18	Plastic	1500	308	428	590	358	1.38	

and Boguchwal, 1990; van den Berg and van Gelder, 1993).

Upper regime plane bed (UPB) is associated with high sediment transport rates. Sometimes it is also characterized by a large amount of bedload that moves in the form of sheets with no or negligible bed deformation. However, it has also been reported in the literature, rather ambiguously, that UPB is a transitional state observed when either ripples, dunes or antidunes are washed away by the strengthening of the flow. Part of the confusion resides in the fact that the transition between regimes depends also on the grain size of the bed material. In fluvial flows UPB are reported when either ripples or dunes are washed out. For fine sediments the transition between ripples and UPB may occur without the development of dunes, as most of the sediment is entrained into suspension. In both cases this precedes the formation of antidunes (Zanke, 1976; Guy et al., 1966; Engelund, 1970; Bridge and Best, 1988; Southard and Boguchwal, 1990; van den Berg and van Gelder, 1993).

Ohata et al. (2022) suggested regions for the formation of both regimes unrelated to the threshold condition of sediment motion, a unique value of particle diameter, or a Froude number of unity. LPB seem to be defined by bedload-only flows, and UPB are associated with suspension dominated flows.

Hernández-Moreira et al. (2020) proposed that two different types of UPB can be defined, one associated with standard bedload transport at the dune–antidune transition, and the other associated with bedload transport in sheet flow mode at the transition between upstream and downstream migrating antidunes.

Transition is a category for flows that mold bedforms ranging from those typical of the lower flow regime to those typical of the upper flow regime. Standing waves are virtually stationary waves associated with supercritical flow, i.e., antidunes (Guy et al., 1966; Sanders et al., 2023).

2.5. Bedform regime diagrams

A variety of phase diagrams for bedform regime have been proposed; these are summarized in García (2008). Simons and Richardson (1966) used grain size and stream power to define a 2D phase diagram with regimes for no movement, ripples, dunes, antidunes and plane bed. Southard and Boguchwal (1990) and Ashley (1990) used flow velocity and grain size to define a 2D diagram with regimes for no movement, lower-regime plane bed, upper-regime plane bed, ripples, dunes and antidunes.

The above two-phase diagrams involve the use of dimensional parameters. A more formal approach involves dimensionless parameters (Parker and Anderson, 1977). For example, the 2D diagram of van den Berg and van Gelder (1993) discriminates bedforms according to a bed mobility parameter (similar to the Shields number) and a dimensionless grain size d^*. The 3D diagram of Vanoni (1974) discriminates according to the Froude number and the ratio H/d_{50} of flow depth H to median sediment grain size d_{50}. Some of such diagrams have a specialized purpose. For example, Carling and Shvidchenko (2002) present a 2D diagram using Froude number and the ratio of flow velocity to critical shear velocity to (among other things) discriminate between regimes for upstream-migrating and downstream-migrating antidunes. Yokokawa et al. (2011a) present 2D dimensionless phase diagrams designed to quantify formation regimes of three supercritical-flow bedforms: upstream-migrating antidunes, downstream-migrating antidunes, and cyclic steps. Ohata et al. (2017) expanded the analysis to 3D diagrams based on Froude number, Shields number and dimensionless grain size, or dimensionless flow velocity, height and grain size.

In this study we report on density current analogs to all these bedform types/states. We go on to develop phase diagrams for density currents that are a) directly comparable to the fluvial case, but b) are more likely to be applicable to the case of turbidity currents at field scale than those obtained from experiments designed to model river flows.

3. Data compendium

We observed a wide range of bedform types in all compiled experiments (sources in Table 1). Although in some cases their classification

may be subject to interpretation, we have sought to rely as much as possible on unambiguously identifiable features for their characterization. Here we list the relevant parameters that we used to characterize and classify bedforms and describe how they were estimated from experimental observations. Additional parameters will be introduced later. The definitions of all parameters are found in the Notation section.

3.1. Froude and wavenumber

We introduce several parameters to establish working definitions for the flows and bedforms in question. Here H = layer-averaged flow thickness, U = layer-averaged flow velocity, g = gravitational acceleration, Δ = bedform waveheight, λ = bedform wavelength, $\overline{\rho}$=layer-averaged density of the underflow and ρ_a = density of the ambient fluid above the interface (i.e. above H_i). The average fractional excess density F_e of the flowing fluid relative to that of the ambient fluid is defined as

$$F_e = \frac{\overline{\rho} - \rho_a}{\overline{\rho}} \tag{1}$$

The densimetric Froude number Fr_d is defined as

$$Fr_d = \frac{U}{\sqrt{gF_eH}} \tag{2}$$

Water, whether clear or laden with suspended sediment or dissolved salt, is three orders of magnitude heavier than air. In the fluvial case, then, F_e can be well approximated by unity, and Eq. (2) devolves into a simpler form (see Fig. 1). The density currents considered here are dilute in terms of both dissolved salt and suspended sediment, so that $F_e << 1$. With this in mind, we use the notation Fr_d for both fluvial and subaqueous flows.

Fluvial flows with $Fr_d > 1$ are termed supercritical, and those with $Fr_d < 1$ are termed subcritical. This definition, however, could be somewhat misleading because it has been argued that the critical Froude number of a turbidity current can be non-unity depending on the degree of entrainment of ambient fluid and the density variation in the current (Huang et al., 2009). A more general definition associates subcritical flow with a state under which the streamwise variation of interface elevation is out of phase with the bed, and supercritical flow with a state under which the reverse phasing occurs. Anderson (1953) and Kennedy (1963) have shown in the case of fluvial potential flows, and Engelund and Fredsoe (1982) in case of fluvial shear flows, that the effective dividing line between subcritical and supercritical flows is a function of the dimensionless bedform wavenumber k:

$$k = \frac{2\pi H}{\lambda} \tag{3}$$

More specifically, in the long-wave limit $k \to 0$, the Froude number bounding subcritical and supercritical response becomes equal to unity, but as k increases toward the range of the bedforms studied here, it drops below unity. The result is that even fluvial flows with values of Fr_d that are somewhat below unity can show supercritical response over undulating beds. This has been informally absorbed into the research community in terms of the classifications of upper-regime and lower-regime as shorthand for supercritical-response and subcritical-response regimes. Thus, lower and upper Froude number regimes do not exactly align with lower and upper plane bed regimes.

In addition, we define the basal densimetric Froude number Fr_{db} as:

$$Fr_{db} = \frac{U_b}{\sqrt{gH_bF_{eb}}} \tag{4}$$

where H_b is the density current thickness of the basal (or lower) layer measured from the bed to the height of peak velocity u_p, as sketched in Fig. 1, U_b is the average velocity of the basal layer, and F_{eb} is the basal fractional excess density estimated with the layer-averaged density of the basal layer $\overline{\rho_b}$ as:

$$F_{eb} = \frac{\overline{\rho_b} - \rho_a}{\overline{\rho_b}} \tag{5}$$

The grounds for this are discussed below, but it derives from the fact that as opposed to fluvial flows, even current thickness is an ambiguous parameter in the case of density currents. The current often has a diffuse interface with the ambient fluid, where velocity and excess density only gradually vanish in the upward direction. Indeed, vertical velocity profiles of density currents substantially differ from their fluvial counterparts, or rather the resemblance extends only up to H_b. This motivates the assessment of a dimensionless basal bedform wavenumber k_b as:

$$k_b = \frac{2\pi H_b}{\lambda} \tag{6}$$

We note that for fluvial flows, the flow height is effectively the basal flow height, hence $H \approx H_b$. (Fig. 1).

3.2. Dimensionless grain size

The grain size distribution of the bed sediment is represented by a median grain size, d_{50}, and a standard deviation σ_g expressing a uniformity index, as summarized in Table 1. It is nondimensionalized in the form originally introduced by Bonnefille (1963) and used by Chaubert and Chauvin (1963) in their bedform classification diagram (García, 2008). The Valenbois-Bonnefille dimensionless particle diameter, is defined as

$$d^* = d_{50}\left(\frac{gR_b}{\nu^2}\right)^{1/3} \tag{7}$$

where $R_b = (\rho_s - \rho_b)/\rho_b$ is the near-bed submerged specific density of sediment, ρ_s is sediment density, and ρ_b is the near-bed density of the flow.

The particle Reynolds number is another similar parameter used to characterize different stages of particle movement in tandem with the Shields number.

$$Re_p = \sqrt{gR_bd_{50}}d_{50}\Big/\nu \tag{8}$$

This parameter is equal to $(d^*)^{3/2}$ and is normally used to estimate the dimensionless Shields number for initiation of motion (e.g., Brownlie, 1981).

3.3. Bed shear stress and Shields number

If for uniform fluvial flows the bed shear stress can be estimated at a reach scale from the relation $\tau = \rho gHS$, the same does not hold for a density underflow due to entrainment of ambient water across the top interface of the current. Because of interface mixing, in density currents a logarithmic profile controlled by bed friction is expected to hold only in a near-bed region below the level of peak streamwise velocity. The shear velocity u_* and the bed shear stress τ_b can be determined from the fitting of a logarithmic law of the wall to the vertical profiles of streamwise velocity as described in the Supplementary Material. The bed shear stress is then obtained as:

$$\tau_b = \rho_b u_*^2 \tag{9}$$

where ρ_b is the near-bed flow density. Bed shear stress is further nondimensionalized to get the corresponding Shields number τ^*:

$$\tau^* = \frac{\tau_b}{\rho_b R_b g d_{50}} \tag{10}$$

In cases where bedforms of significant height and asymmetry display flow separation, the bed shear stress and Shields number are further divided into a skin friction component and a form drag following, for example, Nelson and Smith (1989).

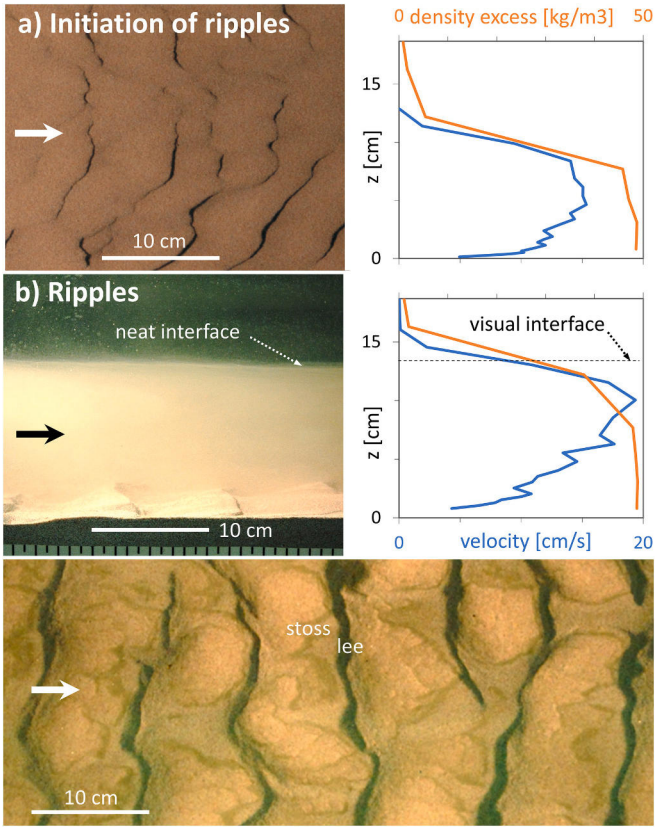

Fig. 3. a) Initiation of ripples. Plan view photo of small ripples, just over the initiation of sediment motion (left). Velocity and density profiles of the associated saline current (right). From experiment SUB11b (Sequeiros et al., 2010a) for which bed sediment was P2, bed slope was S = 0.19 %, total and basal Froude numbers Fr_d = 0.54, Fr_{db} = 0.75. b) Ripples: side view photo during experiment (top left), note the neat interface between saline current and ambient fluid, typical of subcritical regime. The interface seems mostly unaffected by the ripples. Measured velocity and density profiles (top right). Plan view photo after flume dewatering (bottom). From experiment SUB10b (Sequeiros et al., 2010a) with bed sediment P2, bed slope S = 0.49 %, total and basal Froude numbers Fr_d = 0.57, Fr_{db} = 0.56. Arrows indicate direction of flow and bedform migration.

The Mobility parameter of the basal flow is defined after van den Berg and van Gelder (1993) as:

$$\theta_b' = \frac{{U_b}^2}{R_b d_{50}(18\log(4H_b/d_{90}))^2} \tag{11}$$

Following Bonnefille (1963), basal flow thickness and depth-averaged velocity are nondimensionalized after Ohata et al. (2017) as:

$$H_b^{*B} = H_b\left(R_b g/\nu^2\right)^{1/3} \tag{12}$$

$$U_b^{*B} = U_b(R_b g\nu)^{-1/3} \tag{13}$$

Alternatively, length parameters can be nondimensionalized relative to d_{50} (Allen, 1970) or with u_*/ν (Lapotre et al., 2017).

3.4. Bedform characteristics

In addition to the bedform waveheight Δ, wavelength λ, steepness $\zeta = \Delta/\lambda$, direction and rate of migration, 2D or 3D planform arrangement, and the degree of asymmetry based on stoss and lee sides are included in the database when available. The asymmetry parameter A is defined after van Landeghem et al. (2012) as:

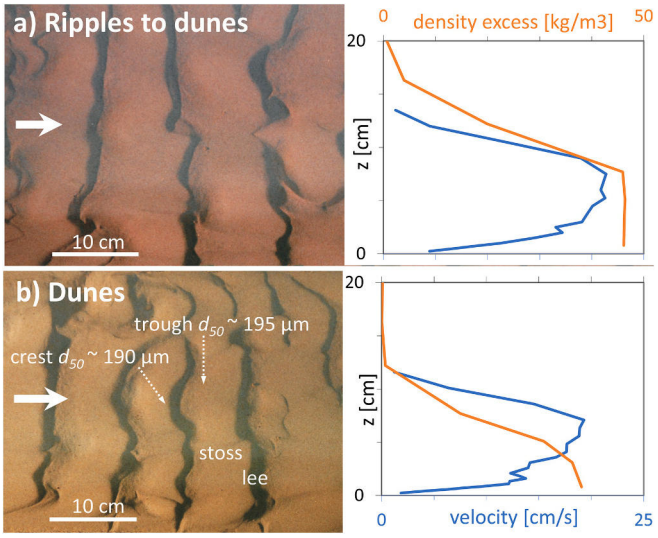

Fig. 4. a) Ripples transitional to dunes: plan view photo (left) and velocity and density profiles of the associated saline current (right). From experiment SUB09 (Sequeiros et al., 2010a), with bed sediment P2, bed slope S = 0.49 % and Froude number Fr_d = 0.79 (Fr_{db} = 0.93). b) Dunes: plan view photo (left) and velocity and density profiles of the associated saline current (right). From experiment SUB06b (Sequeiros et al., 2010a), with bed material P2, bed slope S = 0.85 % and Froude number Fr_d = 0.82 (Fr_{db} = 0.85). Crests have finer sediment than troughs. Arrows indicate direction of flow and bedform migration.

$$A = \frac{L_{stoss} - L_{lee}}{\lambda} \tag{14}$$

where L_{stoss} and L_{lee} are lengths of the stoss and lee side of the bedform respectively (Fig. 1). The average slope of the bedform stoss side S_s, a parameter useful to tell apart cyclic steps from upstream migrating antidunes, is estimated with the following equation:

$$S_s = S - \frac{\Delta}{L_{stoss}} \tag{15}$$

The convention for positive slope is clockwise from horizonal, hence a typical average (or regional) bed slope S is positive, while S_s can be negative.

3.5. Uncertainty assessment

For those experiments where several velocity and/or concentration profiles were obtained at the same location, calculated flow parameters were averaged to preserve only one single datapoint. Likewise, measurements of trains of bedforms associated with a certain flow condition and location were averaged. This reduces the number of datapoints but provides for more robust statistics, as well as a metric for quantifying epistemic and aleatory uncertainty by including minima and maxima.

Spatial flow variation along individual bedforms is another sort of uncertainty, even on bedforms without flow separation (Fedele et al., 2016). For example, we estimate fluctuations in Froude number within a bedform length of ~13 %.

Pertaining to field observations (section 6), there can be a mismatch between observed flow and observed bedforms. While both may be reasonably measured, it is not a given that the reported flow created the reported bedform. In additon, given the more transient and sporadic nature of field turbidity currents relative to rivers, we do not know whether we are observing fully developed bedforms.

4. Experimental density current bedforms

4.1. Ripples

As in fluvial flows, distinguishing ripples from dunes in density currents is often subject to interpretation. Ripples are of smaller amplitude than dunes and are known to scale better with grain size than with flow depth. They do not seem to induce perturbations of the current interface. On the other hand, fluvial dunes tend to scale approximately as 1/6 of the flow depth and induce small, but noticeable perturbations at the interface. In the present analysis of subaqueous bedforms, the classification of ripples versus dunes is subject to a larger degree of interpretation than for their fluvial counterparts, as the possible perturbations of the current interface were less evidently measurable. To mitigate this challenge, we chose a hybrid classification first relying on the ratio of waveheight to current thickness and on the ratio of bedform wavelength to mean grain size, which are easily measured parameters: bedforms formed under subcritical flow with Δ/H_b lower than 1/6, and λ/d_{50} lower than 2000 were classified as ripples, otherwise as dunes. If some parameters were lacking for this assessment, then bedforms with Yalin number χ lower than 4 were classified as ripples, and those above that threshold as dunes.

Given the above criteria, ripples were observed for moderate subcritical flows over fine/light sediment beds (e.g., P2, P7, P18 in Table 1). Bed slopes ranged from 0.19 % to 1.50 %, basal densimetric Froude numbers range was 0.55–0.98.

In Sequeiros et al. (2010a), starting from flat beds, ripples formed very quickly after starting the flow. They adjusted themselves into periodic patterns with stable wavelength in the order of a minute, and subsequently started to migrate downstream at a constant speed. The ripples started to appear immediately after initiation of motion of bed sediment, at very small transport rates. Sediment transport itself appeared to be controlled by ripple migration, with all visible transport on the gentle stoss side depositing over the short lee face after the ripple crest.

Sample photographs of ripple structure are given in Fig. 3 and Fig. 4a for the same plastic bed material (P2) but distinct stages of maturation. Ripples in Fig. 3a developed over a gentle bed slope $S = 0.19$ %, under subcritical regime ($Fr_d = 0.54$ and $Fr_{db} = 0.75$). The bed shear stress was just above initiation of sediment motion, and the ripples had very small waveheights ($\Delta \sim 0.2$ cm). They have elongated crests but are not very well aligned across the channel width, instead showing a 3D planform.

Ripples in Fig. 3b are more developed and created by a density current on a slightly steeper, yet still gentle slope ($S = 0.49$ %, $Fr_d = 0.57$, $Fr_{db} = 0.56$). Based on visual observations, the basal layer upper surface and the density current interface are hardly affected by the bedforms, whose waveheight to current thickness ratio Δ/H_b is still just below 1/6. The velocity and density profiles show the typical characteristics of subcritical density currents, with a peak velocity u_p closer to the sharp interface than to the bed, a thin upper layer, and a well-mixed, rather uniform density in the basal layer (Fig. 1).

Bedforms in Fig. 4a have bed slope S = 0.49 % and a higher Froude number $Fr_d = 0.79$ ($Fr_{db} = 0.93$). These bedforms may be called ripples transitional to dunes, with a ratio $\Delta/H_b = 0.19$, just above threshold 1/6. They are organized into a clearer 2D pattern than those of Fig. 3a, with crestlines well aligned and trackable across the whole channel width.

Ripples are commonly downslope-asymmetrical, with stoss sides longer than lee sides ($0.36 < A < 0.85$), and some flow separation observed on the lee side. Ripples may develop an armored layer of coarse material in their troughs as a result of downward coarsening (Guy et al., 1966; Blom et al., 2003).

4.2. Dunes

Bedforms formed under subcritical flow regime with waveheight to current thickness ratio Δ/H_b higher than 1/6 or wavelength to median grain size ratio λ/d_{50} higher than 2000 were classified as dunes. If some parameters were lacking for this assessment, then bedforms with Yalin number χ higher than 4 were classified as dunes. Dunes were observed for experiments where bed sediment was fine or low density (P2, P9, P18), an example of dunes is shown in Fig. 4b with S = 0.85 % under subcritical regime ($Fr_d = 0.82$, $Fr_{db} = 0.85$).

Dunes developed by density current occurred on bed slopes from 0.49 % to 1.22 %, with a basal Froude number range of $Fr_{db} = 0.70$–0.93, The dunes looked very similar to the transitional bedforms depicted in Fig. 4a, except that the waveheight was larger when compared to current thickness. Flow observations supported by video recordings point to marked turbulent flow in the near bed region, more flow detachment downstream of the lee side than in the case of ripples, and bursts of suspended sediment. These constitute additional reasons to classify these bedforms as dunes (Bennett and Best, 1996; Schindler and Robert, 2004, 2005; Best, 2005; Fernandez et al., 2006).

Dunes, like ripples, tend to be downslope asymmetrical ($0.28 < A < 0.73$) with downward coarsening (Guy et al., 1966; Blom et al., 2003). Density current dunes are out of phase with the basal layer upper surface and the interface (Sequeiros et al., 2010a; de Cala et al., 2020), a behavior also observed in fluvial flows.

Dunes have vertical sorting corresponding to upward fining as reported by Blom et al. (2003). Even for well-sorted experiments with sediment P2, typical d_{50} on the dune's crests were ~ 3 % finer than on the troughs (190 μm vs 195 μm, Fig. 4b).

4.3. Supercritical-regime ripples and dunes, downstream-migrating antidunes

Within our database downstream-migrating bedforms were the most common type observed under supercritical regime. We distinguish them in three main categories: supercritical ripples (SR), supercritical dunes (SD) and downstream-migrating antidunes (DMA).

Fedele et al. (2016) classified Froude-supercritical downslope-asymmetric downstream-migrating bedforms as "supercritical dunes" as opposed to symmetric and sinusoidal DMA. Flow separation is the key feature to set SD apart from DMA. Supercritical dunes have more rounded crests than dunes, but they are downslope asymmetric and have a clear separation zone on the lee side. On the contrary, DMA are symmetrical with sinusoidal shape and no flow separation.

Supercritical dunes are unlikely to be in phase with the density current interface or the basal layer upper surface; whereas DMA are observed to be in phase with both (Fedele et al., 2016). Both SD and DMA, however, have in common that the flow thickness (both H_i and H_b) is thinner at the crest than at the trough and hence there is an expansion of the flow from crest to trough that favors separation, as reported for fluvial DMA by Núñez-González and Martín-Vide (2011). This crest/trough difference in H_b is small and difficult to gauge, especially in DMA.

The more symmetric and sinusoidal in shape the bedforms are, the more likely they will be in phase with the flow and less likely flow separation will occur (Fedele et al., 2016; de Cala et al., 2020). See section 7.8 for further discussion on this issue.

For near-critical or supercritical flow, the effect of viscosity becomes less relevant. This is certainly the case in sinusoidal-shaped upstream- and downstream-migrating antidunes associated with rapid flow conditions and profuse bedload transport. However, some supercritical density currents develop rather small bedforms that can be best described as "supercritical ripples" (SR) in view of their size and asymmetry as well as the ratio between the viscous sublayer thickness and the skin roughness.

To distinguish SR from SD we have used the same criteria to separate ripples from dunes in the subcritical regime ($\Delta/H_b > 1/6$ *or* $\lambda/d_{50} > 2000$, $\chi > 4$ for dunes). In addition, and regardless of the Froude number regime, wavenumber is another valuable parameter to distinguish them, with ripples having larger wavenumbers k_b than dunes, and rarely below ~3.

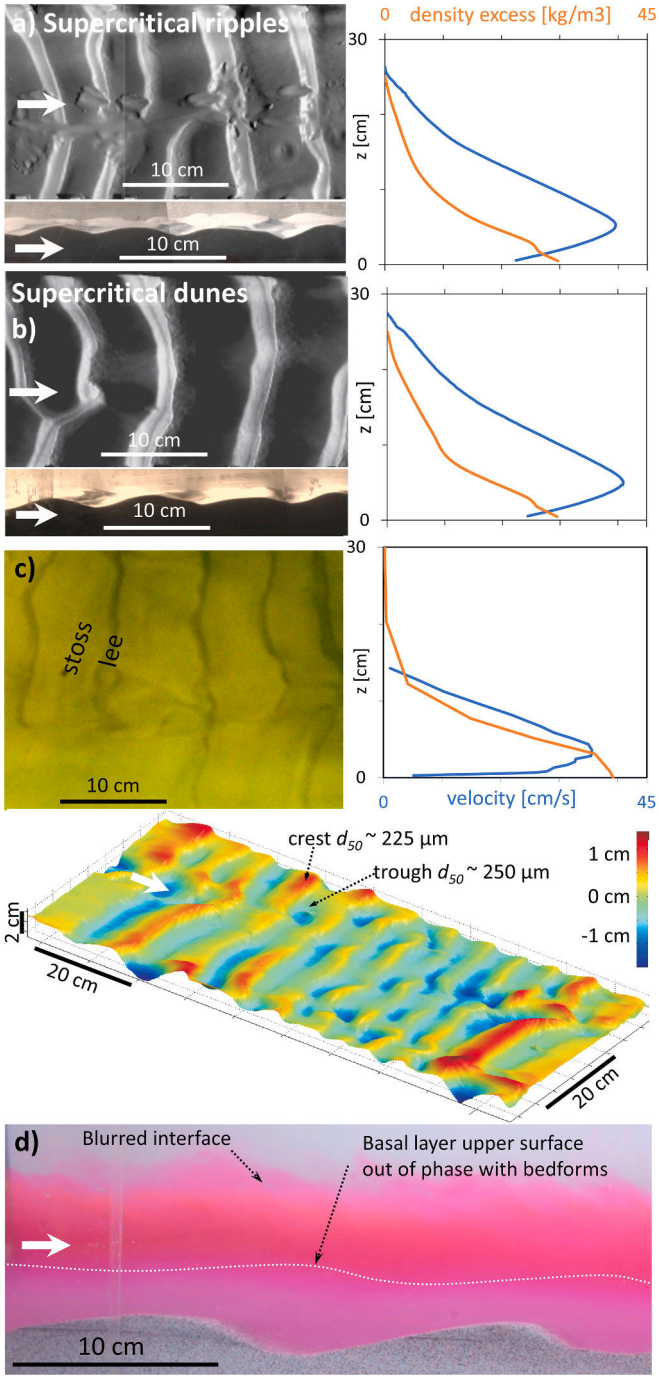

Fig. 5. a) Supercritical-regime ripples formed by turbidity current, plan and side view photos (left), and velocity and density profiles of the associated current (right). From experiment TC2 by Koller et al. (2022), with bed material G2, bed slope S = 5.6 % and Froude number $Fr_d = 1.89$ ($Fr_{db} = 2.95$). b) Supercritical-regime dunes formed by turbidity current, plan and side view photos (left), and velocity and density profiles of the associated current (right). From experiment TC3 by Koller et al. (2022), with bed material G2, slope S = 5.5 % and Froude number $Fr_d = 1.95$ ($Fr_{db} = 2.95$). Bedforms are mildly downslope asymmetrical. Pictures were taken after slowly draining the flume, which may have distorted to some extent the bedform shapes. c) Supercritical-regime dunes formed by saline current: plan view photo (top left), velocity and density profiles of the associated current (top right), and reconstructed laserscan bathymetry (bottom). From experiment SUP49 by Sequeiros et al. (2010a), with bed material S1, slope S = 5 % and Froude number $Fr_d = 1.55$ ($Fr_{db} = 2.35$). Crests have finer sediment than troughs. Bedforms are distinctly downslope asymmetrical. The variation in shading documents elevation deviation from the mean bed profile averaged over the steps. d) Supercritical-regime dunes formed by saline current. Bedforms are out of phase with interface and basal layer upper surface. From Fedele et al. (2016) with bed material P12, bed slope S = 17.6 % and Froude number $Fr_d = 1.65$. Arrows indicate direction of flow and bedform migration.

Supercritical ripples were observed for experiments where bed sediment was P2, P6, P7, P8, P18, S2, S3, G1 and G2, that is fine/medium plastic, fine glass and medium sand material; under a wide range of Fr_{db} (1.00–3.45), bed slopes (0.49 %–7.34 %). They are downslope asymmetrical but less so than subcritical ripples ($0.11 < A < 0.72$). Supercritical ripples are very short bedforms, with k_b larger than 10, and have intermediate steepness ($0.05 < \zeta < 0.13$). An example of SR close to the boundary with SD is seen in Fig. 5a, formed by a turbidity current moving over a bed composed of glass beads (G2), slope $S = 5.6$ % and $Fr_d = 1.89$ ($Fr_{db} \sim 2.95$). These SR are well developed and have a very

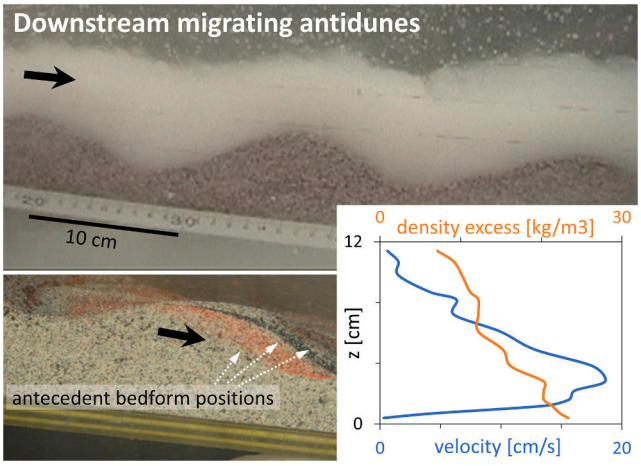

Fig. 6. Downstream migrating antidunes: side view photo shows the sinusoidal and symmetrical bedforms in phase with the current interface (top), characteristic bedding indicating downstream migration pattern (bottom left), spatially averaged velocity and density profiles of the associated density current (bottom right). From Fedele et al. (2016), with bed material P11, bed slope S = 7.7 % and Froude number $Fr_d = 1.39$ ($Fr_{db} \sim 1.67$). Arrows indicate direction of flow and bedform migration.

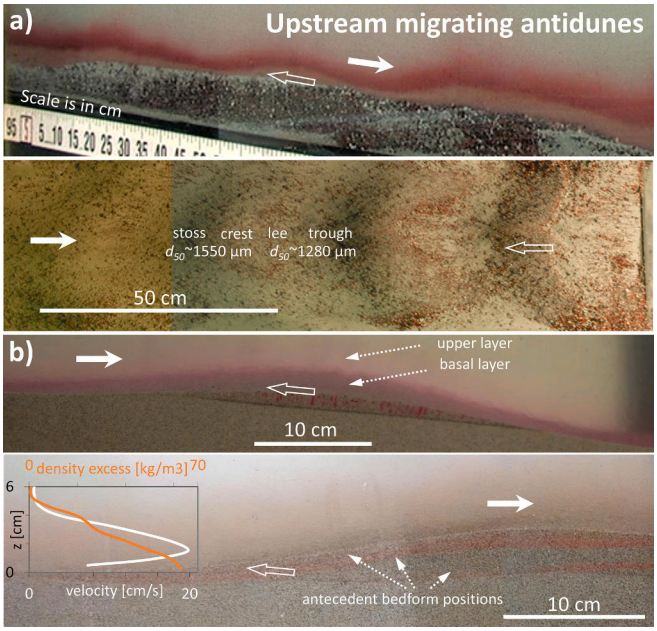

Fig. 7. a) Upstream migrating antidunes formed by hybrid saline-turbidity current: side view photo shows turbidity current in phase with bedforms (top), plan view photo mosaic after flume was dewatered (bottom). These UMA have coarser material deposited on the stoss and crest segments than on lee and trough segments. From experiment SUP56 (Sequeiros et al., 2010a), with bed material P4, bed slope S = 5 % and Froude number $Fr_d = 1.91$ ($Fr_{db} \sim 2.98$). b) Upstream migrating antidunes formed by saline current: side view shows density current in phase with bedform (top). The intense near-bed coloring by a higher concentration of suspended sediment is an indication of the spatial variation of the basal layer, which seems thicker above the crest. Side view of bedform stoss, where antecedent bed configurations show the upstream migrating nature of the bedform (bottom). Spatially averaged velocity and density profiles of the associated density current (inset bottom left). From unpublished experiments by J.J. Fedele, with bed material P10, bed slope S = 6.1 %, $Fr_d = 1.25$ ($Fr_{db} \sim 1.50$). Filled and empty arrows indicate direction of flow and bedform migration respectively.

mild asymmetry.

Supercritical dunes developed with bed sediment P2, P7, S1, G1, G2, C1, C2; fine/medium plastic, fine glass, fine coal and medium sand material; Froude numbers $Fr_{db} = 1.14–3.34$, and bed slopes from 0.85 % to 12.3 %. Like dunes, they are downslope asymmetric, with a wider range of asymmetry, from mildly to very downslope asymmetric ($0.10 < A < 0.75$). Supercritical dunes are short ($0.76 < k_b < 4.75$), and steep ($0.07 < \zeta < 0.21$) bedforms. In Fig. 5b-c two examples of mildly and markedly asymmetrical SD respectively are shown. The former, created by a larger turbidity current than that responsible for the SR in Fig. 5a, have glass beads (G2) as bed material; $S = 5.5$ %, $Fr_d = 1.95$ ($Fr_{db} \sim 2.95$), and $A = 0.30$. The latter were developed over sand (S1) with a similar slope S = 5.0 %, but lower specific discharge, with $Fr_d = 1.55$ ($Fr_{db} = 2.35$) and $A = 0.75$. Both have a mostly 2D planform. The velocity and density profiles show the typical characteristics of supercritical density currents, with a peak velocity u_p closer to the bed than to the interface and a thick upper layer, in contrast to those of subcritical density currents (e.g. Fig. 1, Fig. 3). Supercritical dunes are not in phase with the flow (Fig. 5d).

Downstream-migrating antidunes developed with bed sediment P3, P9, P11, P12 and P18, composed of medium to coarse plastic beads. The Froude number range was $Fr_{db} = 1.48–3.58$, and bed slopes ranged from 5.0 % to 17.6 %. They are mostly symmetrical but slightly skewed to the downslope side ($-0.13 < A < 0.20$). DMA are longer than SD ($0.31 < k_b < 0.96$), and steep ($0.03 < \zeta < 0.34$) bedforms. Fig. 6 is an example of a DMA formed by a density current moving over a bed composed of fine/medium plastic sediment (P11), slope $S = 7.7$ % and $Fr_d = 1.39$ ($Fr_{db} \sim 1.67$). These DMA are quite symmetrical ($A \sim 0.12$) and in phase with the flow interface.

All these supercritical downstream-migrating bedforms, like dunes, usually show vertical sorting corresponding to upward fining. For experiments with sediment S1, typical d_{50} on the SD crests were 10 % finer than on the troughs (225 µm vs 250 µm). This has also been observed in fluvial DMA (e.g., McBride et al., 1975; Núñez-González, 2012). The process of upward fining in DMA may differ from that of SD/dunes though, considering that avalanche faces on the lee side may not develop in the former case, and may be influenced by the symmetry of the bedform and absence of flow separation on the lee side. In any case, however, the result is segregation of coarser grains on the trough (and lee) and of finer grains on the crest (and stoss). This downward coarsening may or may not be preserved in the stratigraphic record, depending on the presence or absence of aggradation. Its expression is also influenced by the degree of grain size sorting (Núñez-González, 2012).

4.4. *Upstream-migrating antidunes*

Upstream-migrating antidunes (UMA) formed with bed sediment P3, P4, M1, P9, P10, P11, P14 and P17, a wide range of plastic from middle to coarser sizes. The Froude number range was $Fr_{db} = 1.50–3.49$, and bed slopes varied from 5.0 % to 17.6 %. UMA are in phase with the basal flow and interface of the density current, and have longer wavelengths relative to flow depth ($k_b = 0.11–0.31$) than DMA. They are also less steep than DMA ($0.03 < \zeta < 0.10$). UMA are mostly symmetrical ($|A| < 0.1$), have usually a sinusoidal shape and no flow separation.

The bedforms in Fig. 7a were developed for $S = 5.0$ %, $Fr_d = 1.91$ ($Fr_{db} \approx 2.98$), and $A = -0.02$. The upstream migration is a byproduct of differential sediment transport and deposition of particles on the stoss side, in turn caused by increasing flow thickness and decreasing flow velocity on the stoss (flow expansion). The inverse happens on the lee side.

Unlike other bedforms, these UMA show upward coarsening (or sorting over the length of individual bedforms), resulting from the upstream migration of the bedform with coarser particles depositing on the stoss side and crest, and finer material on the lee side and trough. For experiments with sediment P4, d_{50} on the UMA crests were ~ 15–20 %

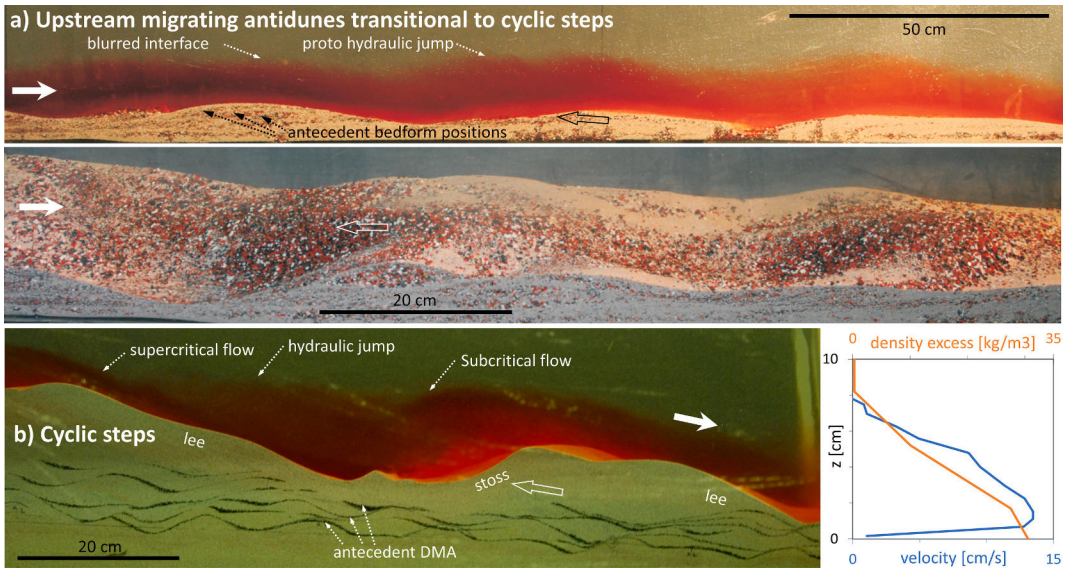

Fig. 8. a) Upstream-migrating antidunes before morphing into cyclic steps, formed by saline current: side view photo during experiment with current interface in phase with bedforms (top), top-side view photo after experiment with coarser particles deposited on the stoss and crest (bottom). From experiment SW2–12 (Spinewine et al., 2010), with bed material M1, bed slope S = 7.6 %, and Froude number $Fr_d \sim 1.48$ ($Fr_{db} \sim 2.07$). b) Cyclic steps formed by saline current: side view during experiment shows current flowing over the steps with supercritical flow over lee side, followed by a hydraulic jump and subcritical flow over the stoss side (left), and velocity and density profiles of the associated current on a supercritical segment (right). From experiment SW3a (Spinewine et al., 2009), with bed material P2, average bed slope S = 8.5 % and $Fr_d \sim 1.60$–1.80 in the supercritical segment. Filled and empty arrows indicate direction of flow and bedform migration respectively.

coarser than on the troughs (1550 μm vs 1280 μm). Stoss sides coarser than lee sides have been reported in fluvial antidunes (Cheel, 1990; Alexander and Fielding, 1997) as well as in upstream-migrating likely UMA submarine bedforms (e.g. Toyama, Nakajima and Satoh, 2001; Mafate/Saint-Denis, Mazuel et al., 2016; Magdalena, Ercilla et al., 2002a; Orinoco, Ercilla et al., 2002b). However, upward coarsening should not be expected to occur in all these cases, for the coarser material deposition may occur mostly on the proximal part of the stoss side but not on the crest. This instance of upward coarsening was an exception in our dataset, for upward fining was observed in most of our experiments where bed samples were evaluated.

Bed, basal flow, and interface are in phase in UMA. The basal flow is thicker at the crest and thinner at the trough. This is seen in Fig. 7b where the spatial variation of the basal layer over the UMA is visualized by the higher concentration of suspended material near the bed.

Under certain conditions UMA may evolve into cyclic steps (see 7.10). We observed a stage preliminary to this transition under steep bed slopes $S = 7.6$ % with $Fr_d = 1.48$ ($Fr_{db} \approx 2.07$) (Fig. 8a). As the average slope became steeper because of thinning of the deposit downstream, UMA grew in size and steepness until eventually a hydraulic jump appeared. The bed material was coarse and poorly sorted, a mix (M1) of 80 % coarse material and 20 % fine. These transitional UMA, sometimes called breaking antidunes, are very steep ($\zeta = 0.09$), above the average of stable UMA, and still symmetrical ($A \approx$ -0.09) although with a slight upslope asymmetry. The transitional UMA also had upward coarsening, with coarser particles depositing on the stoss and crest and finer material on the lee and trough. Sorting becomes more noticeable when the bed sediment is less uniform.

4.5. Cyclic steps

Cyclic steps (CS) are the largest of all bedforms, they are bounded by hydraulic jumps and migrate upstream. Cyclic steps can evolve from either DMA or UMA, usually with an associated increase in bed slope and Froude number due to gradual thinning of the deposit downstream, even under the same upstream flow boundary conditions. The gradual growth in steepness ζ and negative slope on the stoss side S_s eventually force a hydraulic jump. The transcritical behavior of the flow over the steps directly relates to the mechanism for their upstream migration. Over the lee side the supercritical flow is thin and attached to the bed. Over the trough and stoss side of the step, the subcritical flow is thicker, with a rather horizontal interface with the ambient water. The stoss face is prone to be more irregular than the lee face, favoring detachment, flow separation, eddies and recirculation cells. Sediment is thus trapped and deposited along the stoss side, causing upstream migration of the CS. Once formed, CS are very stable features.

Our cyclic steps were formed with bed sediment P5, P11, P12, P13, P16 and P17, a range of medium-sized plastic sediment. The average bed slope of recorded CS ranged from 5.3 % to 17.6 %. Fig. 8b shows an example of CS that emerged from previously developed smaller DMA with $S \sim 6$ %. Local stoss and lee side slopes may vary significantly. Lee side slopes are very steep ($S \sim 20$ %) guaranteeing supercritical flow development; while stoss slopes can be long and remarkably negatively sloped ($S \sim$ -20 %) thus favoring hydraulic jump formation. The supercritical stretches of CS in our observations had $Fr_d = 1.45$–2.88. The subcritical stretches, more difficult to measure due to the presence of the hydraulic jump, dropped below $Fr_d \sim 0.5$. Because of this, we report characteristic Froude number of CS for the supercritical segment only.

Cyclic steps are very long and steep bedforms (k_b as low as 0.03, ζ as high as 0.21). These CS were mostly upslope asymmetrical, but with the asymmetry parameter A ranging widely from −0.36 to 0.21. Grain size is one of the parameters that determines CS asymmetry (Cartigny, 2012).

Cyclic steps share the upstream migrating pattern of UMA, but they tend to have downstream-upward-fining stratigraphy based on fluvial and turbidity currents experiments (e.g., Cartigny et al., 2014; Ono et al., 2023). This is explained by a combination of the hydraulic jump and the long wavelength of CS. The stoss side of CS has a propensity to accumulate coarser material just downstream of the hydraulic jump around the trough of the CS. Farther downstream along the stoss side the flow starts accelerating toward the crest, becoming thinner and less subcritical, with an increase in shear stress. Hence stoss sides tend to have downstream fining from the trough toward the crest. After several sequences the downstream fining on the stoss side leads to upward-fining trend in the CS stratigraphy (Cartigny et al., 2011; Cartigny

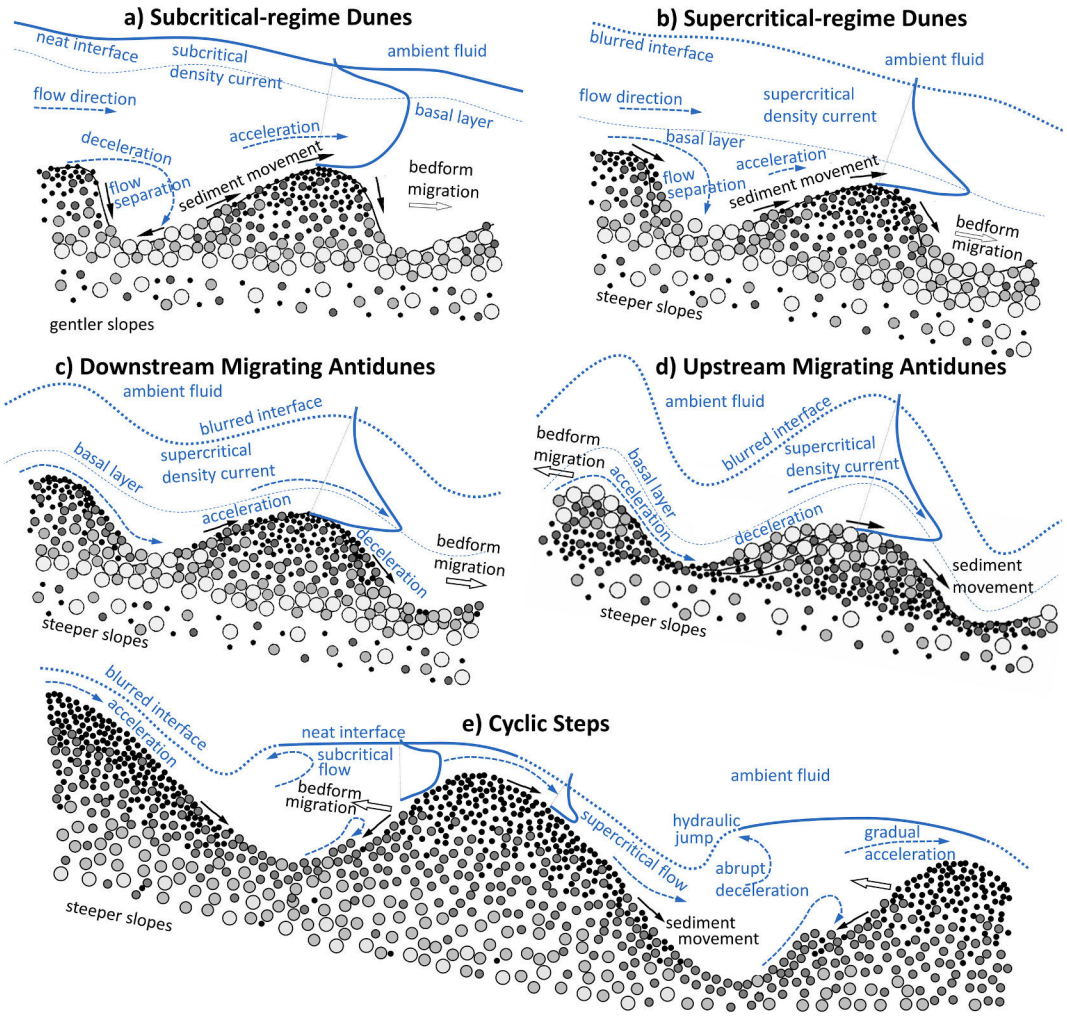

Fig. 9. Sketches of density current, bedform, and sediment vertical grading. a) Subcritical-regime dunes; b) supercritical-regime dunes; c) downstream-migrating antidunes; d) upstream-migrating antidunes; e) cyclic steps. Dunes are formed under subcritical flow regime on gentle slopes, while the other bedforms are observed on steeper slopes under supercritical flow regime. Dunes on both Froude number regimes have flow separation on the lee side, while the more symmetric antidunes do not. The transcritical CS, the largest of all bedforms, are bounded by hydraulic jumps and always migrate upstream. Dunes tend to be very downslope asymmetric, supercritical dunes as well but less so, DMA and UMA are usually symmetric, and CS come in a wide range of (a)symmetry. Dunes are out of phase with interface and basal layer upper surface. SD are unlikely to be in phase with them. DMA and UMA are in phase with both of them. In dunes, SD and DMA the flow tends to be thicker at the trough and thinner at the crest, while the opposite happens in UMA. Flow spatial acceleration/contraction and deceleration/expansion areas are associated with erosion and deposition respectively. Because of differential sediment transport and segregation, and bedform migration, upward fining of sediment is typical for dunes, DMA and CS (albeit for different reasons), while UMA can sometimes have upward coarsening. Ripples (not shown), in either Froude number regime, resemble dunes in all respects but are smaller, form in finer grain sizes, and do not affect the flow interface; they are unlikely to affect the basal layer upper surface either. All these are typical but not exclusive patterns. Sketches are not at scale. Developed based on Blom et al. (2003) sketch for dunes.

et al., 2014; Slootman and Cartigny, 2020; Ono et al., 2023).

4.6. Lower and upper plane bed regimes

In our experiments LPB were observed for both subcritical and supercritical density currents. As in the fluvial case, there seems not to be a one-on-one correspondence between lower/upper bed regime and sub/supercritical Froude number regime, at least not in supercritical saline currents barely capable of moving bed sediment. Some cases with plane bed and significant sediment transport can be classified as UPB, but uncertainty remains for the experimental initial condition was plane bed, and no antecedent bedform field existed to be washed out and confirm upper plane regime.

Fedele et al. (2016) reported UPB when antidunes were washed out under highly supercritical flow conditions ($Fr_d > 2.2$), but no UPB in the transition between dunes and antidunes. In our experiments no transitional or standing waves were clearly observed.

Our observations seem to support Ohata et al. (2022) in that LPB form when sediment particles move only as bed load, while UPB appear under conditions of active suspended load.

5. Bedform classification

The sketch in Fig. 9 summarizes flow characteristics and sediment processes that lead to the formation of the main type of bedforms described in the previous section. These include bed slope and flow regime, thickness and spatial variation of the density current basal layer, phase of bedforms relative to the interface and the basal layer, local acceleration and deceleration along the bedform associated with erosion and deposition zones, flow separation, grain size segregation as well as bedform geometry. We note that while these represent typical but not exclusive features, they facilitate a general understanding and pattern recognition.

In all bedform diagrams described in this section, the classification of

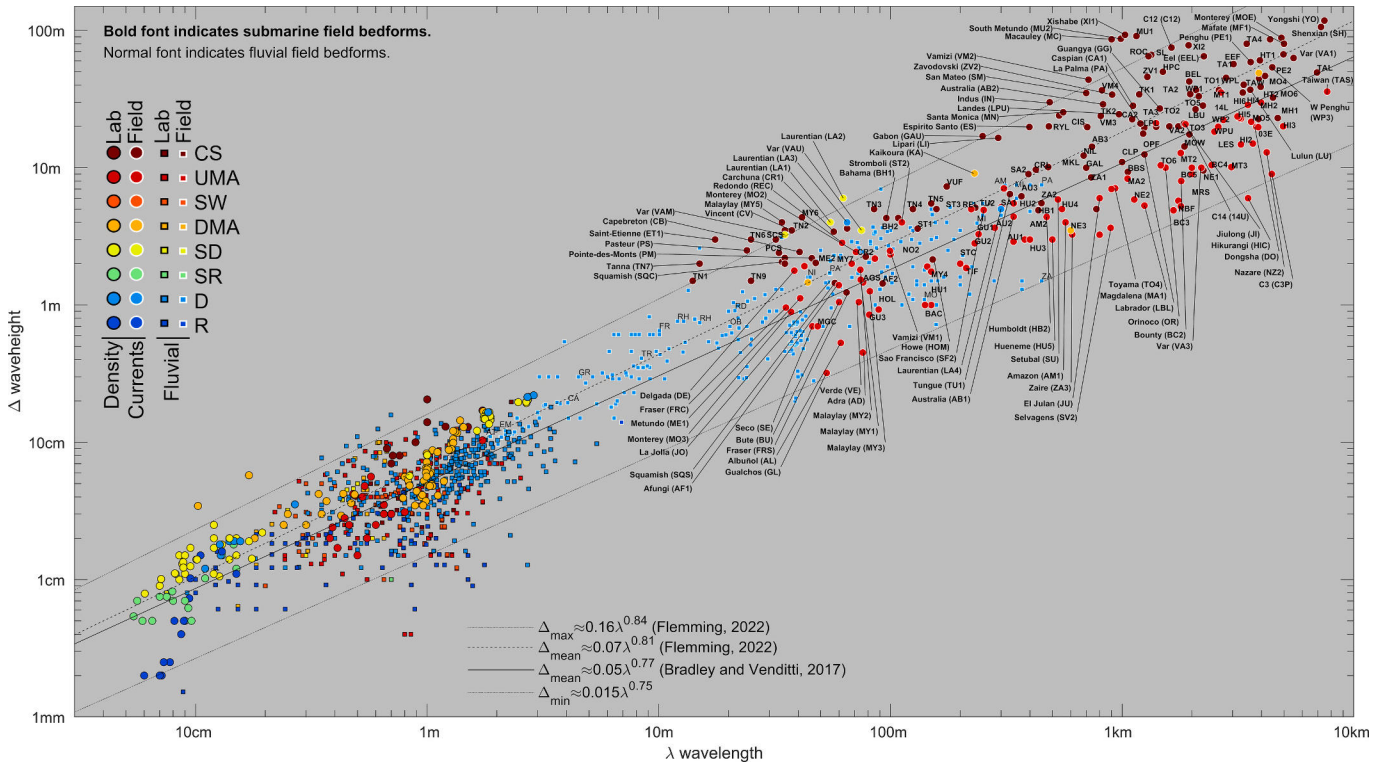

Fig. 10. Bedform waveheight vs wavelength for all bedform types (marker face color), experimental and field sources (marker edge color) induced by both density/turbidity currents and fluvial flows (marker shape). Bradley and Venditti (2017) and Flemming (2022) metric equations are derived mostly for fluvial ripples and dunes. Bold font code indicates submarine field bedform hub and profile (Table 2 and Fig. 19). Normal font indicates fluvial bedforms (Table 3).

flume bedforms is informed by the knowledge provided by observing, measuring and analyzing flows and bedforms during the formative process. Hence while there may be uncertainty in the bedform classification it is considered very low. On the other hand, the interpretation of field-scale bedforms is, in most cases, made without any knowledge of the formative flow conditions. Apart from additional evidence found in the source reference, the classification is informed by a set of criteria derived mostly from the experimental bedforms. The set of criteria to classify bedforms will be explained in greater details in sections 6 and 7.

5.1. *Bedform dimension diagrams*

Characterization of bedform size and some flow parameters is done first by means of diagrams showing the wide range of bedform dimensions spanning several orders of magnitude. Fig. 10 shows bedform wavelength λ against waveheight Δ for all available data together with mean and maximum lines from the equations of Bradley and Venditti (2017) and Flemming (2022). Despite being derived mostly for fluvial ripples and dunes, these lines fit all bedform types very well. The clustering of bedform types is similar at field and laboratory scales. Fig. 11 show dimensionless wavelength and waveheight against basal flow thickness, also highlighting criteria distinguishing ripples from dunes (sections 4.1 and 4.2). Both plots illustrate the scarcity of submarine flow field data compared to fluvial and laboratory flow data. This notwithstanding, the few available datapoints from submarine field environments fit within the same bounds observed for fluvial bedforms.

5.2. *Regime diagrams*

The main objective of bedform diagrams characterizing bedform regime is to provide a link between measurable geometric properties and relevant formative flow parameters. The first example is the diagram in Fig. 12, introduced by Kennedy (1963), where the basal Froude number is plotted against the basal wave number k_b. Density current data fit very well within the original boundaries separating upstream- and downstream-migrating regions derived for fluvial bedforms based on potential flow theory. Importantly, Fig. 12 presents density current data using basal layer metrics (Fr_{db}, k_b), rather than those from the entire current (Fr_d, k). The basal layer of density currents has flow profiles that resemble fluvial flow profiles, for which $k \approx k_b$ and $Fr_d \approx Fr_{db}$. Had the pair (Fr_d, k) been used instead, the match would appear distorted and unconnected to boundaries predicted by fluvial potential flow theory. Furthermore, clustering of different bedform types is neatly shown separating CS, UMA, DMA, SD, SR, R, D from each other, and both density current and fluvial flow bedforms fall in the same fields of the phase diagram. These results strongly support our approach of analyzing density current bedforms using basal flow characteristics rather than the full flow profile.

There seems to be one-on-one correlation between Fr_d and Fr_{db} in the experimental data where full velocity and density profiles are available (Fig. 13a). In the observed range of subcritical regime datapoints $Fr_{db} \propto Fr_d$, whereas in the supercritical regime $Fr_{db} \propto 2Fr_d$. These trends should not be extrapolated though. Whereas for a range of intermediate slopes, previous studies found a dependency of the total Froude number Fr_d on the square root of the bed slope S (Ippen and Harleman, 1952; Middleton, 1966; Komar, 1971; Bo Pedersen, 1980; Stacey and Bowen, 1988), for very gentle and very steep slopes Fr_d grows asymptotically to a constant value dependent on bed roughness and suspended sediment fall velocity (Sequeiros, 2012). The basal Froude number Fr_{db} is also dependent on S and, like in fluvial environments, with no apparent asymptotic limit (Fig. 13b). The transition from sub- to supercritical regime occurs on a slope range between 0.3 % and 1 %. Further reasons for this behavior are discussed in section 7.3.

Fig. 14 shows a regime diagram of basal Froude number Fr_{db} vs dimensionless grain size d^* after Fedele et al. (2016). Clustering of bedform types is also apparent, e.g., subcritical ripples tend to form in finer material than dunes. Among supercritical regime bedforms UMA occur across the widest range of grain sizes, with a fair overlap with

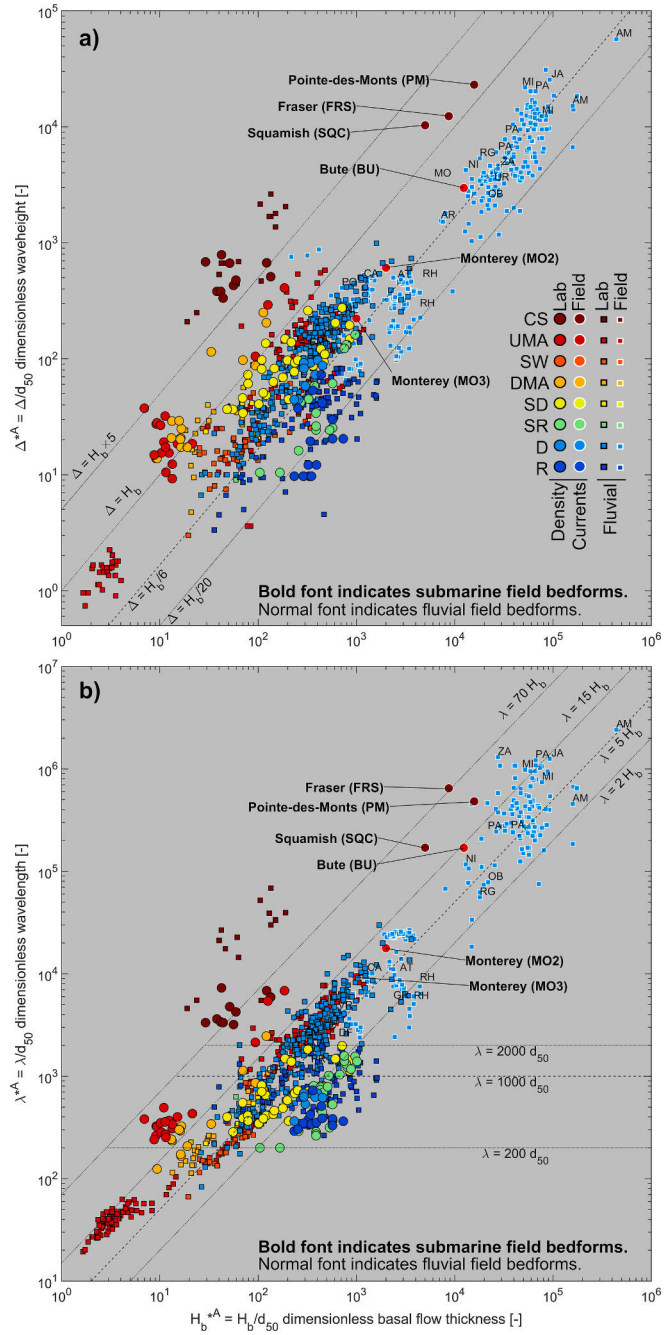

Fig. 11. a) Dimensionless bedform waveheight vs basal flow thickness. The Yalin-Best threshold of $\Delta/H_b = 1/6$ is part of the criteria to set ripples and dunes apart. Cyclic steps have the largest Δ/H_b ratios and ripples the smallest. Normal font indicates fluvial bedforms (Table 3). b) Dimensionless bedform wavelength vs basal flow thickness. The Yalin-Allen threshold of $\lambda/d_{50} = 1000$ (with a ceiling of 2000) is part of the criteria to set ripples and dunes apart. Dune's wavelengths scale with flow depth as $\lambda/H_b \sim 5$ (Allen, 1970) and it can also be used as a criterion to set them apart. Cyclic steps have the largest λ/H_b ratios and ripples the smallest. Bold font code indicates submarine field bedform hub and profile (Table 2 and Fig. 19). Normal font indicates fluvial bedforms (Table 3).

DMA. Supercritical ripples and dunes cluster on the fine-medium sand range together with CS, with the latter, however, having higher Froude numbers. The reasons for overlapping include the role of bed shear stress as well as epistemic and aleatory uncertainty in measurements. Conversely, the lack of bedform types in certain areas of the diagram may simply be a case of availability bias.

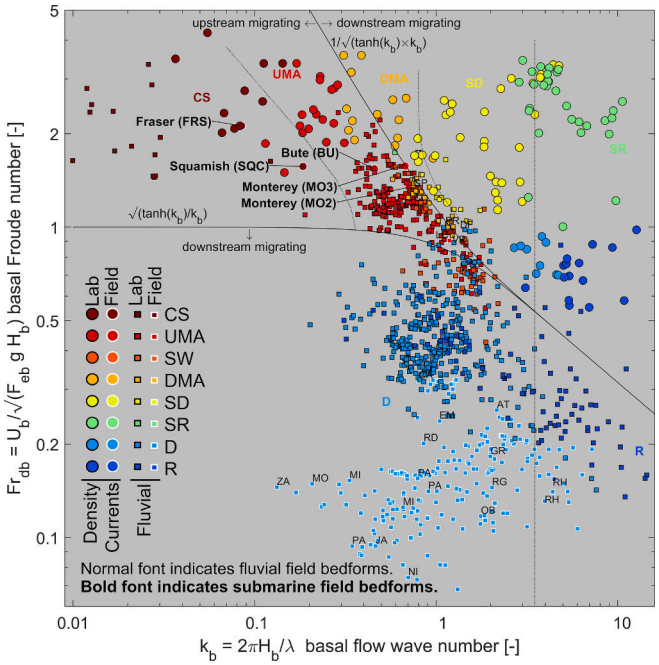

Fig. 12. Kennedy-type bedform regime diagram showing basal Froude number versus basal wave number (note that for fluvial cases $k \approx k_b$, and $Fr_d \approx Fr_{db}$). For cyclic steps the indicated Froude number is at the supercritical segment. Cyclic steps have the smallest wave numbers and ripples the largest. Fluvial and density current bedform types cluster together in the same regions. Bold font code indicates submarine field bedform hub and profile (Table 2 and Fig. 19). Normal font indicates fluvial bedforms (Table 3).

The Shields diagram (Shields, 1936) shows bed shear stress against bedform grain size, with both parameters in dimensionless form (Fig. 15). This type of plot has been the subject of many studies that found distinct regions: no motion, initiation of motion and motion (Mantz, 1977; Parker, 2005), initiation of suspension and prevalence of suspension (van Rijn, 1984; Niño et al., 2003; Bagnold, 1966), and ripple/dune boundaries (e.g., Lapotre et al., 2017).

A similar diagram is produced with the mobility parameter θ'_b of van den Berg and van Gelder (1993) which has the advantage of estimating the bed shear stress by means of depth-averaged flow velocity (of the basal layer for density currents) and a Chézy coefficient related to grain roughness. Cartigny et al. (2014) expanded the diagram to include various kinds of supercritical bedforms (Fig. 1 in Supplementary Material).

There is overall a good match in τ^*-Re_p and θ'_b-d^* spaces for most density current bedforms. However, there is also a fair amount of overlap among bedform types. This should not come as a surprise because larger values of τ^* and θ'_b indicate larger velocities, that can be achieved by a) increasing the discharge for a given slope, or b) increasing the slope for a given discharge. For example, two very different density currents, one supercritical and another subcritical, moving over the same material can induce a similar shear stress (see section 7.5). Slope and its dependent parameter, Froude number, are not directly accounted for in the Shields or mobility parameter diagrams. No matter how large the discharge is, supercritical flow will not develop for $S < 0.3$ %; and no matter how low the discharge is, subcritical flows rarely occur for $S > 1$ % (Fig. 13b). In short, Froude and Shields numbers are not interchangeable. Hence the Shields or mobility parameter diagrams should be viewed together with the Fr_{db}-d^* diagram (Fig. 14). This would call for a τ^*-Fr_{db}-d^* 3D phase diagram. Yet given the unique role flow density plays in density currents (see section 7.4), a more comprehensive regime diagram for density currents should also include the fractional excess density, making it a 4D space. This goes beyond the

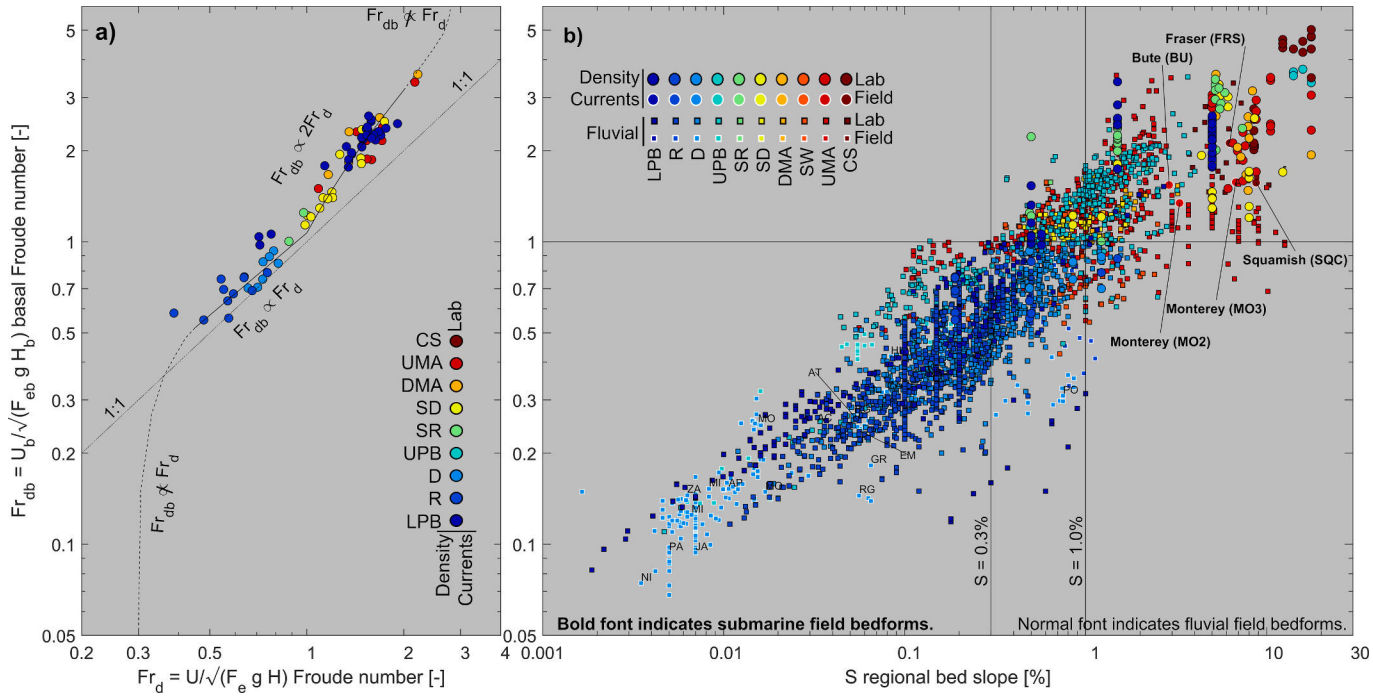

Fig. 13. a) Density current total Froude number Fr_d against basal Froude number Fr_{db} from experimental observations. Dashed lines indicate expected Fr_d asymptotic behavior on very gentle and very steep slopes for turbidity currents. b) Regional bed slope (average over a train of bedforms) against basal Froude number. Supercritical flows have not been observed for $S < 0.3$ %; and subcritical flows rarely occur for $S > 1$ %. Despite the spread, caused by bed roughness and properties of suspended material, there is a strong connection between bed slope and basal Froude number, which warrants using the slope as a first order proxy for the Froude number when no flow data is available. Bold font code indicates submarine field bedform hub and profile (Table 2 and Fig. 19). Normal font indicates fluvial bedforms (Table 3).

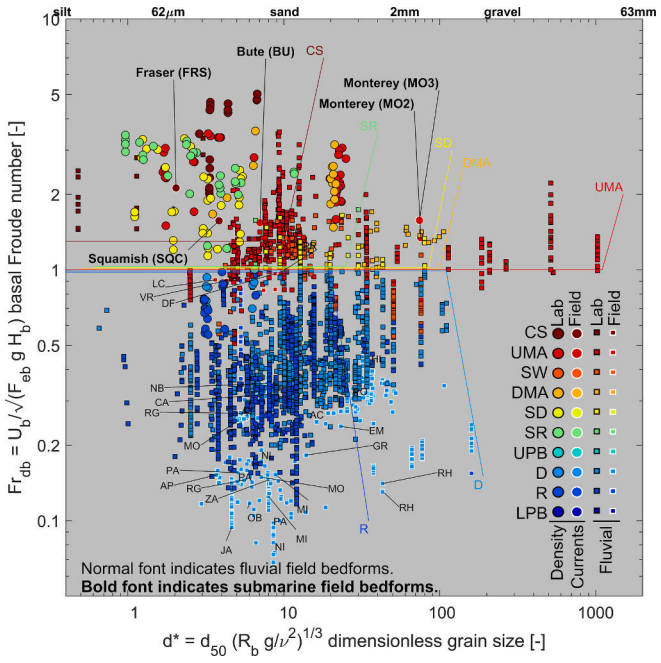

Fig. 14. Basal Froude number vs dimensionless grain size. In both Froude number regimes ripples develop for finer material than dunes. Upstream migrating antidunes are observed to occur under a wide range of grain sizes. Cyclic steps usually develop for fine grain sizes. Bold font code indicates submarine field bedform hub and profile (Table 2 and Fig. 19). Normal font indicates fluvial bedforms (Table 3).

scope of this study, because at least an order of magnitude more datapoints would be needed.

Ohata et al. (2017) proposed a 3D regime diagram based on dimensionless grain size d*, flow thickness $H_b{}^{*B}$ and flow velocity $U_b{}^{*B}$, (for definitions see Notation), in which we have used the basal flow properties for density current bedforms. While the range of grains sizes covers only fine, medium and coarse sand, the available density current data points sit well within their corresponding boundaries (see Fig. 2 in Supplementary Material).

Fig. 16 is a new type of regime diagram based on the bedform asymmetry parameter A, and where the flow component comes in the form of the basal wavenumber k_b. The observed clustering shows a gradual shift across the entire spectrum of possible bedforms, with overlap dependent on bedform type and data availability.

5.3. *Dimensionless flowless diagrams*

The main objective of the dimensionless diagrams introduced in Fig. 17 and Fig. 18 is to identify bedforms based purely on geometry and slope setting, where there is no flow data to assess Froude, Shields or wavenumber. They are particularly useful for distinguishing field-scale bedforms, including observations from the modern seabed and ancient cases in outcrop or the subsurface—provided the original bed slope has not been significantly tilted or distorted. Bedform asymmetry A against steepness ζ is shown in Fig. 17, and bedform stoss slope S_s against regional or average bed slope S is seen in Fig. 18. Both have distinctive clustering and show gradual shift through bedform types. Fig. 18 sets the basis for a novel approach to tell UMA from CS when positive stoss slope conditions are met (see also section 7.9).

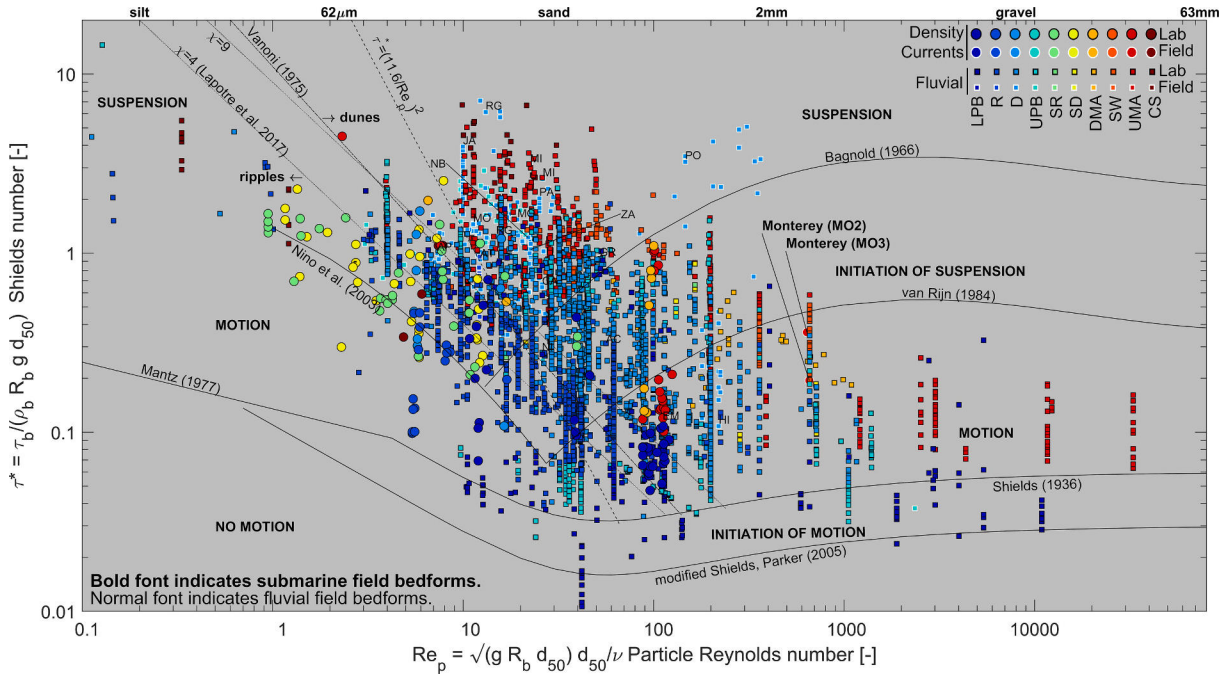

Fig. 15. Dimensionless shear stress vs particle Reynolds number. The Shields diagram shows regions of mobility for different grain sizes and magnitude of shear stress. Lines indicate thresholds of motion and suspension, and criteria to distinguish ripples from dunes based on shear stress (Vanoni, 1975; Lapotre et al., 2017; and viscous sublayer). Criteria relying on bedform dimensions are not visible in this diagram. Bold font code indicates submarine field bedform hub and profile (Table 2 and Fig. 19). Normal font indicates fluvial bedforms (Table 3).

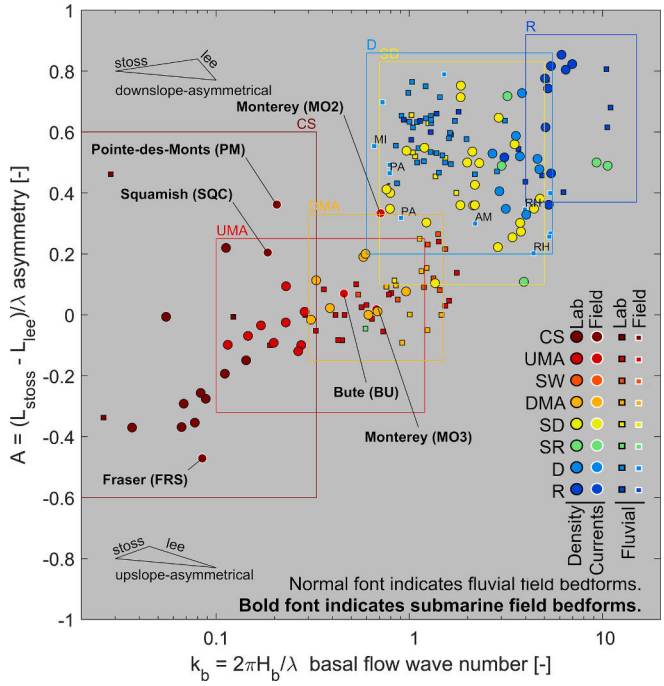

Fig. 16. Bedform asymmetry vs basal flow wave number. Even without flow observations, basal flow number can sometimes be inferred from features on the canyon side walls, such as in the Pointe-des-Monts Canyon (Normandeau et al., 2022), facilitating the identification of the likely bedform type when bedform characteristics, such as asymmetry, are available. Bold font code indicates submarine field bedform hub and profile (Table 2 and Fig. 19). Normal font indicates fluvial bedforms (Table 3).

6. Field-scale density current bedforms

6.1. Locations and settings

Fig. 19 and Table 2 show locations and characteristics of submarine bedforms observed in canyons and channels **(C)**, channel levees **(L)**, slopes / rises / basins **(S)**, fans and islands **(F)**. These categories aim to characterize whether the bedforms are confined or not, and if the latter what type of unconfinement it is. Canyons and valleys provide a degree of lateral confinement. When bedform width (along crest length) is of the same order of canyons width they are said to be confined. In wide canyons and valleys such as the Laurentian, where bedform width is smaller than that of the valley, confinement would seem less relevant; however in many wide valleys bedforms still are found confined within narrow and shallow corridors that probably predate the location of future channels (e.g., Laurentian, Chenal Vincent in La Réunion) hence we classify them as canyons or channels (C). Levees and flanks (L); slopes, rises and basins (S); and fans (F); all provide unconfined environments for bedform development. Bedforms in prodeltas may be confined or unconfined, and may be found in fan-like settings. A distinction setting apart fans and bedform fields around small volcano islands from other unconfined settings is pertinent because they are typically defined by radial bathymetry and lateral flow expansion, which may give the misleading impression of the overlaid bedforms having concave upward shapes, and thus migrating downstream (see section 7.14).

In field surveys bedform dimensions and bed slope are the most accessible data. In many of them there are also sediment samples and seismic/sub-bottom profiles from which bedform migration history can be inferred. However, turbidity current observations in tandem with associated bedforms remain relatively scarce despite a handful of studies in the last two decades. This is particularly true because detailed observations characterizing flow properties in a manner equivalent to lab experiments with full velocity and density profiles are very rare.

When interpreting the field bedforms discussed in this section, keep in mind that without a reliable, concurrent dataset encompassing flow,

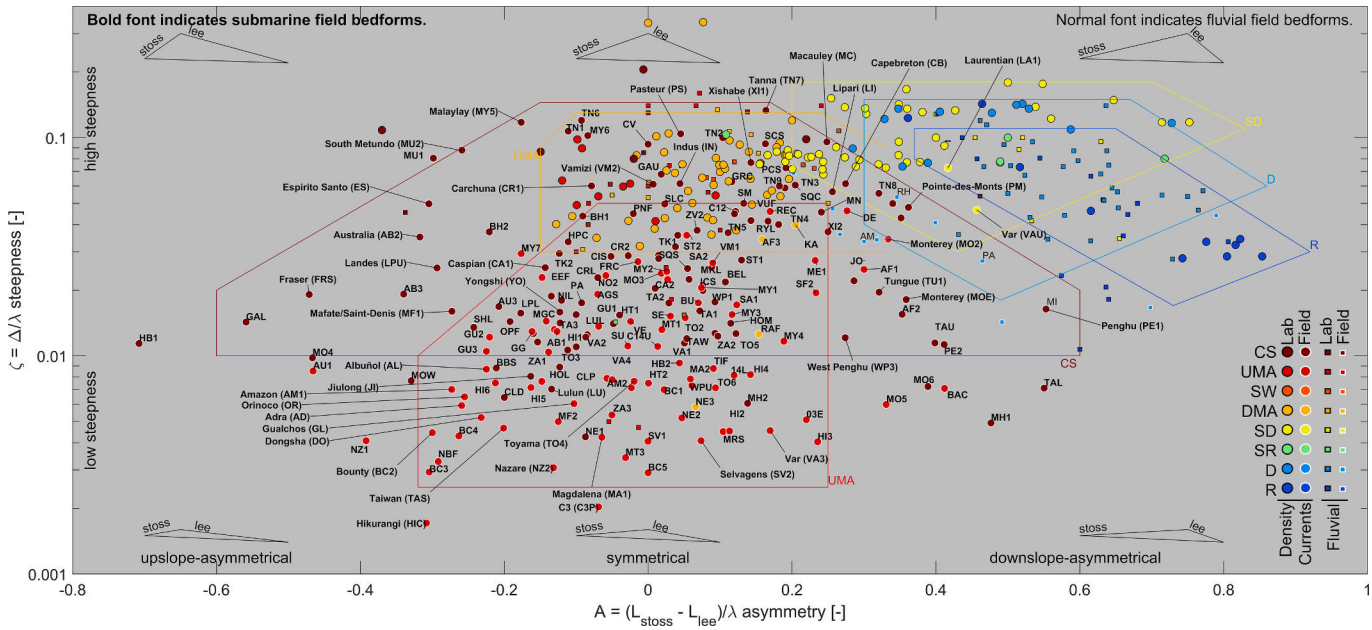

Fig. 17. Bedform asymmetry vs steepness. Ripples and dunes, in both Froude number regimes, are downslope asymmetrical and with intermediate to high steepness. Cyclic steps have the widest range of asymmetry among bedforms, with intermediate to high steepness. Upstream migrating antidunes are symmetrical, or slightly upslope asymmetrical; and have low to intermediate steepness, but their steepness increases before transitioning to CS. Downstream migrating antidunes are symmetrical or slightly downslope asymmetrical and tend to have intermediate to high steepness. Bold font code indicates submarine field bedform hub and profile (Table 2 and Fig. 19). Normal font indicates fluvial bedforms (Table 3).

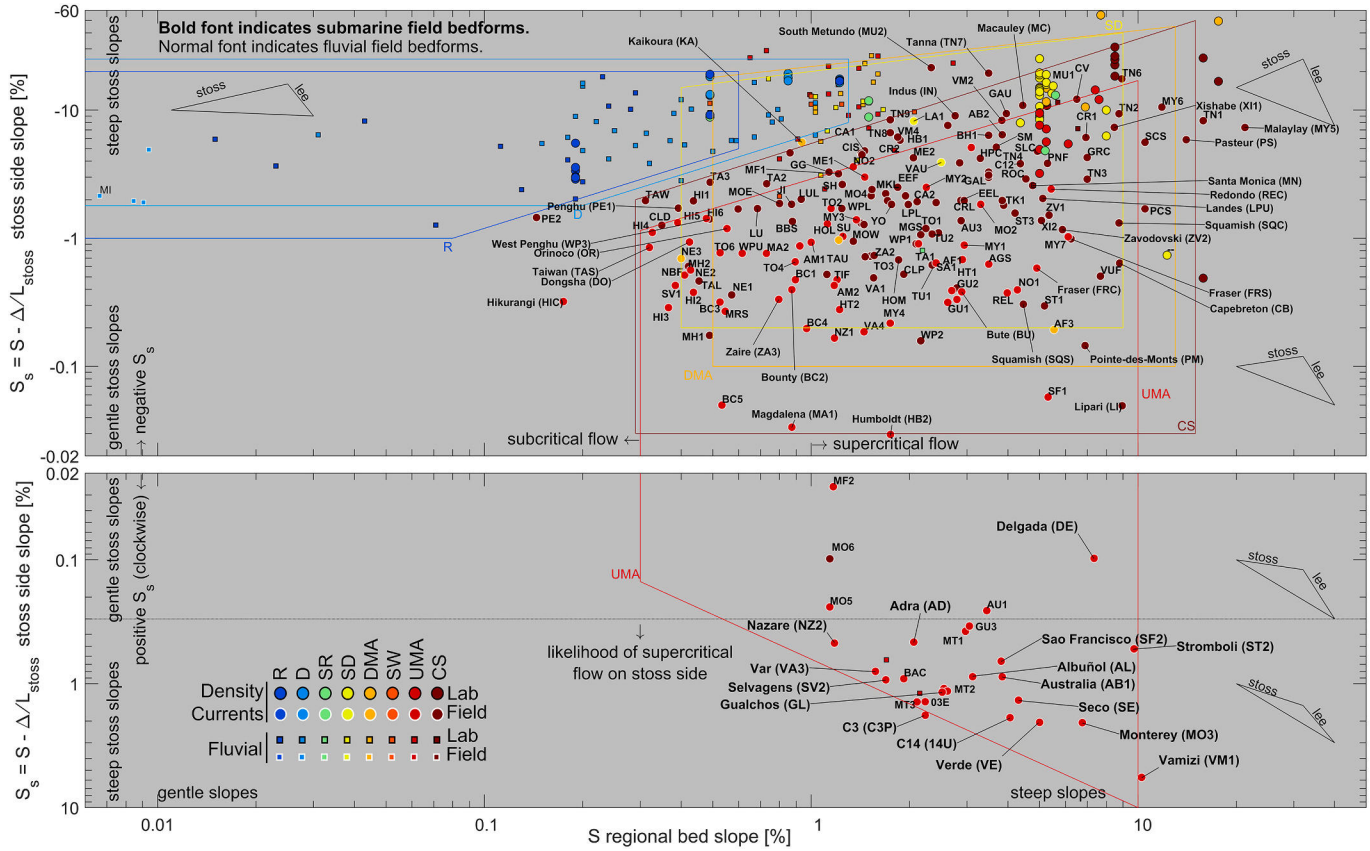

Fig. 18. Bedform stoss slope against regional bed slope. Subcritical ripples and dunes develop over gentle slopes and have characteristic negative stoss slopes. Supercritical bedforms develop on steeper slopes, but more often than not they also have negative stoss slope. Positive stoss slope steeper than ~0.3 % is arguably an indication of UMA, as opposed to CS, because it deters subcritical flow and the formation of a hydraulic jump. Bedform sketches are only illustrative of regional and stoss slopes, and are not intended to show asymmetry. Bold font code indicates submarine field bedform hub and profile (Table 2 and Fig. 19). Normal font indicates fluvial bedforms (Table 3).

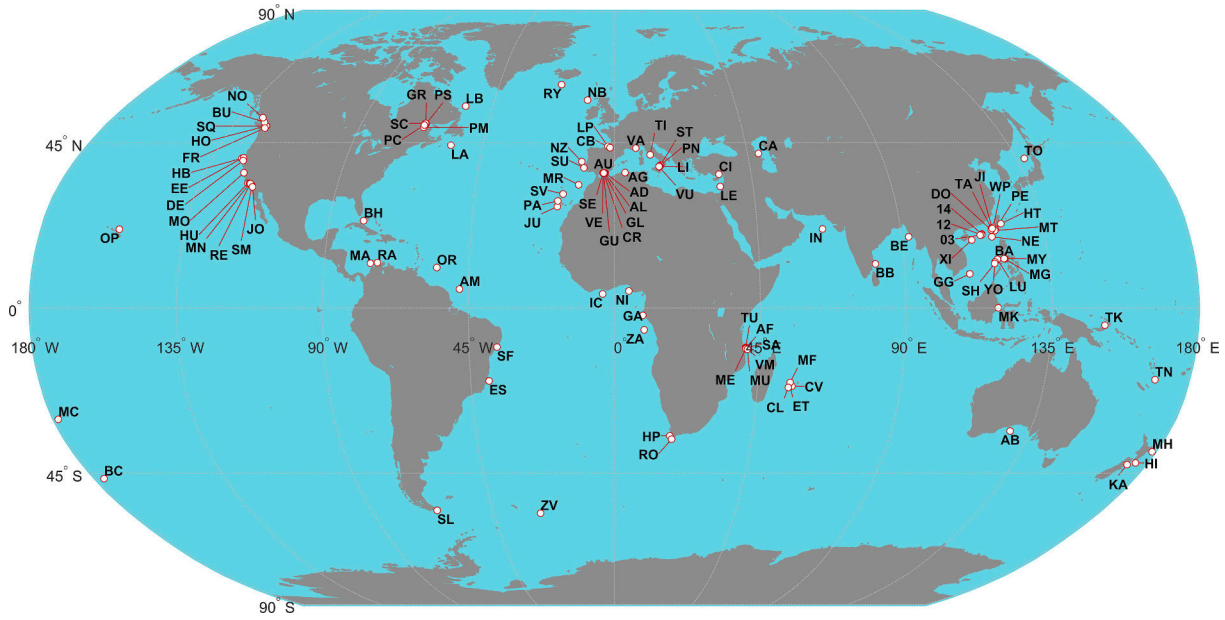

Fig. 19. Locations of hubs where field submarine bedforms have been assessed. They are indicated by a two-letter code. A single hub may contain more than one site where bedforms are recorded, different bedform types (e.g. upstream migrating antidunes and cyclic steps) or settings (e.g. canyon, levee, fan). See section 6 and Table 2 for further details.

bedform, and sediment observations, some uncertainty will persist—regardless of how robust the classification criteria may be. When available, priority was given to the interpretation attempted by the authors of the referenced studies.

The dataset of fluvial field bedforms comes from large rivers as well as smaller rivers and creeks (Table 3) from sources mentioned in section 1.2.

6.2. Estimation criteria

Based on experimental observations depicted from Fig. 10 to Fig. 18 and informed by assessments in source articles, we propose in Fig. 20 a flow diagram to determine bedform types when little or no flow characteristics are available, which is the case for most field observations. The first step in the classification assumes that bedform migration direction is known, either from seismic profiles, multiple bathymetric surveys or bedform curvature in confined channels. Subsequent steps are based on bedform dimensions, asymmetry, steepness, stoss slope, average bed slope acting as a proxy for Froude number (see section 5.2, Fig. 13b), and criteria to distinguish ripples from dunes described in sections 2.2 and 4.1.

The asymmetry parameter range is $-1 < A < 1$. When the absolute value is $|A| < 0.1$ the bedforms are considered nearly symmetrical (stoss length ≈ lee length), and when $|A| < 0.2$, they are considered weakly asymmetrical (van Landeghem et al., 2012; Ma et al., 2019). Values of $A > 0.2$ indicate downslope asymmetrical bedforms (stoss side longer than lee side). Values of $A <$ -0.2 correspond to upslope asymmetrical bedforms (stoss side shorter than lee side). For this study, we consider bedforms with $|A| < 0.2$ to be symmetrical. Regardless of Froude number regime, ripples and dunes are downslope asymmetrical. UMA and DMA tend to be symmetrical, and CS are found through a wide spectrum of asymmetry. UMA are low steepness elongated bedforms typically with $\zeta < 0.05$. DMA, UMAT and CS are on average steeper than UMA. Dunes are steeper than ripples, but there is significant overlap.

In our dataset UMA are the bedforms with almost all instances of positive stoss slope. This feature tells them apart from CS, for the latter have mostly marked negative stoss slopes essential to create the hydraulic jump and transcritical flow. The occurrence of positive stoss slope in other supercritical regime bedforms such as SD cannot be ruled out.

Density currents and fluvial flow observations indicate that supercritical flows need at least an average bed slope S steeper than ~0.3 %, and that subcritical density currents are unlikely to exist for S steeper than ~1.0 %.

Ripples and dunes are set apart first by means of what we call the Yalin-Allen threshold of $\lambda/d_{50} = 2000$ and the Yalin-Best threshold of $\Delta/H_b = 1/6$, and in those cases where these criteria cannot be implemented due to lack of data, by means of the Lapotre et al. (2017) criteria based on the Yalin number $\chi = Re^* \sqrt{\tau^*}$. The rationale for such an order is pragmatic, prioritizing the type of information that is more likely to be available, and the fact that bed shear stress estimation is more difficult in density currents than in fluvial flows.

The simple rules in Fig. 20 should not be taken dogmatically and should always be validated by flow conditions whenever possible. Furthermore, for the bed slope range of 0.3–1.0 % where both Froude number regimes overlap (Fig. 13b) it is not possible with these simple rules to make further distinctions between subcritical and supercritical ripples/dunes unless flow conditions are known.

When migration direction is unknown -such as when only a single bathymetry dataset is available- additional features like bedform concavity can aid in identifying bedforms (see section 7.14).

In the next sections we go through some characteristic cases and use the flow diagram to inform the process of inferring bedform types.

6.3. Cyclic steps

To induce a hydraulic jump some significant perturbation or obstruction to the flow is needed, whether in the form of a long stoss side with (usually) gentle negative slope that forces the jump because of the abrupt slope change on the lee-stoss boundary, or a short stoss side with steep negative slope resulting in a large waveheight that acts as an obstacle. This obstruction must be considered *relative* to the flow thickness. Hence without actual flow observations there will always be uncertainty to distinguish between CS and UMA.

Given that turbidity currents are often transient and unsteady, flow thickness is expected to change within a given event. Thus, a given bedform may behave both as CS and UMA depending on flow stage: waxing, peak or waning. The intra-event variability also applies between

Table 2
Summary of submarine field bedforms. Hub code indicates site (see map in Fig. 19). Profile specifies in-hub location, when more than one set of bedforms is assessed within a hub. Setting can be canyons or channels (**C**), levees and flanks (**L**), slopes, rises, valleys and basins (**S**), fans and islands (**F**).

Source	Site	Description	Hub	Profile	Setting	Interpreted bedform type
Zhou et al. (2021)	C3 Canyon South China Sea	Present, Zhou Table 1 and Fig. 4	03	P	C	UMA
Zhou et al. (2021)	C3 Canyon South China Sea	PGM, Zhou Table 1 and Fig. 4	03	E	C	UMA
Li et al. (2019)	C12 Canyon South China Sea	Lower thalweg	12	–	C	CS
Sun et al. (2023)	C14 Canyon South China Sea	Upper	14	U	C	UMA
Sun et al. (2023)	C14 Canyon South China Sea	Lower	14	L	C	UMA
Anderskouv et al. (2010)	Great Australian Bight	Eastern lower (A)	AB	1	S	UMA
Anderskouv et al. (2010)	Great Australian Bight	Eastern middle (B—I)	AB	2	S	CS
Anderskouv et al. (2010)	Great Australian Bight	Western middle (Bw-Ew)	AB	3	S	CS
Bárcenas et al. (2009), Urgeles et al. (2011)	Adra Prodelta	Table III and Table 1 in refs.	AD	–	S	UMA
ENI (unpub.)	Afungi Canyon	Middle	AF	1	C	UMA
ENI (unpub.)	Afungi Canyon	Distal	AF	2	C	CS
ENI (unpub.)	Afungi Canyon	Distal	AF	3	C	DMA
Urgeles et al. (2011)	Algerian Shelf	Fig. 7	AG	–	S	UMA
Bárcenas et al. (2009), Urgeles et al. (2011)	Albuñol Prodelta	Table III and Table 1 in refs.	AL	–	F	UMA
Flood et al. (1995)	Amazon Canyon levee	930	AM	1	L	UMA
Flood et al. (1995)	Amazon Canyon levee	933	AM	2	L	UMA
Muñoz et al. (2017)	Almuñecar Canyon	Profile B West	AU	1	C	UMA
Muñoz et al. (2017)	Almuñecar Canyon	Profile A East Up	AU	2	C	UMA
Muñoz et al. (2017)	Almuñecar Canyon	Profile C East down	AU	3	C	CS
Sequeiros et al. (2019)	Baco Canyon	Depth ~ 324-333 m	BA	–	C	UMA
Kolla et al. (1976)	West Bengal Slope	Type III profile $_{\text{Fig. 8}}$c	BB	–	S	CS
Carter et al. (1990)	Bounty Channel levee	Fig. 4 large	BC	1	L	UMA
Carter et al. (1990)	Bounty Channel levee	Fig. 4 mean	BC	2	L	UMA
Carter et al. (1990)	Bounty Channel levee	Fig. 4 small	BC	3	L	UMA
Carter et al. (1990)	Bounty Channel levee	Fig. 3 large	BC	4	L	UMA
Carter et al. (1990)	Bounty Channel levee	Fig. 3 small	BC	5	L	UMA
Lu et al. (2021)	Upper Bengal Fan canyon flank	SW1, western flank	BE	–	L	CS
Wunsch et al. (2017), Schnyder et al. (2018)	Western Great Bahama Bank	Continuous wave fields in 2 deg. slopes	BH	1	S	CS
Wunsch et al. (2017), Schnyder et al. (2018)	Western Great Bahama Bank	Lower slope with gullies	BH	2	S	CS
Zeng et al. (1991), Heijnen et al. (2020), Chen et al. (2021)	Bute Inlet	Mid-reach	BU	–	C	UMA
Levchenko and Roslyakov (2010) and Sorokin and Roslyakov (2019)	Caspian Sea Western Slope	Figs. 2, 5	CA	1	S	CS
Levchenko and Roslyakov (2010) and Sorokin and Roslyakov (2019)	Caspian Sea Western Slope	Fig. 8	CA	2	S	CS
Mazières et al. (2014), Guiastrennec-Faugas et al. (2020)	Capebreton Canyon	Head, profile C′	CB	–	C	CS
Ediger et al. (2002)	Cilician Basin	Upper slope, Fig. 2.	CI	–	S	CS
Sisavath et al. (2011)	Cilaos Fan proximal (slope like), SW La Réunion Island	Profile C—D Fig. 6	CL	P	S	CS
Sisavath et al. (2011)	Cilaos Fan distal (slope like), SW La Réunion Island	Profile *E*-F Fig. 6	CL	D	S	CS
Cerrillo-Escoriza et al. (2024)	Carchuna Canyon	Upper segment, Table 1 and Fig. 3	CR	1	C	CS
Cerrillo-Escoriza et al. (2024)	Carchuna Canyon	Lower segment, Table 1 and Fig. 3	CR	2	C	CS
Cerrillo-Escoriza et al. (2024)	Carchuna Canyon levee	Eastern levee, Fig. 10	CR	–	L	CS
Ollier et al. (1998), Saint-Ange et al. (2013)	Chenal Vincent	Upper northern valley	CV	–	C	CS
Smith et al. (2018)	Delgada Canyon	Fig. S3	DE	–	C	UMA
Kuang et al. (2014)	Dongsha Canyon levee	Western levee	DO	–	L	UMA
Lamb et al. (2008)	Eel Fan	Profile 2	EE	–	F	CS
Lamb et al. (2008)	Eel Fan levee	Distributary channel	EE	–	L	CS
Heiniö and Davies (2009)	Espirito Santo Channel	S.I. Table 1	ES	–	C	CS
Babonneau et al. (2013)	Saint-Etienne Canyon	Tributary canyon S2, S3, S4, S5 in Fig. 4	ET	1	C	CS
Babonneau et al. (2013)	Saint-Etienne Canyon	Etang-Sale sector tributary canyons S4, S5, S6 in Fig. 3	ET	2	C	CS
Hill (2012), Lintern et al. (2016)	Fraser Delta	Channel northern branch	FR	–	C	UMA
Hill (2012), Lintern et al. (2016)	Fraser Delta	Non-channeled slope	FR	–	S	CS
Lonergan et al. (2013)	Margin of Gabon	Lower slope	GA	L	S	CS
Lonergan et al. (2013)	Margin of Gabon	Upper slope	GA	U	S	CS
Zhang et al. (2024), Zhong (2025)	Guangya Channel	Channel 3, Fig. 1D Table S1	GG	–	C	CS
Bárcenas et al. (2009), Urgeles et al. (2011)	Gualchos Prodelta	Table III and Table 1 in refs.	GL	–	S	UMA
Normandeau et al. (2016)	Gravel Delta	Figs. 5, 6, 7, 8	GR	–	C	CS
Lobo et al. (2015) and Urgeles et al. (2011)	Guadalfeo Prodelta	Western sediment field, Table III and Table 1.	GU	1	S	UMA
Lobo et al. (2015) and Urgeles et al. (2011)	Guadalfeo Prodelta	Eastern sediment field, Table III and Table 1.	GU	2	S	UMA

(*continued on next page*)

Table 2 (*continued*)

Source	Site	Description	Hub	Profile	Setting	Interpreted bedform type
Bárcenas et al. (2009), Urgeles et al. (2011)	Guadalfeo Prodelta	Table III and Table 1.	GU	3	S	UMA
Lee et al. (2002)	Humboldt Slope	Fig. 8	HB	1	S	CS
Lee et al. (2002)	Humboldt Slope	Fig. 9	HB	2	S	UMA
Lewis and Pantin (2002)	Hikurangi Channel levee	SHTL 13a left-bank	HI	2	L	UMA
Lewis and Pantin (2002)	Hikurangi Channel levee	SHTL 13a left-bank	HI	1	L	CS
Lewis and Pantin (2002)	Hikurangi Channel levee	SHTL 11a left-bank	HI	3	L	UMA
Lewis and Pantin (2002)	Hikurangi Channel levee	SHTL 11b left-bank	HI	4	L	UMA
Lewis and Pantin (2002)	Hikurangi Channel	SHTC Foredeep, transition to Cook Canyon	HI	–	C	UMA
Tek et al. (2022)	Hikurangi Channel levee	Wave field 1a axis	HI	5	L	UMA
Tek et al. (2022)	Hikurangi Channel levee	Wave field 2a axis	HI	6	L	UMA
Stacey et al. (2019)	Howe Sound	Upper midslope middle profile A, St2	HO	M	S	CS
Stacey et al. (2019)	Howe Sound	Upper midslope lower profile B, St3	HO	L	S	UMA
Palan (2017)	Hope Canyon	Canyon floor and margins	HP	–	C	CS
Liu et al. (2019)	Huatung Basin	Sediment wave field 1 upper cd	HT	1	S	CS
Liu et al. (2019)	Huatung Basin	Sediment wave field 1 lower cd	HT	2	S	UMA
Normark et al. (2002), Piper and Normark (2001)	Hueneme Canyon levee	l12	HU	1	L	UMA
Normark et al. (2002), Piper and Normark (2001)	Hueneme Canyon levee	l18	HU	2	L	UMA
Normark et al. (2002), Piper and Normark (2001)	Hueneme Canyon levee	l1N	HU	3	L	UMA
Normark et al. (2002), Piper and Normark (2001)	Hueneme Canyon levee	l1mid	HU	4	L	UMA
Normark et al. (2002), Piper and Normark (2001)	Hueneme Canyon levee	l1S	HU	5	L	UMA
Russo et al. (2024)	Ivory Coast Tano Basin	Line 4	IC	–	S	CS
Haq et al. (2021, 2023)	Indus Canyon levee	Fig. 2	IN	–	L	CS
Zhong (2025)	Jiulong Fan	Fig. 1C Table S2	JI	–	F	CS
Paull et al. (2013)	La Jolla Canyon	Canyon floor	JO	–	C	–
Wynn et al. (2000a)	El Julan (channelized slope)	Figs. 7 and 8	JU	–	C	UMA
Mountjoy et al. (2018), Lewis and Barnes (1999)	Kaikoura Canyon	Lower segment	KA	–	C	DMA
Piper et al. (1985), Hughes Clarke et al. (1990)	Laurentian Fan Eastern Valley	Upper part 2-3 km wd	LA	1	C	SD
Piper et al. (1988), Hughes Clarke et al. (1990)	Laurentian Fan Eastern Valley	Upper part 2-3 km wd	LA	2	C	SD
Piper et al. (1988), Hughes Clarke et al. (1990)	Laurentian Fan Eastern Valley	Middle-lower part, East branch	LA	3	C	D
Piper et al. (1988), Hughes Clarke et al. (1990)	Laurentian Fan Eastern Valley	Lower part, South branch termination	LA	4	C	D
Praeg and Schafer (1989)	Labrador Sea Slope	Upper	LB	U	S	CS
Praeg and Schafer (1989)	Labrador Sea Slope	Lower	LB	L	S	CS
Schattner and Lazar (2016)	Levant Slope	Profile in Fig. 7	LE	–	S	UMA
Casalbore et al. (2014)	Lipari West flank	Bf6	LI	–	C	CS
Faugères et al. (2002)	Landes Plateau	Upper slope	LP	U	S	CS
Faugères et al. (2002)	Landes Plateau	Lower slope	LP	L	S	CS
Zhong (2025)	Lulun Canyon	Fig. 1E Table S1	LU	–	C	CS
Zhong (2025)	Lulun Canyon levee	Right Hand levee, Fig. 1E Table S2	LU	–	L	CS
Ercilla et al. (2002a)	Magdalena Fan	Figs. 4, 5, 6	MA	1	F	UMA
Bouma and Treadwell (1975)	Magdalena Fan	2B	MA	2	F	UMA
Pope et al. (2018)	Macauley Volcano submerged caldera	Wave field on the SW slope	MC	–	F	CS
ENI (unpub.)	Metundo Canyon	Distal	ME	1	C	UMA
ENI (unpub.)	Metundo Canyon	Distal	ME	2	C	CS
Mazuel et al. (2016)	Mafate/Saint-Denis Fan	Upper	MF	1	F	CS
Mazuel et al. (2016)	Mafate/Saint-Denis Fan	Lower	MF	2	F	UMA
Porcile et al. (2020)	Magasawang-Tubig Channel	Depth 175 m	MG	–	C	UMA
Porcile et al. (2020)	Magasawang-Tubig Slope	Profile II-II', wd ~ 190 m	MG	–	S	UMA
Shorrock et al. (2025)	Mahia Canyon lower slope	Upper profile Fig. 5D	MH	1	S	CS
Shorrock et al. (2025)	Mahia Canyon lower slope	Lower profile Fig. 5D	MH	2	S	CS
Posamentier et al. (2000)	Makassar Strait levee	Northern overbank, left levee Fig. 6 and 7	MK	–	L	CS
Tubau et al. (2015)	Santa Monica Canyon slope	Canyon flank Fig2 and 7e	MN	–	S	CS
Xu et al. (2014), Paull et al. (2010, 2011)	Monterey Canyon	TC2 R2 1020 m wd	MO	2	C	UMA
Xu et al. (2014), Paull et al. (2010, 2011)	Monterey Canyon	TC2 R3 1445 m wd	MO	3	C	UMA
Wolfson-Schwehr et al. (2023)	Monterey Canyon	Upper canyon 260-310 m wd	MO	1	C	UMA
McHugh and Ryan (2000)	Monterey Canyon levee	Shepard meander Fig. 6 a-a'	MO	4	L	CS
McHugh and Ryan (2000)	Monterey Canyon levee	Shepard meander Fig. 9 a-a' upper	MO	5	L	UMA
McHugh and Ryan (2000)	Monterey Canyon levee	Shepard meander Fig. 9 a-a' lower	MO	6	L	CS
Normark et al. (1980, Normark et al. (2002)	Monterey Fan	Western levee of Monterey Fan, Fig. 4	MO	W	F	CS
Fildani et al. (2006)	Monterey East Channel	Profile Fig. 3	MO	E	C	CS
Jacobi et al. (1975)	Moroccan Rise	Fig. 2	MR	–	S	UMA
Damuth (1979)	Manila Trench Valley	Profile A	MT	1	S	UMA
Damuth (1979)	Manila Trench Valley	Profile D	MT	2	S	UMA

(*continued on next page*)

Table 2 (*continued*)

Source	Site	Description	Hub	Profile	Setting	Interpreted bedform type
Damuth (1979)	Manila Trench Valley	Profile C	MT	3	S	UMA
Chen et al. (2024)	South Metundo Canyon	Upper axial zone, Table 1 and Fig. 6	MU	1	C	CS
Chen et al. (2024)	South Metundo Canyon	Lower axial zone, Table 1 and Fig. 6	MU	2	C	CS
Sequeiros et al. (2019)	Malaylay Canyon	Channel 2 A-A' wd ~ 180 m	MY	1	C	UMA
Sequeiros et al. (2019)	Malaylay Canyon	Channel 2C-C′ wd ~ 300 m	MY	3	C	UMA
Sequeiros et al. (2019)	Malaylay Canyon	Channel 2 B-B′ wd ~ 250 m	MY	2	C	UMA
Sequeiros et al. (2019)	Malaylay Canyon	Main channel wd > 300 m	MY	4	C	UMA
Sequeiros et al. (2019)	Malaylay Canyon	Channel 4 wd ~ 60 m	MY	5	C	CS
Sequeiros et al. (2019)	Malaylay Canyon	Channel 4 wd ~ 110-115 m	MY	6	C	CS
Sequeiros et al. (2019)	Malaylay Canyon	Channel 4 wd ~ 230 m	MY	7	C	UMA
Howe (1996)	Rockall Trough North Barra Fan	Gwaelo sequence	NB	–	F	UMA
Wang et al. (2025) submitted	South China Sea NE Lower Slope	Field 2, Fig. 3B	NE	1	S	CS
Wang et al. (2025) submitted	South China Sea NE Lower Slope	Field 2, Fig. 3B	NE	2	S	UMA
Wang et al. (2025) submitted	South China Sea NE Lower Slope	Field 1, Fig. 3A	NE	3	S	DMA
Normark et al. (2002), also Heiniö and Davies (2009)	Nigeria Canyon levee	Bonga block OPL 212	NI	–	L	CS
Bornhold and Prior (1990)	Noeick Delta Middle Slope	Mid slope, Fig. 10	NO	1	S	UMA
Bornhold and Prior (1990)	Noeick Delta Lower Slope	Lower slope, Fig. 11	NO	2	S	UMA
Arzola et al. (2008), Lastras et al. (2009), Masson et al. (2011a,b)	Nazaré Canyon	Southern margin of lower canyon, upstream bedforms Fig. 8 Arzola	NZ	1	C	UMA
Arzola et al. (2008), Lastras et al. (2009), Masson et al. (2011a,b)	Nazaré Canyon	Southern margin of lower canyon, downstream bedform Fig. 8 Arzola	NZ	2	C	UMA
Eakins and Robinson (2006)	Opana Fan	Fig. 10	OP	–	F	CS
Ercilla et al. (2002b)	Orinoco Southern Valley	Fig. 8	OR	–	S	UMA
Wynn et al. (2000a)	La Palma Slope (fan-like)	Figs. 3 and 4	PA	–	F	CS
Normandeau et al. (2016)	Pentecote Delta	Figs. 5, 6, 7, 8	PC	–	S	CS
Zhang et al. (2022)	Penghu Canyon	Lower 1	PE	1	C	CS
Zhang et al. (2022)	Penghu Canyon	Lower 2	PE	2	C	CS
Normandeau et al. (2014, 2019, 2022)	Pointe-des-Monts Canyon	Main, Fig. 2, Profile F-F′	PM	–	C	CS
Casalbore et al. (2014)	Panarea Island	Northern flank, Bf4	PN	–	F	CS
Normandeau et al. (2016)	Pasteur Delta	Figs. 5, 6, 7, 8	PS	–	S	CS
Bouma and Treadwell (1975)	Rancheria Fan	2C	RA	–	F	DMA
Tubau et al. (2015)	Redondo Canyon	Canyon floor	RE	–	C	UMA
Tubau et al. (2015)	Redondo Canyon levee	Eastern channel levee	RE	–	L	UMA
Palan (2017)	Rose Canyon	Canyon floor	RO	–	C	CS
Lonsdale and Hollister (1979)	Reynidsjup Channel levee	Fig. 2	RY	–	L	CS
ENI (unpub.)	South Afungi Canyon	Middle	SA	1	C	UMA
ENI (unpub.)	South Afungi Canyon	Middle	SA	2	C	CS
Normandeau et al. (2016)	Schmon Delta	Figs. 5, 6, 7, 8	SC	–	S	CS
Bárcenas et al. (2009), Urgeles et al. (2011)	Seco Prodelta	Table III and Table 1 in refs.	SE	–	C	UMA
Fonseca Ribeiro (2018)	Sao Francisco Canyon	Upper canyon floor i1	SF	1	C	UMA
Fonseca Ribeiro (2018)	Sao Francisco Canyon	Upper canyon floor i2	SF	2	C	UMA
Zhong (2025)	Shenxian Canyon levee	Right hand levee, Fig. 1E Table S2	SH	–	L	CS
Palma et al. (2021)	Sloggett Canyon	CB2 branch thalweg	SL	–	C	CS
Covault et al. (2014)	San Mateo Canyon	Figs. 6, 7B	SM	–	C	CS
Hughes Clarke (2016), Hage et al. (2018)	Squamish Prodelta	North channel TC C	SQ	–	C	CS
Stacey et al. (2019)	Squamish Prodelta	Lower slope, channel and lobe, St1	SQ	–	S	CS
Kidd et al. (1998)	Stromboli Canyon	Outer bend south of Lametini seamount	ST	–	C	UMA
Casalbore et al. (2014)	Stromboli Island	SE flank, Bf1	ST	1	F	CS
Casalbore et al. (2014)	Stromboli Island	NW flank, Bf2	ST	2	F	UMA
Casalbore et al. (2014)	Stromboli Island	N flank, Bf3	ST	3	F	CS
Arzola et al. (2008), Lastras et al. (2009), Masson et al. (2011a,b)	Setubal Canyon	Canyon floor, Fig. 14 Arzola	SU	–	C	UMA
Wynn et al. (2000b)	Selvagens Islands	Distal field NW of the islands	SV	1	S	UMA
Santos et al. (2019)	Selvagens Islands	NE proximal field, Fig. 5F profile	SV	2	S	UMA
Zhong et al. (2015)	Taiwan Canyon	South Taiwan Shoal upper	TA	U	C	CS
Zhong et al. (2015)	Taiwan Canyon	South Taiwan Shoal lower	TA	L	C	CS
Li et al. (2021)	Taiwan Canyon levee	Wave field 1, upper	TA	1	L	CS
Li et al. (2021)	Taiwan Canyon levee	Wave field 1, middle	TA	2	L	CS
Li et al. (2021)	Taiwan Canyon levee	Wave field 1, lower	TA	3	L	CS
Li et al. (2021)	Taiwan Canyon levee	Wave field 2	TA	4	L	CS
Kuang et al. (2014)	Taiwan Canyon levee	Western levee	TA	W	L	CS
Kuang et al. (2014)	Taiwan Canyon levee	Southern levee	TA	S	L	UMA
Trincardi and Normark (1988), Urgeles et al. (2011)	Tiber Prodelta	Line D, and Table 1 in refs.	TI	–	F	UMA
Hoffmann et al. (2008, 2011)	Torkoro Upper Slope	Hixon Bay, Group 2	TK	1	S	CS
Hoffmann et al. (2008, 2011)	Torkoro Lower Slope	Hixon Bay, Group 5	TK	2	S	CS
Clare et al. (2018)	Sulphur Bay, Tanna Island	Profile X, upper channel	TN	1	C	CS
Clare et al. (2018)	Sulphur Bay, Tanna Island	Profile X, upper middle	TN	2	C	CS
Clare et al. (2018)	Sulphur Bay, Tanna Island	Profile X, lower middle	TN	3	C	CS
Clare et al. (2018)	Sulphur Bay, Tanna Island	Profile X, lower	TN	4	C	CS
Casalbore et al. (2021)	Sulphur Bay, Tanna Island	Profile K, distal, Fig. 10	TN	5	S	CS
Clare et al. (2018)	Sulphur Bay East, Tanna Island	Profile Z, upper middle	TN	6	C	CS
Clare et al. (2018)	Sulphur Bay East, Tanna Island	Profile Z, lower middle	TN	7	C	CS

(*continued on next page*)

Table 2 (*continued*)

Source	Site	Description	Hub	Profile	Setting	Interpreted bedform type
Clare et al. (2018)	Sulphur Bay East, Tanna Island	Profile Z, lower	TN	8	C	CS
Clare et al. (2018)	Sulphur Bay East, Tanna Island	Profile Z, distal	TN	9	S	CS
Nakajima et al. (1998)	Toyama Canyon levee	Fig. 9 upslope	TO	1	L	CS
Nakajima et al. (1998)	Toyama Canyon levee	Fig. 9 downslope	TO	2	L	UMA
Nakajima and Satoh (2001)	Toyama Canyon levee	Line 202 upslope	TO	3	L	CS
Nakajima and Satoh (2001)	Toyama Canyon levee	Line 202 downslope	TO	4	L	UMA
Nakajima and Satoh (2001)	Toyama Canyon levee	Line 101 upslope	TO	5	L	CS
Nakajima and Satoh (2001)	Toyama Canyon levee	Line 101 downslope	TO	6	L	UMA
Total (unpub.)	Tungue Canyon	Middle	TU	1	C	CS
Total (unpub.)	Tungue Canyon	Middle	TU	2	C	CS
Malinverno et al. (1988)	Var Canyon, Fig. 7–8	Lower upper valley	VA	U	C	SD
Piper and Savoye (1993)	Var Canyon	Upper middle valley	VA	M	C	SD
Migeon et al. (2000, 2001)	Var Canyon levee/ridge	VSR very large	VA	1	L	CS
Migeon et al. (2000, 2001)	Var Canyon levee/ridge	VSR large	VA	2	L	CS
Migeon et al. (2000, 2001)	Var Canyon levee/ridge	VSR medium	VA	3	L	UMA
Migeon et al. (2000, 2001)	Var Canyon levee/ridge	VSR small	VA	4	L	UMA
Bárcenas et al. (2009), Urgeles et al. (2011)	Verde Prodelta	Table III and Table 1 in refs.	VE	–	S	UMA
ENI (unpub.)	Vamizi Canyon	Upper	VM	1	C	UMA
ENI (unpub.)	Vamizi Canyon	Middle	VM	2	C	CS
ENI (unpub.)	Vamizi Canyon	Middle	VM	3	C	CS
ENI (unpub.)	Vamizi Canyon	Distal	VM	4	C	CS
Casalbore et al. (2014)	Vulcano Island	SW flank, Bf5	VU	–	F	CS
Zhong et al. (2015)	West Penghu Canyon	Middle 1	WP	1	C	CS
Zhong et al. (2015)	West Penghu Canyon	Middle 2	WP	2	C	CS
Zhong et al. (2015)	West Penghu Canyon	Lower	WP	3	C	CS
Gong et al. (2012)	West Penghu Fan	Upper lower slope above Taiwan Canyon	WP	U	F	UMA
Gong et al. (2012)	West Penghu Fan	Lower lower slope above Taiwan Canyon	WP	L	F	CS
Zhong (2025)	Xishabe Canyon	SY78, Fig. 1B Table S1	XI	1	C	CS
Zhong (2025)	Xishabe Canyon	SY174	XI	2	C	CS
Zhong (2025)	Yongshi Canyon levee	Right hand levee, Fig. 1E Table S2	YO	–	L	CS
Migeon (2000)	Zaire Canyon levee	G2Z03	ZA	1	L	CS
Migeon (2000)	Zaire Canyon levee	Z2–19	ZA	2	L	CS
Migeon (2000)	Zaire Canyon levee	Z1–54	ZA	3	L	UMA
Leat et al. (2010, 2013)	Zavodovski Island	Eastern ridge, JR206_27	ZV	1	F	CS
Leat et al. (2010, 2013)	Zavodovski Island	Eastern ridge, JR206_29	ZV	2	F	CS

Table 3
Sites of fluvial field bedforms. For sources see section 1.2.

Site	Short code
American Canal	AC
Amazon	AM
Acop Canal	AP
Araguaia	AR
Atrisco Lateral	AT
Calamus	CA
Dry Fork Creek, Miss.	DF
Embarras	EM
Fraser	FR
Gravel Pit Runoff, Byhalia, Miss.	GP
Green	GR
Hii	HI
Jamuna	JA
Little Colorado, Cameron, AZ	LC
Mississippi	MI
Missouri	MO
Niobrara	NB
Nile	NI
North Loup	NL
Ob	OB
Parana	PA
Polomet	PO
Pigeon Roost Creek, Miss.	PR
Red Deer	RD
Rio Grande	RG
Rhine (Lower)	RH
Tanana	TA
Trinity	TR
Uruguay	UR
Virgin, St. George, Utah	VR
Zaire	ZA

different flow events; a bedform that is UMA for the formative flow, may be CS for later smaller flows. With these caveats in mind, we proceed to describe some bedforms that most certainly are CS.

Upslope migrating fine-sand bedforms on the Fraser Delta slope (Hill, 2012; Lintern et al., 2016; Hill and Lintern, 2022) short-coded FRS are upslope asymmetrical with intermediate steepness (Fig. 17) and have marked negative stoss slope (Fig. 18). The observed turbidity currents have rather thin basal layers relative to bedform size (Fig. 11) resulting in low wavenumbers (Fig. 12). These features point to CS on unconfined slopes (Fig. 21). Inside channels, however, bedforms are composed of medium sand, are smaller and symmetrical, and fall in an intermediate range where CS and UMA overlap in the phase diagrams (FRC).

Upslope migrating concave-downward bedforms on the northern channel of the steep Squamish Prodelta (Hughes Clarke, 2016; Hage et al., 2018) short-coded SQC are slightly downslope asymmetrical with high steepness (Fig. 17), gentle negative stoss slope (Fig. 18) and are composed of fine to medium sand (Stacey et al., 2019). Records of confined turbidity currents show relatively thin basal layers (Fig. 11) with associated low wavenumbers (Fig. 12, Fig. 16). They have all the markers of CS. Farther downslope in the lower slope bedforms are likely CS as well (SQS).

Upslope migrating concave-down bedforms on the main Pointe-des-Monts Canyon (Normandeau et al., 2014, 2019, 2022) short-coded PM are downslope asymmetrical and rather steep (Fig. 17) with very gentle negative stoss slopes (Fig. 18). No flow observations are available, but turbidity current basal thickness is indirectly estimated by erosion of the canyon wall (~1.5 m average, Fig. 11), which results in a low wavenumber (Fig. 16). These signatures indicate CS.

Upslope migrating very fine-grained, very large bedforms on the Monterey East Channel, on the levee off the Shepard Meander (Fildani et al., 2006) short-coded MOE are downslope asymmetric and

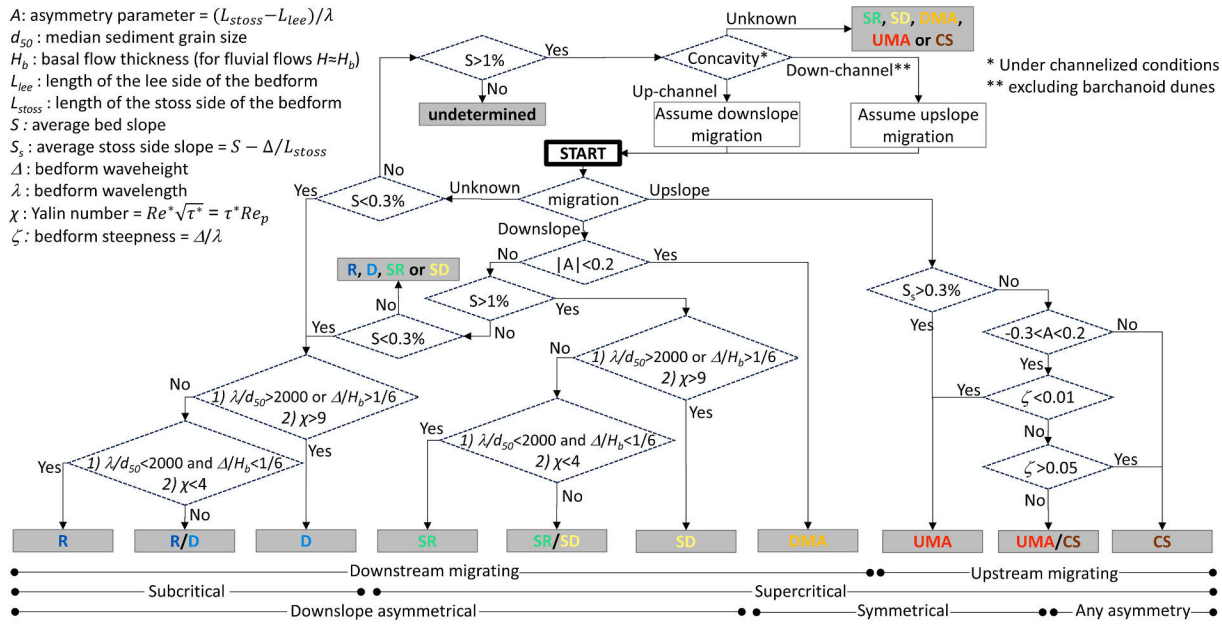

Fig. 20. Bedform interpretation criteria chart for when little or no flow data is known. Bedform dimensions, geometry and bed slope must be known. Some flow data and grain size may be needed to tell ripples from dunes. Still sometimes it is not possible to discern bedform type without knowing flow conditions. See section 6.2 for additional explanation. When migration direction is not known additional features such as bedform planar concavity may help identification provided the setting has some degree of confinement (section 7.14).

intermediate steep (Fig. 17) and have negative stoss slope (Fig. 18). No flow observations are available, but dedicated modeling point to low wavenumber (Fig. 16). These are among the largest CS ever observed (Fig. 10).

For other upstream migrating bedforms in different settings that can be classified as CS with a reasonable degree of certainty due to asymmetry and/or high steepness see Table 2, Fig. 10, Fig. 17.

In the CS-UMA overlapping area classification is more conjectural and based on additional parameters when available. We also note that UMA on the brink of transitioning to CS can develop large steepness well above their normal values, but still behave as UMA until the hydraulic jump is triggered, as recorded by Spinewine et al. (2010) whose observations of UMA evolving toward CS in Fig. 17 have steepness typically associated with CS.

These interpretations generally fit the view of Cartigny et al. (2011) that cyclic steps with downslope asymmetries are more likely found in confined, high energy settings (i.e. canyons), while upslope asymmetries are more representative for fine-grained bedforms in unconfined, low energy environments (i.e. slopes and levees). Detailed description of all field bedforms in Table 2 exceeds the scope of this study.

6.4. *Upstream migrating antidunes*

The Monterey Canyon is one of the field sites with flow, bedform and sediment observations allowing an evaluation not unlike those under controlled laboratory conditions. Our assessment leans to the theory that bedforms in Monterey Canyon (Paull et al., 2010, 2011) at the locations where turbidity currents were recorded (~800–1500 water depth, Xu et al., 2004, 2014) are upstream migrating antidunes driven by strong sediment-gravity flows, as conjectured by Smith et al. (2007). In the Kennedy diagram the Monterey Canyon data points fall in the UMA region, close to the transition where supercritical bedforms migrate downstream and – at least for turbidity currents such as those in Xu et al. (2004, 2014) with wavenumber k_b too high to be CS (Fig. 12). Their asymmetry is within (MO3 at water depth ~ 1450 m) or slightly above (MO2 at w.d. ~ 1000 m, Fig. 22) that of most other UMA (Fig. 16), and this downslope asymmetry can be interpreted as more characteristic of CS, that could occur in the waning stage of the turbidity current (see section 7.9). Their steepness is on the high side of most UMA, overlapping with DMA and CS (Fig. 17). It is unlikely that MO3 bedforms are CS, as some stoss slopes are positive and beyond the point where subcritical flows can occur, but this possibility cannot be ruled out for MO2 bedforms (Fig. 18). The Monterey Canyon bedforms occur on areas where the canyon fill consists of cohesionless coarse sand and gravel (Paull et al., 2011). In the Froude number and Shields number diagrams these bedforms fall in a region where fluvial coarse-grained UMA and DMA are common (Fig. 14, Fig. 15). However, the facies of the sediments collected from these bedforms are composed of fining-upward sequences (Paull et al., 2010), which differ from the upward coarsening experimental UMA.

Another feature that hints at upstream migration is the concavity of the bedforms in a confined setting in tandem with supercritical flow conditions. In Monterey Canyon the crescent-shaped bedforms have concave down-canyon crests (Fig. 22), similar to experimental UMA in Fig. 7a. Concave up-canyon bedforms also occur in Monterey Canyon, but not at the locations assessed here (ca 1000–1500 m). Areas of up-concavity are upstream of features that may be restricting down-canyon sediment movement (Paull et al., 2011), in deeper waters (>1800 m) and seem to be modulated also by internal tides (Wolfson-Schwehr et al., 2023).

Turbidity currents and associated bedforms have also been observed in Bute Inlet (BU), British Columbia (Zeng et al., 1991; Heijnen et al., 2020; Chen et al., 2021). These bedforms are confined within channels with concave-down crescent shapes. They are superimposed over larger upstream migrating features, called knickpoints, which modulate bedform size and location by changes in bed slope. While the regional bed slope in Bute Inlet mid-reach is in the order of 1.2 %, locally downstream of the knickpoints slopes can be up to 5 %. The Bute Inlet crescentic bedforms are likely UMA created by supercritical turbidity currents. Froude number estimations based on observations by Zeng et al. (1991) set the bedforms in the UMA region of the Kennedy diagram (Fig. 12). While individual bedforms may be either upslope or downslope asymmetrical, on average they tend to be rather symmetrical (Fig. 16) and with intermediate steepness (Fig. 17). In the Froude number diagram (Fig. 14), Bute Inlet bedforms sit in a region where fluvial medium-grained sand UMA are also found.

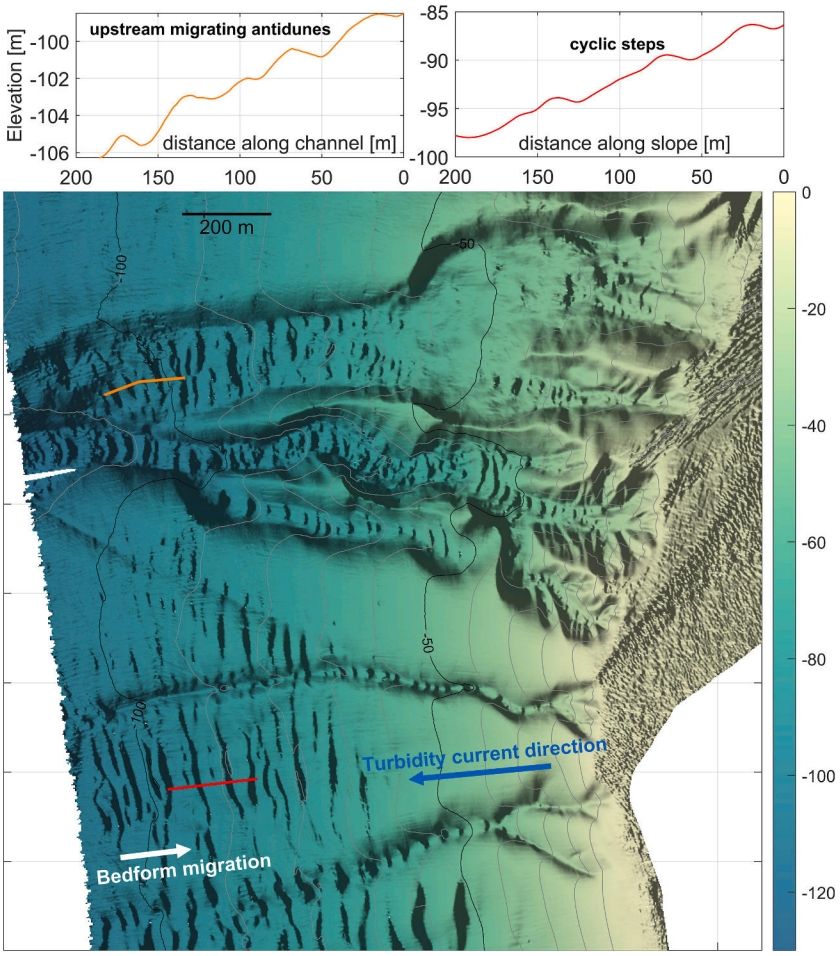

Fig. 21. Fraser Delta upstream migrating bedforms. Color indicates water depth. Contour lines spacing every 10 m. Hillshade highlights stoss and lee sides. Insets show cross sections within the channel (FRC) and on the slope (FRS). The bedforms in the channel are interpreted to be upstream migrating antidunes, and those on the slope cyclic steps. See section 6.3 for further details. Bathymetry data courtesy P. Hill and R. Kung.

Bedforms in the Malaylay Canyon in The Philippines migrate upslope, as revealed by repeat bathymetry surveys and sub-bottom profiles, driven by short-lived but intense turbidity currents (Sequeiros et al., 2019) which result in at least half a wavelength λ migration in about 30 min. Upslope migration is also inferred from their planimetric curved concave-down crests (Fig. 23), the rate of migration being faster in the thalweg than in the margins. The middle and lower reaches of the Malaylay Canyon floor (MY1–3) have coarse-grained sediment (sand and gravel). Sediment is coarser within the channels (d_{50} ~ 200–500 μm) and finer on the overbank and inter-channel areas (d_{50} ~ 15–80 μm). Based on their dimensions, grain size, and estimated bankfull flow conditions the bedforms are most likely UMA. These same bedforms, however, may also be classified as CS during the waning stage of turbidity currents.

For other upstream-migrating bedforms that can be confidently classified as UMA based on symmetry, low steepness, and/or positive stoss slope, refer to Table 2, Fig. 17, Fig. 18.

6.5. *Downstream migrating antidunes*

Bedforms in the lower Kaikoura Canyon (KA) off the east coast of New Zealand have concave-up crests and migrate downslope (Fig. 24), revealed by repeat bathymetry surveys, driven by powerful earthquake-triggered "canyon flushing" turbidity currents (Mountjoy et al., 2018). The bed material is coarse and vertically-graded, from pebble gravel below to coarse sand turbidite with mud above, as interpreted from a core taken at 1874 m water depth in the lower Kaikoura Canyon (Lewis and Barnes, 1999). The regional slope close to 1 % indicates that the turbidity currents were likely supercritical flow regime. The bedforms are rather symmetrical (or mildly downslope asymmetrical) and with relatively high steepness. All these features together point to DMA.

6.6. *Supercritical-regime dunes*

Bedforms in the upper Laurentian Eastern Valley between 2000 and 3500 m water depth are coarse gravel waves with mean grain size estimated in the range 10–100 mm (Piper et al., 1985, 1988; Hughes Clarke et al., 1990). The average bedform wavelength increases from 30 m at the 2000-m isobath to 70 m by 3500 m, and average waveheight ranges from 4 m to 7 m. They are markedly downslope asymmetrical with shorter lee faces that dip downslope at 25–45° (Fig. 25), with rather steep Δ/λ ratios (Fig. 17), straight to mildly sinuous elongate crests. The average regional slope S is steeper than 2 %, hence these bedforms most likely developed under supercritical flow, and given their asymmetry can be classified as SD (LA1–2). Boulders are observed on the stoss side and are densest close to trough, but are rarely visible on the lee face of the gravel waves, which is consistent with a downslope-migrating, asymmetric bedform (Fig. 9).

The bedforms in the lower Var Canyon (or upper Var Valley, VAU) at about 2000 m depth (Malinverno et al., 1988) are composed of coarse material (coarse sand and larger), and with wavelengths between 50 and 100 m and waveheights estimated at less than 5 m with intermediate steepness. They are downslope asymmetric and have slightly concave up crests which points to downstream migration. The average regional

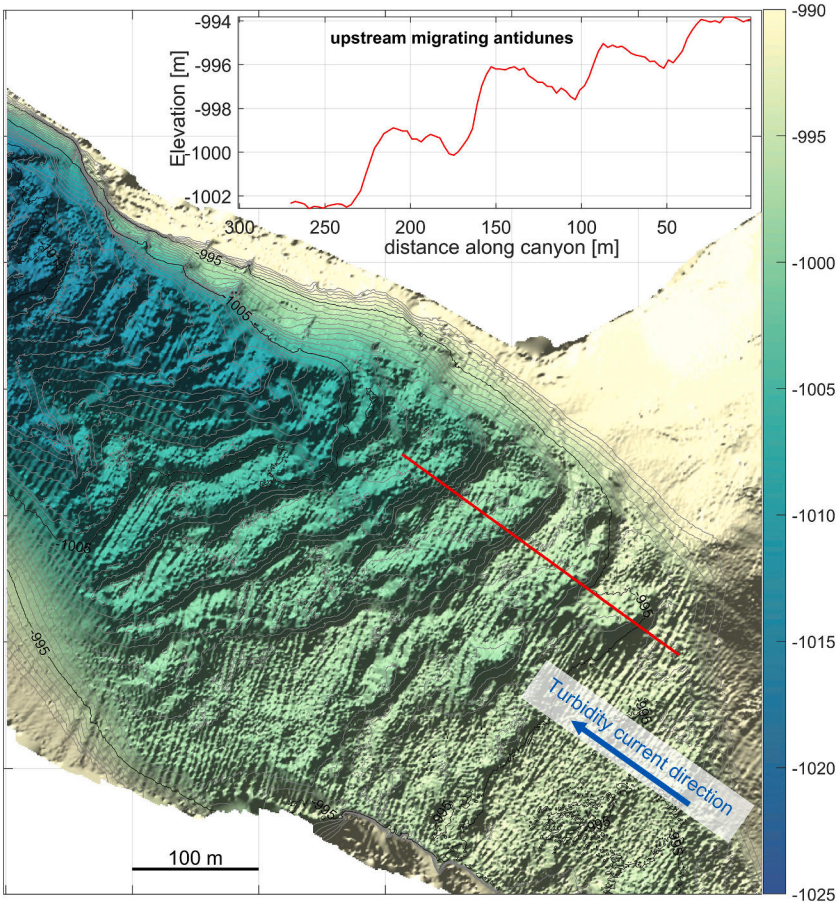

Fig. 22. Monterey Canyon bedforms at ~1000 m water depth (MO2). Color indicates water depth. Contour lines spacing every 1 m. Hillshade highlights stoss and lee sides. Inset shows the cross section along the red line. These bedforms are interpreted to be upstream migrating antidunes. See section 6.4 for further details. Bathymetry data courtesy E. Lundsten and C. Paull. (For interpretation of the references to color in this figure legend, the reader is referred to the web version of this article.)

slope S is 2.5 %, related to supercritical flow regime (Fig. 13b). All these characteristics indicate SD.

6.7. Dunes

Bedforms in the distal thalweg of South branch of the lower Laurentian Eastern Valley in ~4900 m water depth are large waves with a mean wavelength of 300 m and waveheight of ~5 m (Piper et al., 1988; Hughes Clarke et al., 1990). They are also composed of relatively coarse material (coarse sand to gravel 3–6 mm in grain size) but finer than their upslope counterparts discussed in section 6.6.

Another difference is that in the termination of the South branch slopes are much gentler $S \sim 0.26$ %, where only subcritical flows are observed (Fig. 13b), hence it is inferred that only downstream migration is possible. Given their size, then, these bedforms can be classified as subcritical-regime dunes (LA3–4).

The thick massive turbidites suggest deposition beneath a decelerating flow. Within the South branch, thalweg bedforms are aligned in lanes and straight crested, but farther downslope they become sinuous and with spreading crest orientations indicating a diverging flow in an increasingly unconfined setting.

Due to the extreme deep-water, it is difficult to accurately estimate bedform asymmetry from the available sidescan data, but they seem to be slightly downslope asymmetric (Fig. 25).

7. Discussion

7.1. Terminology: bedforms, sediment waves, gravel-, sand-, and mudwaves

The most common bedform observed on the seafloor is known as "sediment wave". Wynn and Stow (2002) defined a sediment wave as "a large-scale […] undulating, depositional bedform that is generated beneath a current flowing at, or close to, the seafloor". The formative current can be either a turbidity current or a bottom contour current, and the wave material is dominated by fine (mud and silt) or coarse (sand and gravel) material.

Fine-grained turbidity current sediment waves are found on channel levees, the continental slope and rise, and the flanks of volcanic islands. They are associated with unconfined turbidity currents and may have either straight or sinuous crests (in the rare cases occurring in confined settings, they may have crescentic shaped crests). In most cases they show upslope migration and a downslope decrease in dimensions and asymmetry. Individual beds are thicker and coarse-grained on the stoss side. They are the largest observed bedforms, with maximum order of magnitude is $\lambda \sim 10$ km, $\Delta \sim 100$ m (Wynn and Stow, 2002; Symons et al., 2016).

Coarse-grained turbidity current sediment waves are found in canyons, channels and channel-lobe transition zones. They are associated with confined or expanding turbidity currents. They are smaller (maximum order of magnitude is $\lambda \sim 1$ km, $\Delta \sim 10$ m) than fine-grained waves. They may lack internal structure and may be sometimes short-

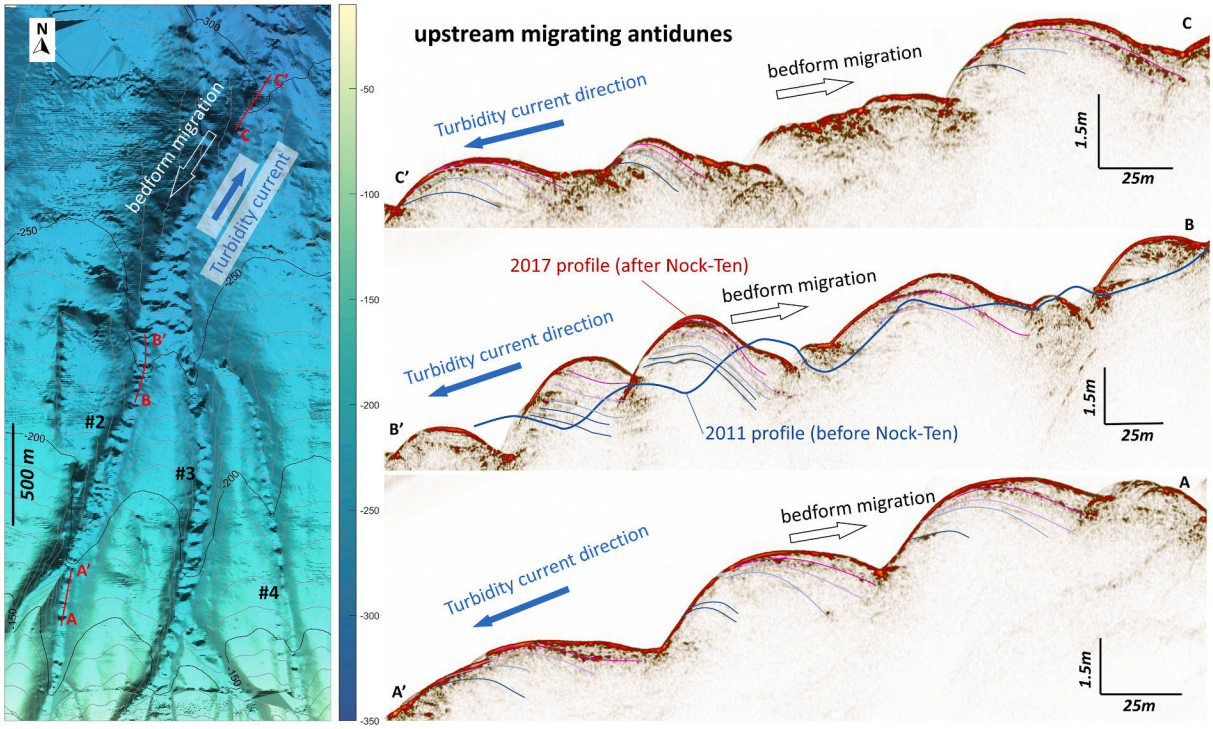

Fig. 23. Malaylay Canyon upstream migrating bedforms. Left: Hillshade relief highlighting stoss and lee sides. Color indicates water depth. Contour lines spacing every 10 m. Right: interpreted sub-bottom profiles at three locations along Malaylay Canyon channel #2 (MY1, MY2, MY3) that reveal upstream bedform migration and bathymetric changes before and after turbidity current triggered by typhoon Nock-ten in December 2016. Internal structure shows strata on the stoss side progressively forming upstream, and an erosional surface forming a steep lee side. Under bankfull conditions these bedforms are interpreted to be upstream migrating antidunes. See section 6.4 for further details.

lived. They may migrate up- or downslope and tend to have crescentic crests, either down- or upslope shaped depending on migration direction (see section 7.14). There appears to be a relationship between wave dimensions and flow velocity (Wynn and Stow, 2002; Symons et al., 2016).

Unconfined bedforms are more prone to aggrade and form a positive relief in contrast to small-scale, confined bedforms, where erosion is thought to play a larger role (Symons et al., 2016).

For Symons et al. (2016) the term "bedform" encompasses seafloor features of any scale with either negative or positive relief in relation to the overall seafloor. The former are called scours (erosion dominated) and the later sediment waves. This distinction may be nominal only because the processes that form scours can be the same as those that form other bedform types, and there is also a lack of data for quantification. In any case, sediment waves are created by a combination of deposition and erosion, and their crests are positive relative to the surrounding region of seafloor, whether fully depositional or mixed. The term sediment wave then does not carry any grain size constraint.

Based on the upslope migration of sediment waves and the comparable symmetrical geometry, Normark et al. (1980) interpreted some sediment waves as upstream-migrating antidunes. Fildani et al. (2006) and Lamb et al. (2008) provided evidence that some sediment waves observed in the submarine environment may be cyclic steps. Cartigny et al. (2011) introduced criteria to tell which sediment waves can be classified as cyclic steps based on the likelihood they were formed under transcritical flow.

The term "mudwave" has also been also used to describe sinusoidal sediment topography. This term is commonly though not exclusively associated with contour currents (Flood, 1988). These are large bedforms ($\lambda > 1$ km, Δ up to 100 m), composed mostly of fine-grained sediment (clay and silt) and are often observed to migrate against the prevalent bottom-current direction, but can also migrate down-current or only aggrade vertically.

Our terminology relies on a generic non-specific term to start the process of classification, namely "bedform". This is subsequently modified according to specific characteristics of the bedform and, when available, according to those of the flow. Informed by the densimetric Froude number, the terminology can be traced to, and is compatible with, fluvial flow bedforms. We supplement it with novel terminology when there is no clear equivalent in fluvial flows, such as supercritical dunes (see section 7.8). Our terminology provides a comprehensive view of all transverse bedforms created by down-slope density currents.

7.2. *Fluvial and submarine bedforms biases*

Rivers, saline currents, and turbidity currents have common features but also some fundamental differences. Rivers and saline currents flow with or without sediment load; while turbidity currents are driven by, and depend on, suspended sediment to move. The density of river water is three orders of magnitude greater than that of air. In contrast, the excess density of saline or turbidity currents is typically one or two orders of magnitude lower than the density of the ambient fluid (Parker, 2005; Cartigny and Postma, 2016). The average F_{eb} in our data is 0.044, with a standard deviation of 0.019 and a maximum of 0.164.

There is a bias toward subcritical bedforms in our river datasets, also found in data gathered by Czapiga et al. (2019). This is because most large rivers run on gentle slopes and in subcritical regime, and also because there are relatively few data points from steep mountain rivers, which are more diffult to monitor when in flood.

On the other hand, there is a bias toward upstream-migrating supercritical bedforms in field turbidity currents, as pointed out by Symons et al. (2016). This is in part because most of our field data comes from steep continental slopes, canyons and deltas, and little data are available farther downslope on the continental rise and abysal plain where gentler slopes and subcritical flows prevail. It can also be inferred that bedforms on the continental rise and beyond are created less frequently, as

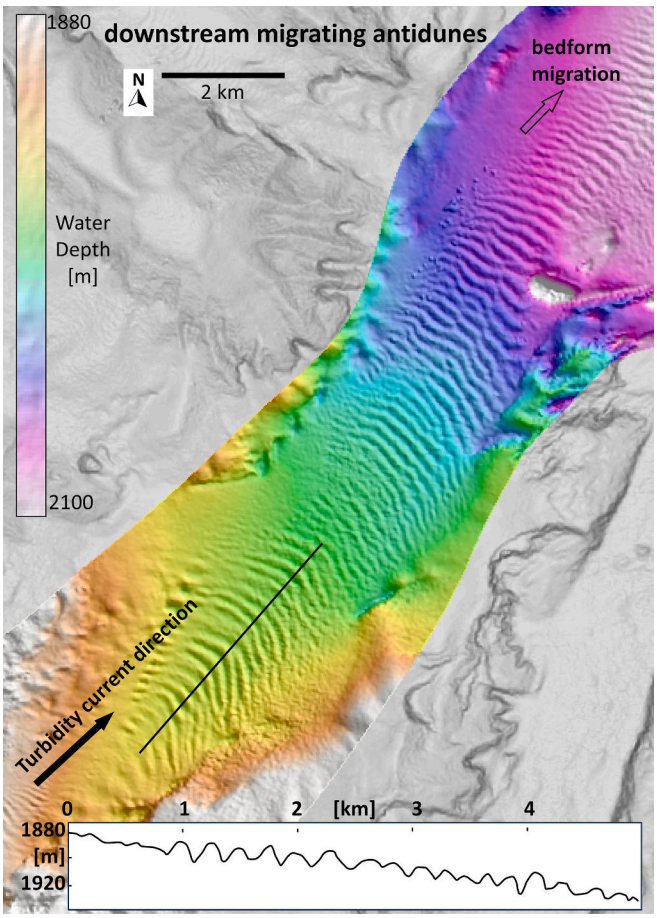

Fig. 24. Kaikoura Canyon bedforms (KA). Morphology of the lower canyon downstream migrating gravel waves, interpreted to be downstream migrating antidunes. Color indicates water depth. Inset shows a piece of the longitudinal profile to illustrate bedform dimensions. See section 6.5 for further details. Adapted from Fig. 3 in Mountjoy et al. (2018).

turbidity currents may reach these areas less often and may be weaker than those on continental slopes and in canyons. This may be a mirror of the intermittency observed in steep rivers where large bedform-creating floods are sporadic. However there is evidence of subcritical regime bedforms created by turbidity currents in submarine environments such as those in the South branch termination of the Laurentian Eastern Valley.

There are other bedforms farther down on the rise and abyssal plain, though contour currents may be often involved in shaping them. Contour currents, relatively weak but persistent geostrophic currents flowing along-slope, can rework turbidity current deposits and create bedforms themselves (Fox et al., 1968; Flood et al., 1993; von Lom-Keil et al., 2002; Rebesco et al., 2014; Hernández-Molina et al., 2018; Miramontes et al., 2020; Warnke et al., 2023; Principi et al., 2024). An example of bedforms shaped by the combined influence of turbidity and contour currents can be found in the sediment wave field 2, located on the right flank of the lower Taiwan Canyon (Gong et al., 2012).

It has been suggested that density currents are more prone to supercritical flow than rivers, due to the relatively small density contrast between the current and ambient seawater compared to that between water and air (Cartigny et al., 2011; Fedele et al., 2016; Talling et al., 2023). This reduced gravity effect is manifested through a low fractional excess density in the densimetric Froude number (Eq. 2 and 4) which favors supercritical flow conditions even under relatively low flow velocities, certainly lower than otherwise needed in fluvial flows. This may partially explain the abundance of supercritical ripples and dunes in density and turbidity currents compared to their scarcity in fluvial flows, at least within the available datasets (e.g., Fig. 12).

In fluvial flows, water density remains nearly constant and plays little role in bedform development, even with high suspended loads -except in hyperconcentrated flows, which are beyond the scope of this study. However, the excess density in the reduced gravity of density currents is a variable and it is directly connected to flow speed rather than flow thickness. This is an additional factor that favors the formation of low-steepness, upstream migrating bedforms such as UMA, that can later evolve into CS, both common in submarine environments (see sections 7.4, 7.13).

7.3. Total or basal Froude number?

We have considered only the basal (lower) layer of the density current when assessing the connection between flow and bedforms. The premise for this split might seem questionable because the upper layer also plays a role in shaping the density current flow, especially in the supercritical regime. However, by considering the basal layer alone, the part of the flow profile that is responsible for creating the bedforms is isolated (Ohata et al., 2023). The basal layer profile closely mimics fluvial flow profiles, and thus a good match is found when density current and river data are plotted together, e.g., the Kennedy phase diagram (Fig. 12), using the basal flow properties of density currents. Were the Froude and wave numbers to be computed based on the characteristics of the entire flow profile there would be no agreement in the Kennedy diagram between fluvial and density current bedforms.

We find that the basal Froude number Fr_{db} is higher than the total Fr_d in the supercritical regime, whereas the two are very similar in the subcritical regime based on available datapoints (Fig. 13a). A flow that is on average faster and thinner and moves under a denser ambient fluid tends to have a higher Froude number, conversely a denser flow has a lower one. According to available data it is the former effect that prevails, but the opposite may be true for turbidity currents moving on very gentle slopes for which we do not have data. While limited, these observations point to the transition from subcritical to supercritical regime occurring at an intermediate range of bed slopes around 1 %, where fluvial and turbidity current Fr_d collapse. And that, unlike fluvial flows, turbidity currents Fr_d diverges from Fr_{db} and tends to asymptotic for very gentle and very steep slopes (Sequeiros, 2012).

Estimating the basal Froude number Fr_{db}, requires accurate information of the entire vertical profiles, and there may be uncertainty as to what constitutes the ambient fluid in the computation of the basal layer-averaged fractional excess density F_{eb}. In our calculations, and for the sake of simplicity, we have considered it with respect to the ambient fluid ρ_a rather than the density of the upper layer. This may help explain the transgression of some DMA datapoints into the UMA space in the Kennedy phase diagram (Fig. 12), in addition to effects of suspended sediment, stratification (Ohata et al., 2023), and instrumentation and measurement bias.

Note that some authors, e.g., Symons et al. (2016) use the term “basal layer” for a thin, coarse, high-concentration near-bed layer. This is not necessarily the same as the basal layer defined in this study which extends up to the height above the bed where the peak velocity is found (see Fig. 1 and section 7.4).

7.4. Flow control

Provided bed slope and grain size remain the same, faster and thicker flows create larger bedforms. This is observed in flume as well as field data, and is shown in Fig. 26 where the flow strength is quantified by the basal specific discharge $q_b = U_b H_b$.

Laboratory density currents reveal additional details. Unlike rivers, larger flow strength in density currents can be attained in different ways. Larger discharge q_b increases basal current velocity U_b and thickness H_b. Excess density F_{eb}, on the other hand, increases U_b, but not much H_b. This

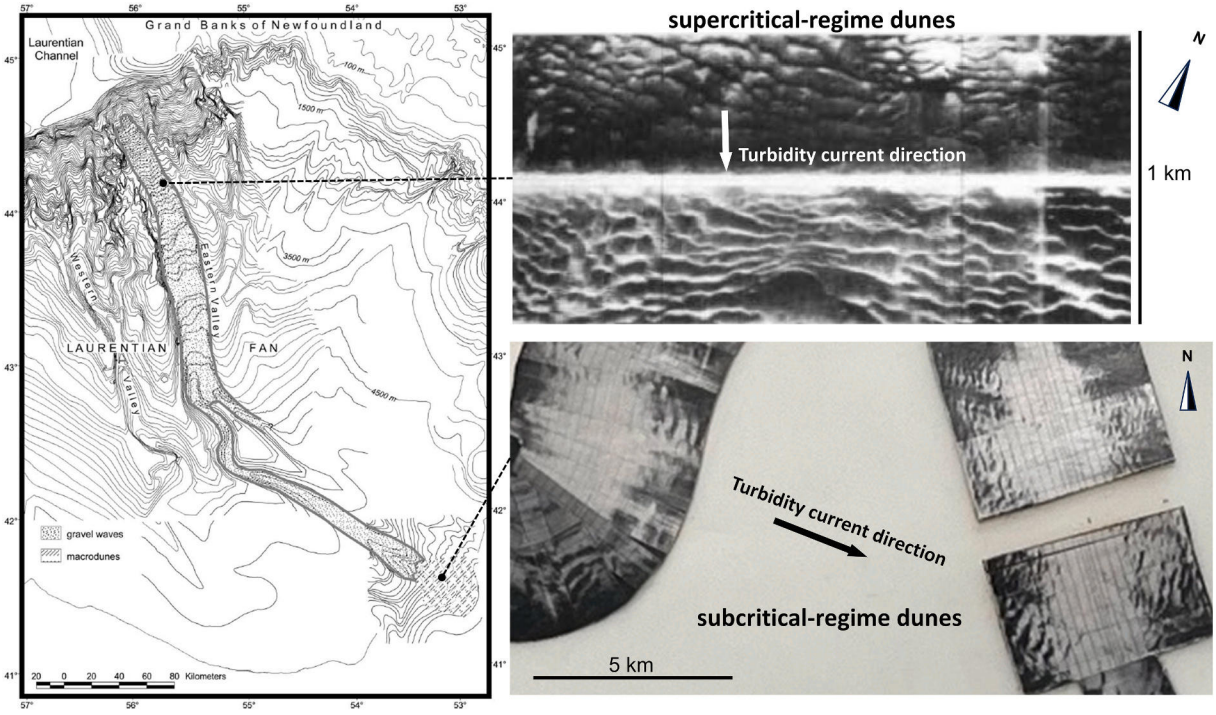

Fig. 25. Laurentian Eastern Valley bedforms. Left: bathymetry of the Laurentian Fan and Valleys adapted from Wynn and Stow (2002) and Hughes Clarke et al. (1990). Top right: sidescan sonogram at 2500 m water depth with gravel waves (LA1, LA2) interpreted as supercritical dunes at the eastern margin of the Eastern Valley, adapted from Fig. 5 in Piper et al. (1985). Bottom right: sand bedforms (LA4) interpreted to be dunes at the termination of the Eastern Valley South branch at 4900 m water depth as seen in a mosaic sidescan, courtesy of John Hughes Clarke. See sections 6.6 and 6.7 for further details.

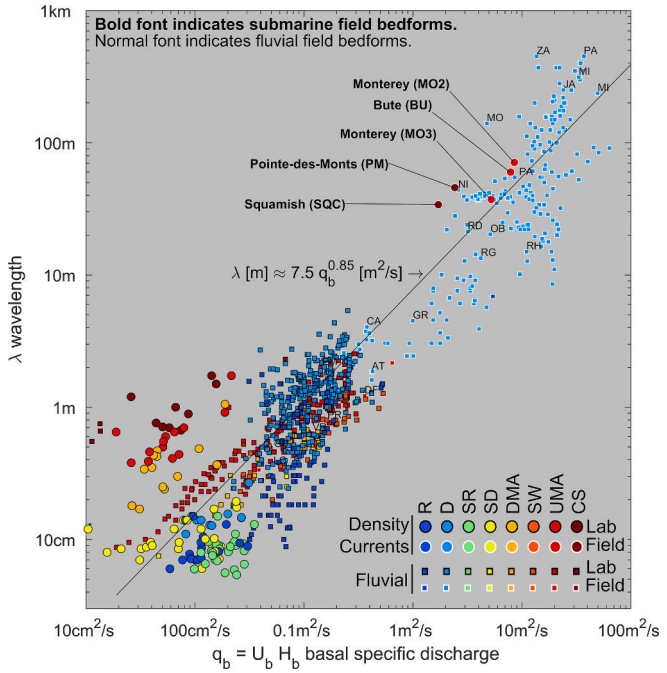

Fig. 26. Basal specific discharge vs bedform wavelength. Faster and thicker flows create larger bedforms. Spread is caused by other factors such as grain size, bed slope and bedform type. The scarce submarine flow observations agree with data from large fluvial rivers. Bold font code indicates submarine field bedform hub and profile (Table 2 and Fig. 19). Normal font indicates fluvial bedforms (Table 3).

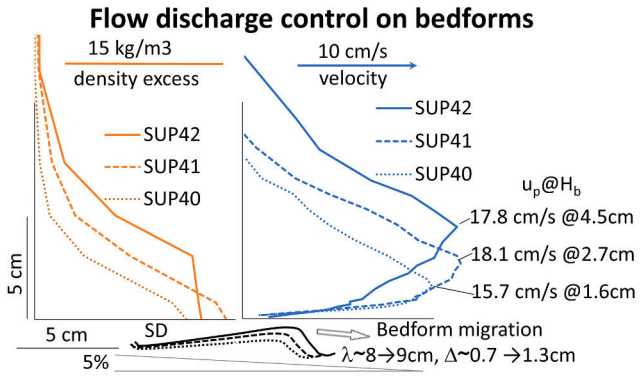

ID	Boundary		Conditions at observation section						
	total				basal				
	q	$\bar{\rho}$	q	$\bar{\rho}$	q_b	$\bar{\rho}_b$	Fr_{db}	k_b	τ^*
-	cm²/s	kg/m³	cm²/s	kg/m³	cm²/s	kg/m³	-	-	-
SUP42	67.0	24.3	119.1	8.8	57.5	13.3	1.65	3.25	0.38
SUP41	44.0	24.3	89.8	8.6	36.0	13.4	2.20	2.03	0.35
SUP40	22.0	24.3	64.4	6.4	17.0	11.5	2.52	1.26	0.26

Fig. 27. Flow discharge control on bedform, and feedback from bedform to flow. Three instances of supercritical dunes created under increasing flow strength with the same bed material (P2), bed slope (5 %) and boundary density (Sequeiros et al., 2010a). Larger flows induce larger bedforms, but bedforms also affect the density current. Data in table correspond to single profiles, not to spatially averaged profiles.

has consequences on how a bedform may form, evolve and transition to a different type of bedform (section 7.13).

There is feedback from bedform to flow as well. Bedform macro roughness increases friction and enhances turbulent mixing in the basal layer, especially for those with flow separation on the lee side, resulting in larger H_b and lower near- bed density ρ_b. Fig. 27 shows three super-critical dune fields created by density currents of increasing flow

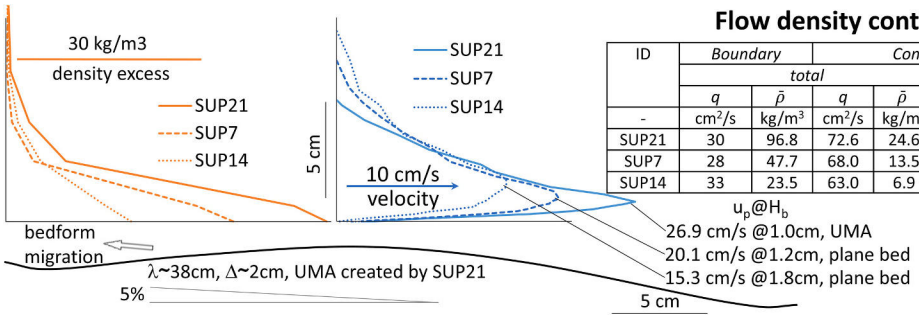

Flow density control on bedforms

ID	Boundary		Conditions at observation section						
	total				basal				
	q	$\tilde{\rho}$	q	$\tilde{\rho}$	q_b	$\tilde{\rho}_b$	Fr_{db}	k_b	τ^*
-	cm²/s	kg/m³	cm²/s	kg/m³	cm²/s	kg/m³	-	-	-
SUP21	30	96.8	72.6	24.6	18.8	45.7	2.79	0.17	0.12
SUP7	28	47.7	68.0	13.5	17.1	31.0	2.48	-	0.07
SUP14	33	23.5	63.0	6.9	19.1	14.8	2.13	-	0.05

Fig. 28. Flow density control on bedform. Three supercritical currents over the same bed material (P3), bed slope (5 %) and similar discharge (Sequeiros et al., 2010a). The lighter currents induce no bedform. The denser current SUP21 forms upstream migrating antidunes (UMA). Other parameters being the same, larger excess densities increase flow velocity and shear stress but not thickness. They also increase Froude number. Data in table correspond to single profiles, not to spatially averaged profiles.

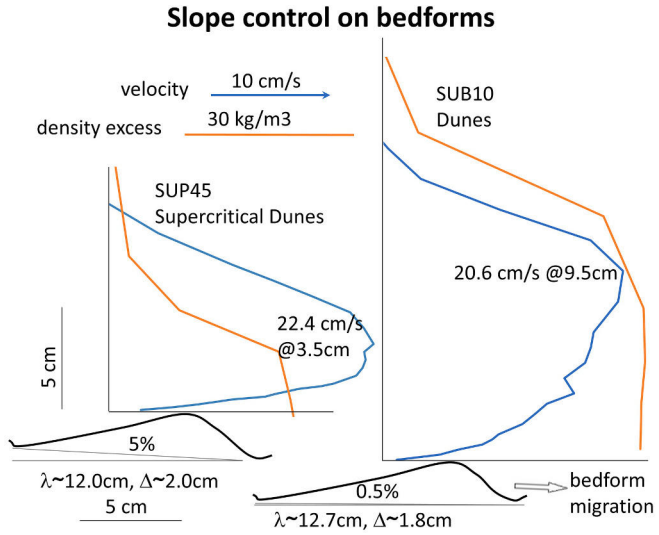

ID	Bed slope	Boundary		Conditions at observation section					
		total				basal			
		q	$\tilde{\rho}$	q	$\tilde{\rho}$	q_b	$\tilde{\rho}_b$	Fr_{db}	k_b
-	%	cm²/s	kg/m³	cm²/s	kg/m³	cm²/s	kg/m³	-	-
SUP45	5.0	67.0	47.0	138.0	19.8	55.7	30.5	1.60	1.81
SUB10	0.5	156.0	69.6	208.1	42.3	145.5	44.6	0.76	4.71

Fig. 29. Slope control on flow and bedform. Supercritical density current and associated supercritical dunes on 5 % bed slope (left), and subcritical current and associated dunes on 0.5 % slope (right) from Sequeiros et al. (2010a). Both bedforms have same bed material (P2) and similar dimensions, but the subcritical current has much higher basal specific discharge and density than the supercritical flow. The subcritical dune is slightly more downslope asymmetric than the supercritical dune. Data in table correspond to single profiles, not to spatially averaged profiles.

strength, but with the same bed material, bed slope and density boundary condition. The bedforms created by the weakest current could alternatively be classified as supercritical ripples. While there is an increase in velocity, thickness and density as the current gets larger, the largest current has a similar peak velocity u_p to the intermediate current, and a more well mixed (less stratified) basal layer. As bedforms grow, the flow density profile may develop an inflexion point which is usually not observable in supercritical flows with flat bed or ripples. Another net result of the bedform feedback is to make supercritical flows less supercritical by increasing the denominator and reducing the numerator in the Froude number (Eq. 4).

The distinct role of excess density is seen in Fig. 28. Three supercritical currents develop over the same bed material and slope with similar specific discharge. The lighter currents induce no bedform and the bed remains plane. The denser current forms UMA. Unlike the effects of specific discharge, larger excess densities increase flow velocity, shear stress and Froude number, but not thickness. In fact, the basal layer becomes thinner. Had specific discharge been increased while keeping the excess density the same, then DMA would probably have developed (see section 7.11).

While specific discharge q_b will increase if turbidity currents self-accelerate as both flow velocity U_b and thickness H_b grow; thickness of by-passing or depositional flows will also grow downstream because of water entrainment from the ambient fluid into the upper and eventually basal layer. Symons et al. (2016) argue that the more stratified the flow is with the development of a dense and coarse near bed layer, the more likely that bedforms will be shorter. On the other hand, the more dilute and well-mixed the flow is, the more likely the bedforms will be longer. Yet, the matter is not only flow capacity to transport high concentrations, and flow competence to move coarse grain sizes, but also grain size availability and flow regime. Hence, turbidity currents overflowing canyon levees will necessarily be more diluted and composed of finer material than currents remaining in canyons. Conversely supercritical turbidity currents are overall more stratified than subcritical ones, and the latter tend to have a relatively uniform and well mixed (i.e. less stratified) basal (lower) layer (Sequeiros et al., 2010a). These processes, and their effects on bedform dimensions, are in great part controlled by bed slope.

7.5. Slope control

Average or regional bed slope controls to a large degree the Froude number regime and consequently shapes velocity and density vertical profiles by means of the ambient fluid entrainment, resulting in distinct profiles for subcritical and supercritical regime (Sequeiros, 2012).

Supercritical flows are overall more efficient at moving coarse bedload than subcritical flows and they can induce bedforms with dimensions similar to those formed by subcritical flows with lower flow discharges and densities. Fig. 29 shows two density currents, one supercritical and another subcritical, flowing over the same bed material. Both currents create similar size bedforms, but are very different in terms of specific flow discharge, density, and shape of vertical velocity and density profiles. The main reason is that the supercritical density current moves on a steep bed slope $S \sim 5$ %, while the subcritical current moves on a slope an order of magnitude less steep $S \sim 0.5$ %.

Based on our observations, we can practically rule out subcritical flows on slopes steeper than ~1.0 % and supercritical flows on slopes gentler than ~0.3 % (Fig. 13b). There are some observations of flows with Froude number below unity and $S > 1$ %, but they pertain to data points in the Kennedy diagram within or around the upstream migrating wedge intruding into downstream migrating zones, where flows tend to be unstable and dificult to measure (Fig. 12). McCave (2017) also found that a condition for the existence of antidunes under supercritical

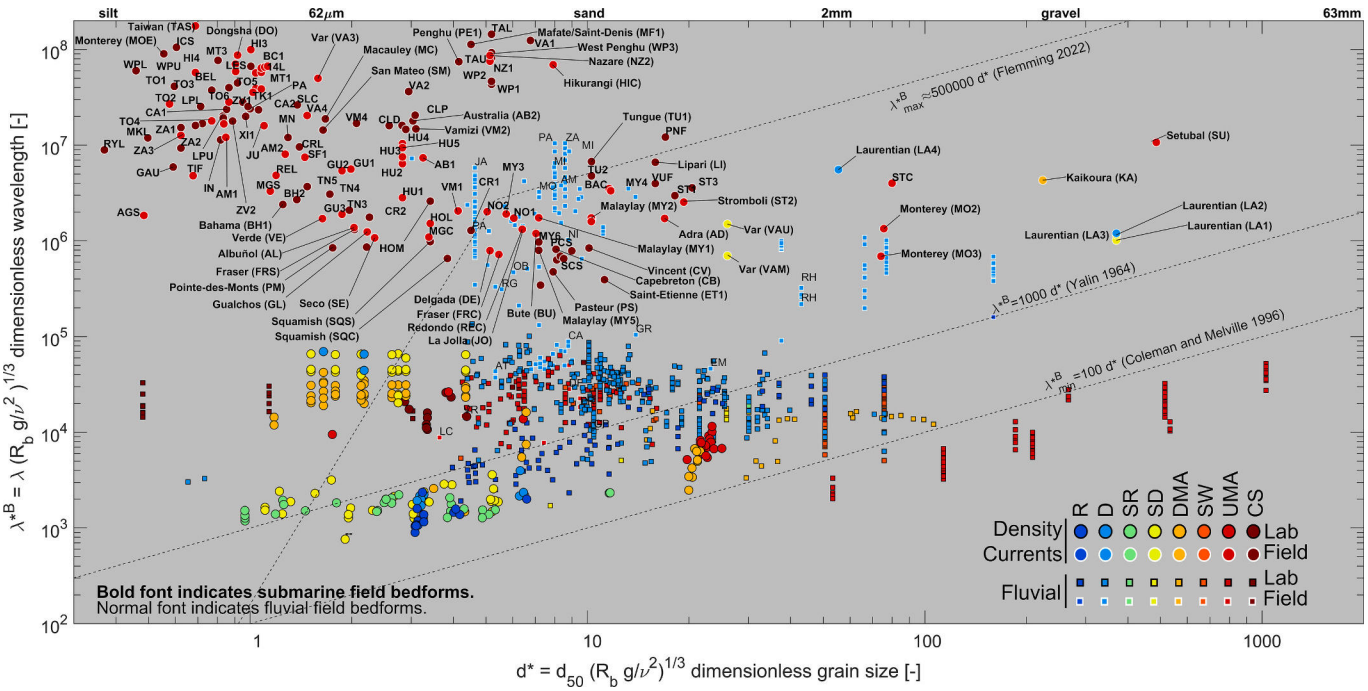

Fig. 30. Dimensionless bedform wavelength vs dimensionless grain size. Yalin (1964), Coleman and Melville (1996), and Flemming (2022) equations are derived mostly for fluvial ripples and dunes. They indicate that larger grain sizes are associated with larger bedforms. Field CS and UMA in mostly unconfined settings are outliers for they are the largest bedforms with the finest grain size without a clear trend. Bold font code indicates submarine field bedform hub and profile (Table 2 and Fig. 19). Normal font indicates fluvial bedforms (Table 3).

ID	Boundary		Conditions at observation section					
	total		total		basal			
	q	$\bar{\rho}$	q	$\bar{\rho}$	q_b	$\bar{\rho}_b$	Fr_{db}	k_b
-	cm²/s	kg/m³	cm²/s	kg/m³	cm²/s	kg/m³	-	-
SUP33	111.0	48.9	185.3	20.0	89.7	31.7	2.17	0.34
SUP13	111.0	47.4	193.5	24.4	90.8	34.4	2.39	0.74
SUP45	67.0	47.0	138.0	19.8	55.7	30.5	1.60	1.81

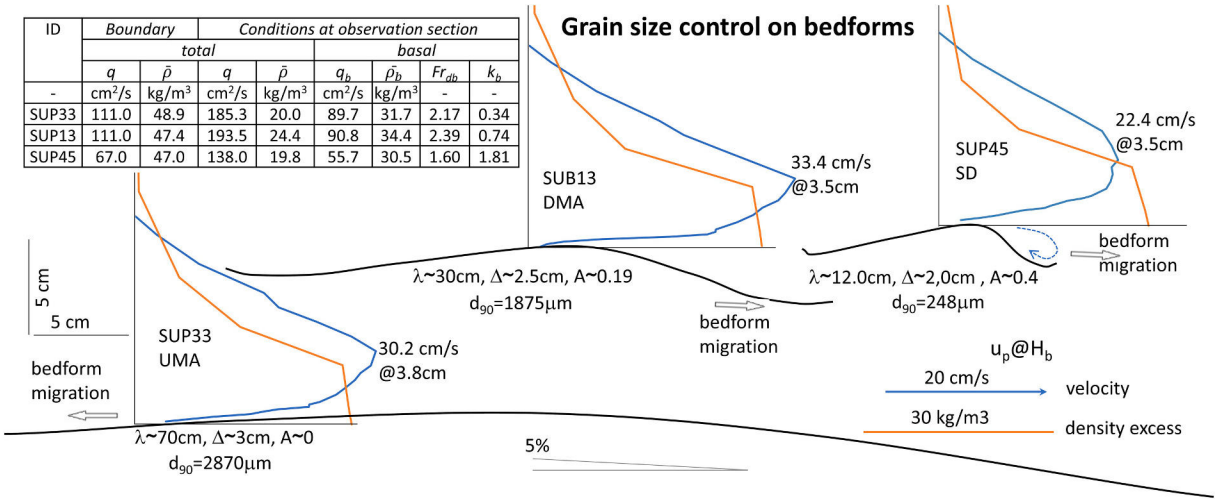

Fig. 31. Grain size control on bedform. Three instances of density currents flowing on the same bed slope (S = 5 %) sediment type (ρ_s = 1530 kg/m^3), and very similar specific discharge and density (Sequeiros et al., 2010a). The current with the coarsest bed material (d_{90} = 2870 mm, left) results in upstream migrating antidunes, the current with bed material d_{90} = 1875 mm (middle) in downstream migrating antidunes, and the current with the finest bed material (d_{90} = 248 mm, right) in supercritical dunes. Data in table correspond to single profiles, not to spatially averaged profiles.

turbidity currents was the requirement of a slope gradient steeper than 0.3 %.

Bedforms seem to occur within a limited range of slopes. In all experimental and field observations gathered in this study bedforms occur for slopes gentler than ~20 % (Fig. 13b). In the Comoros archipelago Tzevahirtzian et al. (2021) report bedforms (likely cyclic steps given their dimensions) on slopes up to 20° (~36 %), but they report none on the steeper upper reaches where only bedform-less gullies or channels incise the flanks of the islands. Bedforms are presumably washed away on steeper slopes. Clare et al. (2018) find a similar pattern of steep gullies without bedforms (average $S \sim 10° \sim 18$ %) and gentler channels ($S \sim 3°$) with bedforms off the coast of Tanna Island, Vanuatu.

Bedform dimensions appear to be related to slope and distance from the source area. Sediment waves on unconfined settings often decrease in size downslope (Monterey Fan levee, Normark et al., 1980; Bounty Channel levee, Carter et al., 1990; Var Fan levee, Piper and Savoye, 1993; La Palma and Selvage wave fields, Wynn et al., 2000a/b; Orinoco Valley, Ercilla et al., 2002b; Toyama Canyon levee, Nakajima et al., 1998; Hikurangi Channel levee, Lewis and Pantin, 2002; and Macauley Volcano, Pope et al., 2018 among many others). Reduction in wavelength and waveheight may result from loss of speed as the slope becomes gentler and the current becomes depositional. However, in some

unconfined settings such as the Cilaos proximal fan (Sisavath et al., 2011) and some wave fields in the South China Sea (Zhong, 2025) wavelength increases downslope.

On the other hand, in more confined settings wave dimensions increase downstream, even when slope decreases, such as in the Laurentian Eastern Valley where the average gravel bedform (interpreted to be supercritical dunes) wavelength increases from 30 m at 2000 m water depth to 70 m at 3500 m (Hughes Clarke et al., 1990). The increase in bedform size could be an indication of a turbidity current accelerating on the steep upper reaches. This seems to apply regardless of the type of bedform. In the Malaylay Canyon bedforms become larger downslope with decreasing slope; even when they likely transition from CS on the very steep upper reaches ($S \sim 20$ %) to UMA on the middle reaches ($S \sim 6$ %). Normandeau et al. (2016) report increasing downslope wavelength of likely CS as slope decreases in the Gravel River delta channels. The same pattern is found in the bedforms estimated to be CS on the Sulphur Bay submarine channel in Tanna Island (Clare et al., 2018). Cartigny et al. (2011) surmise that as the slope gets less steep the distance required for the acceleration of the flow after each hydraulic jump on the stoss side increases, leading to longer wavelength bedforms.

Average bed slopes usually decrease downstream, but in some cases the opposite is true, such as on the slopes of La Réunion Saint-Etienne sector (Babonneau et al., 2013) where bedform wavelength decreases with the increase of slope and grain size. The reason for this could be the rather abrupt transition from steep (~6 %) to very steep slopes (>20 %) where bedforms tend to be eroded.

7.6. Grain size control

Grain size (which controls skin roughness, e.g., García, 2008) exerts some control on wave morphology. For example, gravel rich waves have a greater height for the same wavelength than sand-rich waves (Wynn et al., 2002). Flemming (2022) summarizes several relations between grain size and size of ripples and dunes in rivers indicating that coarser material corresponds to larger bedforms (on average larger wavelength and waveheight). But this rule of thumb has limited application across the full spectrum of bedforms because, as mentioned in section 7.1, the largest bedforms found in unconfined settings are fine-grained, while coarse-grained bedforms found in confined settings are smaller.

For a given setting, i.e. confined or unconfined, coarser material is associated with larger bedforms provided the flow has the capacity and competence to move it. But paradoxically it is unconfined, dilute, and fine-grained (yet supercritical) currents that create cyclic steps, which are the largest submarine bedforms observed. Fig. 30 shows grain size against wavelength made dimensionless by Bonnefille's method $\left(R_b g/\nu^2\right)^{1/3}$, with Yalin (1964), Coleman and Melville (1996), and Flemming (2022) estimations for minimum, mean, and maximum limits derived for fluvial ripples and dunes. For a given bedform type and setting, the figure points to coarser grain sizes being associated with larger bedforms (see also García, 2008). However, no clear trend is observed among unconfined field CS and UMA, which appear widely scattered in their own space as the largest bedforms composed of the finest material.

There is a feedback between grain size (skin roughness) and flow in the same way that bedforms affect flow (section 7.4), by increasing H_b and lowering ρ_b, but this appears to be a second order effect.

Grain size seems also to affect what type of bedform is formed. Provided other factors remain the same, flume experiments indicate that coarser bed grain sizes favor the formation of UMA, intermediate sizes favor DMA, and finer grain sizes favor downslope-asymmetrical downstream migrating bedforms (SD/SR). Fig. 31 shows three instances of density currents flowing on the same bed slope, with very similar specific discharge and density, but over different sediment type. The current with the coarsest bed material forms UMA, the current with intermediate bed material forms DMA, and the current with the finest bed material forms SD. All currents are supercritical but the case with flow separation (SD) has the lowest Froude number.

Grain size may affect asymmetry of CS. Fluvial flume experiments by Cartigny et al. (2014) found that fine sands (160 μm) may favor downslope asymmetric CS, and medium sands (350 μm) may result in symmetric or upslope asymmetric CS.

7.7. Ripples or dunes?

Ripples and dunes are downstream-migrating, downslope-asymmetric bedforms under subcritical regime with flow detachment on the lee side. Thus they are geometrically very similar (e.g., Fig. 17) and for distinctions we have to look at flow characteristics and grain size. Ripples have a viscous boundary layer along the stoss side and its transition into turbulence. When grain size roughness prevents this from happening dunes are formed (García, 2008; Zanke and Roland, 2021). Most of our experimental ripples have ratios of skin roughness over viscous sublayer k_{sn}/δ_{vs} below unity. They do not affect the flow in any meaningful way, and appear in the Shields diagram only for low Re_p (Fig. 15). The opposite is true for dunes, and video evidence shows turbulent flow near the bed, significant bedload transport and bursts of sediment into suspension pointing to a hydraulically rough bottom. The basal layer upper surface and the interface are gently but clearly affected by the dunes.

Several criteria were considered to distinguish ripples from dunes. First is what we call the Yalin-Allen and Yalin-Best criteria based on a λ/d_{50} threshold of 2000 (Fig. 11b) and a waveheight to current thickness ratio Δ/H_b threshold of 1/6 (Fig. 11a), after Yalin (1964), Allen (1970) and Best (2005); then the Lapotre et al. (2017) criterion who introduced the Yalin number χ; then the Vanoni (1975) criterion $\tau^* = 317Re^{*-2.8}$, and finally, the viscosity criterion where the threshold is given by the viscous sublayer being equal to a characteristic grain size yielding $\tau^* = \left(11.6/Re_p\right)^2$(e.g., García, 2008) (Fig. 15).

We classify subcritical bedforms first with the Yalin-Allen and Yalin-Best criteria, and when this is not possible because of missing data, we apply the Lapotre et al. (2017) method, which is very similar to Vanoni's. The Yalin-Allen and Yalin-Best methods are prioritized because they are based on easily accessible parameters: flow depth, waveheight, wavelength and grain size. This approach is also the only one that includes waveheight in the assessment. It does not feature the shear stress, as do the other methods, but this is not necessarily a drawback. Estimating bed shear stress in density currents is more difficult than in fluvial flows and has a larger uncertainty, at least a factor of 2 or 3 based on Sequeiros et al. (2010a) experimental observations.

The viscous sublayer method does not account for any bedform dimension and, compared to Lapotre et al. (2017), is more biased toward ripples in fine sand and toward dunes in coarse sand.

As an alternative to the Yalin-Allen method, a simple threshold of $\lambda = 0.6$ m that many early studies have noted (section 2.2) could also be used. But we prefer the former because it is dimensionless. The Vanoni (1975) method is an alternative to Lapotre et al. (2017).

7.8. Ripples and dunes in supercritical regime?

Downstream migrating bedforms formed by supercritical density currents exhibit diverse morphologies and cannot be grouped together, as they result from fundamentally different physical processes.

The first issue concerns the distinction between bedforms with and without flow separation. The latter are symmetrical, sinusoidal, in-phase with the density current interface, and are termed downstream-migrating antidunes (DMA). After Fedele et al. (2016) the former are called supercritical dunes, which are downslope asymmetrical (though not as asymmetric as subcritical dunes), unlikely to be in-phase with the current interface and basal layer upper surface and have flow separation on the lee side (see Fig. 5d). This issue seems to have passed unnoticed in

fluvial bedforms due to the paucity of "supercritical dunes" observed in that environment (see section 7.2).

Further distinctions can be made among downstream migrating bedforms under the supercritical regime with flow separation. It is expected that for supercritical flow, the effect of viscosity becomes less relevant because the viscous sublayer should be thinner and may not play the same role as it plays in subcritical ripples. However, we have observations of supercritical density currents that develop rather small bedforms under limited bedload transport. They can be best described as "supercritical ripples" in view of their size and downslope asymmetry (Fig. 5a), as well as the estimated ratio between the viscous sublayer thickness and the skin roughness. Hence, in the supercritical regime we apply the same criteria that separate ripples from dunes in subcritical regime, and identify supercritical ripples (SR) and supercritical dunes (SD).

One might argue this is a matter of nomenclature, suggesting all bedforms with flow separation be classified as ripples or dunes. However, de Cala et al. (2020) highlight that subcritical dunes typically form independently of the flow interface, evolving gradually or through ripple coalescence until they grow large enough to generate sufficient turbulence to disrupt the interfaces. In contrast, supercritical bedforms are shaped from the outset by their interaction with waves propagating along the flow interfaces. This results in varying degrees of coupling with the flow interface and basal layer—clearly in-phase in UMA and DMA, and likely out-of-phase in SD. Ripples, regardless of Froude regime, generally do not influence any flow interface. These distinct formative mechanisms support differentiating SD from its subcritical counterpart.

7.9. Cyclic steps or upstream migrating antidunes?

It is not trivial to distinguish CS from UMA without flow evidence. We can point out some distinctions based on observations. Cyclic steps are composed of fine sediment up to sand ($d^* \sim 0.5$–10) while UMA are shifted toward a coarser sediment range well into medium gravel ($d^* \sim 1$–100) and beyond if fluvial data are considered (Fig. 14). However, UMA can also be formed with fine sediment at the boundary of fine sand and coarse silt, and even muds. Cyclic steps have the widest spectrum of asymmetry of all bedforms, while UMA are mostly symmetrical with $|A| < 0.25$ (Fig. 16, Fig. 17). Cyclic steps are steeper than UMA (Fig. 17) and have lower wavenumbers when assessed at their supercritical segment (Fig. 12, Fig. 16). While these parameters provide a guidance for distinguishing UMA from CS there is a fair amount of overlap.

The role that confinement or lack thereof plays in favoring UMA or CS is contentious. It can be argued that confined channels favor UMA over CS, and the opposite is true on channel levees. On channel thalwegs bedforms are shaped by coarser sediment, denser, faster and thicker flows (i.e. larger wavenumber k_b) which correlates with UMA observations. On levees and unconfined slopes finer sediment prevails and thinner flows develop (lower k_b), both associated with CS. Channel thalweg bedforms are often erosional or bypassing surface features with little internal structure remaining underneath from antecedent bedforms. Levee bedforms are usually depositional and can be easily tracked throughout the subsurface. These differences are seen in many canyon/levee systems such as Monterey and Hikurangi (Normark et al., 2002; Lewis and Pantin, 2002) and channel/slope systems such as the Fraser Delta illustrated in Fig. 21 (Hill, 2012).

High-energetic steep slopes favor CS over UMA. Antidunes are shown to form at smaller values of Froude number when compared to cyclic steps (e.g., Fig. 14, see also Fedele et al., 2016). In general bed gradient decreases as distributary sections of the turbiditic systems are approached (section 7.5), thus favoring lower Froude numbers distally, and promoting formation of UMA instead of CS (Fig. 13b).

Another parameter that may help tell UMA and CS apart is the stoss side slope S_s (Fig. 1). No current can flow against gravity for long before undergoing a hydraulic jump. Negative S_s are the norm in submarine bedforms, but when positive stoss slopes $S_s > 0.3$ % occur, a hydraulic jump is unlikely and the bedforms must be UMA (Fig. 18).

As wavelength is a function of discharge, flow unsteadiness forces adjustments in bedform size (Slootman and Cartigny, 2020). Under unsteady and transient turbidity currents, such as those triggered by typhoons in the submarine canyons of the Philippines (Sequeiros et al., 2019; Porcile et al., 2020), it is possible that both CS and UMA occur through the waxing and waning stages of the flow. At the peak, during formative flow conditions, it is believed that bedforms observed in the middle and lower reaches of the Malaylay Canyon are UMA, and in the waning stage the flow becomes weaker and thinner with conditions more conducive for CS (Fig. 23). In the upper and steeper reaches of the canyon (water depth < 120 m) bedforms are interpreted to be CS also given the likelihood of thinner flows in the lower relief channels that connect directly with the shelf break.

The predominance of fine-grained sediments associated with CS may be explained differently depending on the setting. In channelized settings the transcritical nature of the flow itself can be the reason. The subcritical stretch may act as a sediment trap for most of the coarse fraction that happens to be in the flow. Along a train of CS, the coarse material may be gradually filtered out becoming finer downstream. The likely CS train in the Sulphur Bay submarine channel described by Clare

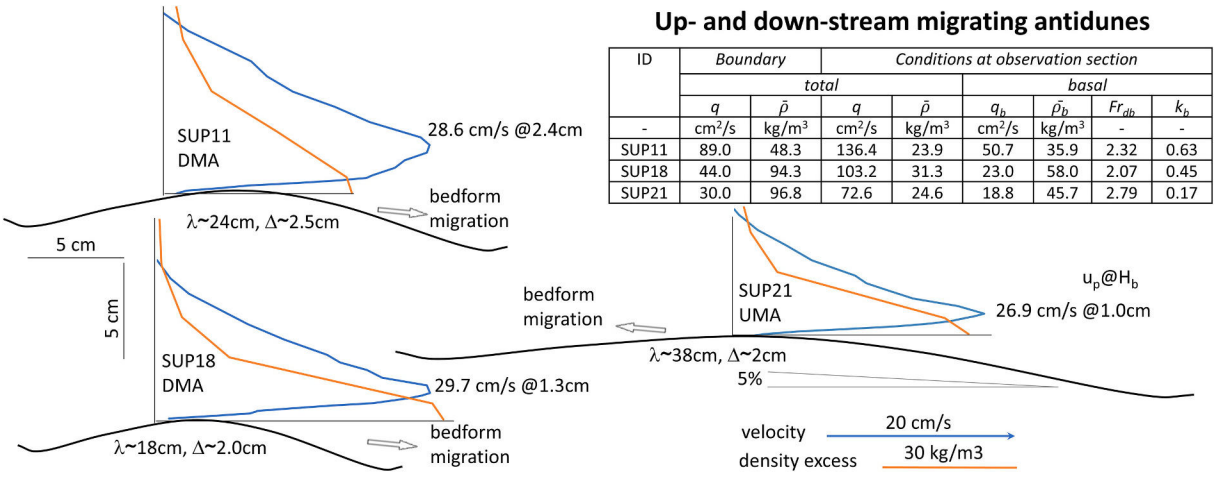

Up- and down-stream migrating antidunes

ID	Boundary		Conditions at observation section					
	total		total		basal			
	q	$\bar{\rho}$	q	$\bar{\rho}$	q_b	$\bar{\rho}_b$	Fr_{db}	k_b
-	cm²/s	kg/m³	cm²/s	kg/m³	cm²/s	kg/m³	-	-
SUP11	89.0	48.3	136.4	23.9	50.7	35.9	2.32	0.63
SUP18	44.0	94.3	103.2	31.3	23.0	58.0	2.07	0.45
SUP21	30.0	96.8	72.6	24.6	18.8	45.7	2.79	0.17

Fig. 32. Upstream and downstream migrating antidunes created under different flows but with the same bed material (P3) and bed slope (5 %) from Sequeiros et al. (2010a). Right: UMA created by high-density low-discharge flow. Bottom left: DMA formed by high-density intermediate discharge flow. Top left: DMA formed by low-density high-discharge flow. Data in table correspond to single profiles, not to spatially averaged profiles.

et al. (2018), where grain size rapidly and progressively becomes finer downstream from d_{50}/d_{90} ~ 295/600 μm to 90/350 μm within a few steps in the upper part of the canyon, seems to be a case in point. Conversely, CS on channel levees are created by turbidity currents that are composed from the beginning by the fine diluted upper fraction of the suspended sediment in the part of the current that manages to overspill the canyon. The Toyama Canyon levees have bedforms that seem to morph from CS to UMA downslope, the sediment on the stoss sides is commonly coarser than on the lee sides and downstream-fining is observed in both CS and UMA resembling features alike (Nakajima and Satoh, 2001).

Upstream migrating antidunes can also be composed of fines. This may be especially applicable to those located downstream of a train of CS that morph into less steep and smaller bedforms on the distal part of levees or unconfined settings as the slope becomes gentler and the current more depositional such as interpreted in the NE lower continental rise of the South China Sea (Wang et al., 2025), and in the overbank bedform field south of the lower Taiwan Canyon (a.k.a. South Taiwan Shoal, Zhong, 2025). Instances abound where levee bedforms proximal to the channel are large and steep, but distally they become smaller and less steep (but still migrating upslope), as in many fields mentioned in section 7.5 (e.g., Bounty, Toyama, La Palma, Hikurangi). We interpret these as CS gradually morphing downslope into UMA, as at some point bedform waveheight is low enough for the flow to go over it without breaking (and creating the hydraulic jump). In these cases, UMA and CS are of the same order of magnitude.

Our assessment agrees with Cartigny et al. (2011), who find that upslope migration together with a wide range of asymmetrical shapes, lack of cross-bedding indicative of streamwise migration and internal structures dominated by back-set bedding make a CS interpretation reasonable.

It has often been argued that antidunes are unlikely to preserve stable internal structures, as is often found in sediment waves, due to their unstable and breaking nature. This is based on experimental work, but it should not be taken as an absolute and extrapolated to field bedforms, for most antidunes produced in the laboratory were not in a net-aggradational setting that would favor preservation, and our experiments show that stable antidunes are also possible. The bedforms in the middle Malaylay canyon (Philippines), interpreted to be UMA, are uniquely documented by neat subsurface imagery (Fig. 23). The internal bed stratigraphy is well preserved on the stoss side with erosion on the lee side. If the bedform is net erosional (as in the upper canyon steeper slopes) the internal stratigraphy will be poorly preserved. West et al. (2019) report several preserved bedforms in outcrops, some of which seem to have been antidunes in deepwater slopes.

Laboratory studies near a model canyon-fan transition show that bed shear stress decreases when density or turbidity currents shift from supercritical to subcritical flow (García, 1994). This reduction significantly lowers bedload transport capacity, leading to sediment accumulation just downstream of the hydraulic jump (García and Parker, 1989). This suggests that changes in bedforms characteristics found in outcrops (e.g. antidunes to ripples-dunes) may indicate a change in flow regime via an internal hydraulic jump.

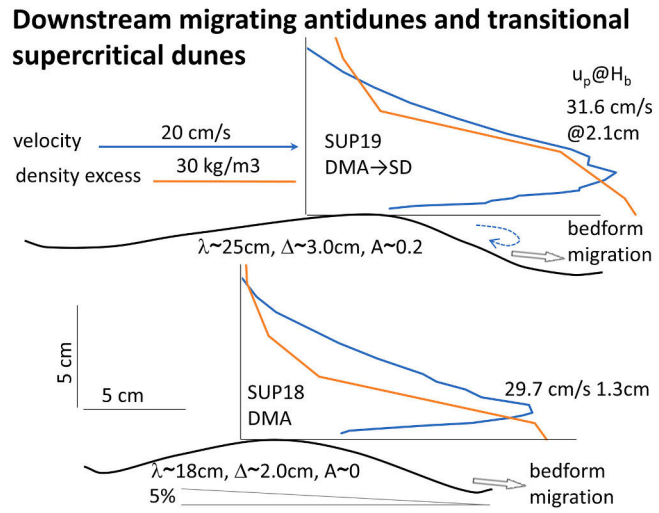

ID	Boundary		Conditions at observation section					
	total				basal			
	q	$\bar{\rho}$	q	$\bar{\rho}$	q_b	$\bar{\rho}_b$	Fr_{db}	k_b
-	cm²/s	kg/m³	cm²/s	kg/m³	cm²/s	kg/m³	-	-
SUP19	67.0	94.3	130.1	49.6	44.9	63.8	1.45	0.53
SUP18	44.0	94.3	103.2	31.3	23.0	58.0	1.57	0.46

Fig. 33. Downstream migrating antidunes (bottom) and transitional Supercritical dunes (top) created under different flows but with the same bed material (P3) and bed slope (5 %) from Sequeiros et al. (2010a). The larger thicker current induces the bedform on top, with imminent conditions for flow separation. Data in table correspond to single profiles, not to spatially averaged profiles.

7.10. When antidunes become cyclic steps

Transition from DMA (Spinewine et al., 2009) and UMA (Fedele et al., 2016) into CS have been observed in experimental density currents. Fedele et al. (2016) describe how the antecedent UMA undergo a random or sequential transition to CS through flow choking and appearance of an internal hydraulic jump. As the Froude number increased, for middle-sized sediments (P11), the UMA waveheight grew to trigger a quick and direct transition to CS. During the transition, the interface crest lagged slightly behind the UMA crest (also seen in Fig. 8a). The transition was direct, without the formation of either unstable antidunes or chutes-and-pools, as commonly reported for the fluvial case (e.g., Cartigny et al., 2014). The key feature is the overgrowth of the UMA crest becoming a local obstacle, inducing a hydraulic jump, and the flow regime becoming transcritical with the formation of stable CS. In the transitional early stage, the CS are of the same order of magnitude as the UMA. Spinewine et al. (2010) describe a similar process of UMA transitioning into would-be CS but with much coarser sediment (M1).

The process above described may happen in tandem with a steepening of the bed slope due to more sediment accumulation proximally and gradual thinning of the deposit in the downstream direction. This steepening was noted by Spinewine et al. (2009) as the bed slope gradually increased from S ~ 6 % to 9 % with medium-grained sediment (P5), and the bedforms evolved from DMA to CS. The transition from DMA to CS is not unlike that from UMA to CS; the difference being that the shorter DMA goes through a more chaotic/erosive process until the longer CS are established. The transition may be instigated by an incision into antecedent bed deposits at a given location, resulting in additional deposition just downstream of it. Sediment reworked by DMA becomes an obstacle to the flow, triggering the hydraulic jump that leads to the CS. As the first CS matures, several new CS are formed in sequence downstream, with an average wavelength at least four times longer than the antecedent DMA wavelength (see Fig. 8b).

Steeper slopes seem to favor CS formation, and to be a factor in triggering the transition to CS starting from DMA or UMA. This is conjectured in the Malaylay Canyon, where the steeper bedforms on the steep upper reaches (S ~ 11–21 %) are interpreted to be CS, and the gentler bedforms on the less steep middle reaches (S ~ 4–7 %) are likely UMA.

Seismic profiles also reveal UMA likely evolving into CS, e.g. in the overbank bedform field south of the lower Taiwan Canyon (Zhong, 2025) where bedforms appear to initiate as small reliefs (possibly incipient antidunes), and gradually evolve into larger scale bedforms over time.

For fluvial flows Cartigny et al. (2011) show that there can be a

gradual transition between short antidunes and CS. If Froude number increases over a train of antidunes, part of the train of antidunes starts to break while other parts return to UPB. This triggers a much longer slightly undulating bed beneath the antidune train that will then amplify and form a CS.

7.11. Upstream or downstream migrating antidunes?

Whether a bedform migrates upstream or downstream depends on many factors, including bed sediment size (section 7.6, Fig. 31). Changes in flow conditions can also result in bedform migration reversal. Fig. 32 shows cases of DMA and UMA created under the same bed material and slope but by different density currents. The more elongated UMA is associated with a high-density, low-discharge (thin) current. The shorter and steeper DMA is associated with a high-density intermediate-discharge current; and the larger DMA with a low-density high-discharge current. All currents are supercritical, with increasing wave number k_b from UMA to DMA. The ratio H_b/Δ increases from UMA to DMA. This indicates that, other variables being the same, thinner high-density flows tend to favor low-steepness upstream bedform migration; and that even changes in specific discharge alone can result in bedform migration reversal.

For fluvial bedforms, Kennedy (1960) noted cases where small flow changes led to either upstream or downstream migrating antidunes. Our observations agree with Núñez-González and Martín-Vide's (2011) energy balance theory, valid for symmetrical sinusoidal bedforms, which predicts that for a given Froude number, DMA are formed under higher wave numbers than UMA, and that DMA attain steeper Δ/λ ratios than UMA.

While thicker flows favor downstream migration, very thick flows may allow detachment on the lee side resulting in the more asymmetric SD bedforms.

7.12. Downstream migrating antidunes or supercritical-regime dunes?

Downstream migrating antidunes (DMA) and supercritical dunes (SD) are arguably the least observed bedforms at field scale, though some cases are known or plausibly interpreted (sections 6.5 and 6.6). Flow separation on the lee side of the bedforms and the associated downslope asymmetry are the distinct features that set SD apart from DMA. The factors that favor transition from DMA to SD are the same ones involved in transition from UMA to DMA: namely, flow discharge and density (section 7.4), and bed grain size (section 7.6).

Fig. 33 shows a DMA and a DMA transitioning to SD, both cases formed with the same bed material and slope but by different flows. The more symmetric DMA is formed by a current with lower discharge than the more downslope-asymmetric bedform, whose velocity profile has some early signs of flow separation on the lee side (i.e. recirculation cells below the crest level). Both currents are supercritical, but the one without flow separation more so. The basal flow wave number k_b and ratio H_b/Δ are larger in the case with flow separation. This indicates that, other variables being the same, thicker high-discharge flows favor flow separation.

7.13. Bedform development and transition

Previous sections have been devoted to describing different bedform types, as well as the control and feedback between bed slope, flow characteristics, grain size and bedform dimensions and shape. The process is complex and far from being fully understood. Under flume conditions the antecedent bed profile is usually plane. All observed bedforms are created from scratch and develop after a certain time into stable conditions. The exception are CS, which cannot be created starting from a plane bed, and need either a slope break (Fildani et al., 2006) or antecedent bedforms from which they can emerge (section

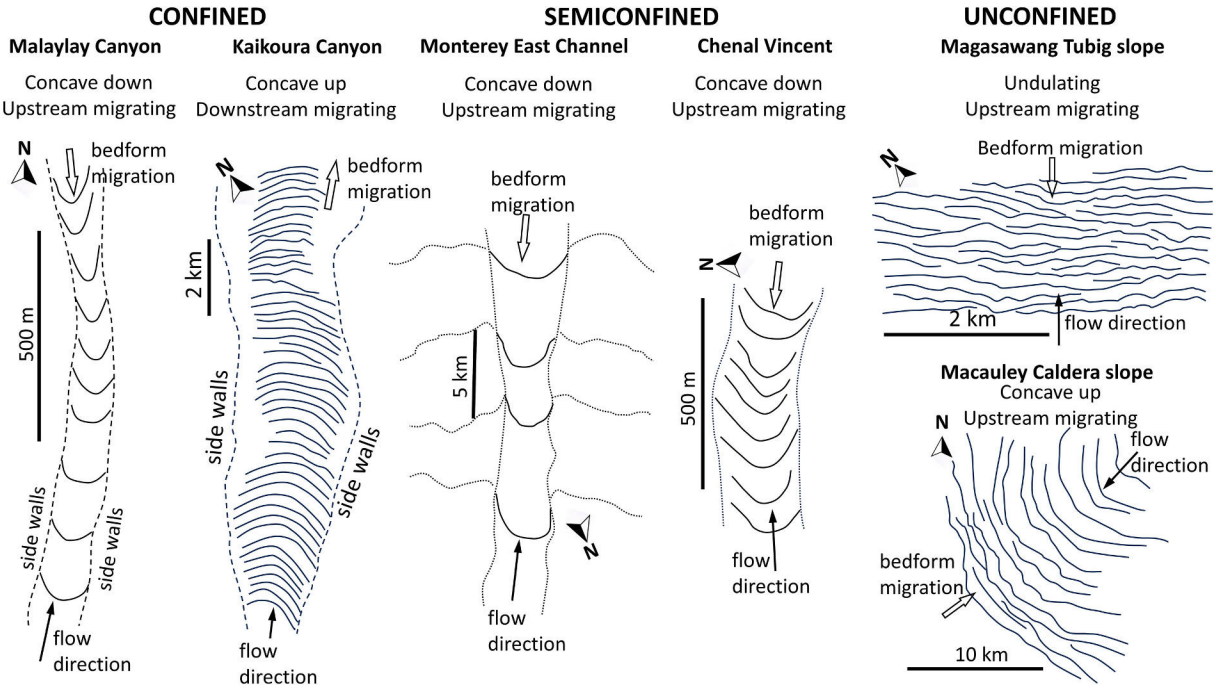

Fig. 34. Bedform migration and concavity of bedform crests under supercritical flows. In confined settings crest concavity indicates direction of bedform migration, such as in the Malaylay and Kaikoura Canyons that have concave down-channel and up-channel respectively. In settings with developing confinement, such as the Monterey East Channel and the bedform corridors within Chenal Vincent, crest concavity also reveals direction of bedform migration. Note that the side walls of Chenal Vincent are more than one kilometer away from the corridor. In unconfined plane slopes bedform crests are usually undulating and/or sinusoidal, such as on the Magasawang Tubig Slope, and bedform migration cannot be appraised from them. Likewise in radially unconfined settings, like the SW flank of the submarine Macauley Caldera, crest concavity does not indicate bedform migration. Black lines show bedform crests, dashed and dotted lines indicate side walls of developed and developing channels respectively. Source: Sequeiros et al., 2019; Mountjoy et al., 2018; Fildani et al., 2006; Porcile et al., 2020; Ollier et al., 1998; Saint-Ange et al., 2013; Pope et al., 2018.

7.10). The known required antecedents for CS are DMA and UMA, and SD could also be counted.

In principle, a gradual transition among bedforms is possible for a given slope and bed material provided discharge (a proxy for shear stress) is gradually increased mimicking the waxing stage in a natural unsteady current. If a steady flow is imposed from the beginning, intermediate transient bedforms may form before stable (asymptotic) bedforms are attained, e.g., the appearence of ripples before dunes are eventually formed by their coalescence (e.g., Coleman and Nikora, 2011). These boundaries have been studied for fluvial flows with empirical and theoretical approaches (e.g., McLean, 1990; van den Berg and van Gelder, 1993; Carling and Shvidchenko, 2002; Fourrière et al., 2010; Colombini and Stocchino, 2011; Núñez-González and Martín-Vide, 2011; Lapotre et al., 2017; Ohata et al., 2017).

In the case of density currents, de Cala et al. (2020) assessed development of bedforms under steady as well as waning flows. Under waning currents, pre-existing bed states can determine the subsequent evolution of bedforms, hence not all changes can be reversed in the short term by returning to original flow conditions. It was found that after UMA are developed by a formative flow, superimposed subcritical dunes and later DMA can develop over the relic UMA during the waning stage. Under antecedent bedforms, the evolution of later bedforms can be non-unique depending on multiple factors, including how fast the transient waning stage is for the bedforms to adjust. The proposed UMA/CS mode for the peak/waning stages over the bedforms in the Malaylay Canyon is akin to these observations (section 7.9).

Based on our experimental matrix we infer the following:

1) Larger basal specific discharges q_b increase current velocity U_b and thickness H_b, inducing larger bedforms. For downstream migrating bedforms, in particular with flow separation, it also facilitates larger wavenumbers k_b. This applies regardless of Froude number regime, and is also valid in fluvial flows.
2) Excess density, a variable directly related to the speed of density currents plays a distinct role. It increases U_b and induces larger bedforms, but does not increase H_b. In bedforms without flow separation, especially upstream migrating, this favors smaller k_b. We argue that, in addition to the reduced gravity effect that favors supercritical flows, the additional degree of freedom provided by the excess density can be another reason for the prevalence of upstream migrating bedforms in the submarine environment.

We propose some simple guidelines to distinguish changes in flow conditons that favor the development of one bedform over another given a certain slope and bed material for supercritical flow regime. These are not, however, intended to be used as hard rules for transition among bedform types.

1) If specific discharge and wavenumber increase in tandem ($\partial q_b > 0$ and $\partial k_b > 0$), then this favors the formation of SD over DMA, and DMA over UMA.
2) If excess density increases in tandem with wavenumber reduction ($\partial F_{eb} > 0$ and $\partial k_b < 0$), then this favors formation of UMA over DMA, and in both cases leads to eventual CS formation due to further bedform steepening.

The underlying assumption is that, for a given bedform type, changes in bedform waveheight and wavelength are proportional ($\partial\lambda \sim \partial\Delta$), which beyond the observed data spread is a reasonable assumption (Fig. 10).

Bedform regime diagrams indicate what type of bedforms will develop for specific formative conditions (e.g., flow strength and grain size). They should not necessarily be understood as diagrams describing transition from one bedform to another, though under some simple and controlled conditions, i.e. monotonic increase of discharge, they may function in that way too.

7.14. Migration direction and concavity of bedforms

Knowing migration direction is the first step to interpret bedform type. Erosion at the lee side of the bedform is a strong indicator for upstream migration (UMA/CS), because downstream migrating bedforms only erode their stoss sides. The clearest indication of migration is the internal structure, where backsets point to upstream migration, while foresets indicate downstream migration (Cartigny et al., 2011). This information is not always available though.

When viewed from above, the concavity of bedform crests (i.e. “crescentic” shape) in confined settings may reveal migration direction. Under supercritical flow conditions concave up-channel bedforms tend to migrate downstream (Kaikoura) and concave down bedforms tend to migrate upstream (e.g., Monterey, Squamish, Malaylay) as sketched in Fig. 34. That the point of maximum displacement along the bedform crest tends to be in the thalweg points to side wall effects that lower bedform migration celerity in the transverse direction away from the thalweg, arguably by the additional friction the side walls of the canyon/channel present to the flow. Larger flow depths and less friction make it more likely that maximum velocities occur at the channel thalweg (e.g., Wynn et al., 2002; Cartigny et al., 2011; Symons et al., 2016).

Subcritical bedforms migrate only downstream. Yet, under subcritical flow conditions, downslope migrating barchanoid dunes may also have concave down-channel crests (e.g., Amazon River, de Almeida et al., 2016), but the processes behind this particular bedform are not related to channel side wall effects. Barchanoid bedforms can also be formed by contour currents in areas of hard substrate and low sediment supply (Wynn and Stow, 2002). In any case they are an exception to the “concavity rule”, although barchan-shaped bedforms under density currents have not been clearly reported to date.

In unconfined settings bedform crests may have an undulating sinusoidal shape (e.g., Symons et al., 2016; Porcile et al., 2020) with alternating down and upslope concavity and migration direction cannot be detected from them. Whenever channels carve out an unconfined slope such as the Monterey East Channel and the Magasawang-Tubig Channel do (Fildani et al., 2006; Porcile et al., 2020), the “concavity rule” still applies because some degree of confinement is created.

Wide canyons and valleys, while technically providing some degree of confinement, may be more than an order of magnitude wider than bedform crest length. Yet, it is not uncommon to find trains of bedforms in narrower and shallower corridors that act as de facto channels within the channel and may exhibit some degree of crest concavity (Symons et al., 2016). For example, the many channels within Chenal Vincent off the eastern coast of La Réunion, Ollier et al., 1998; Saint-Ange et al., 2013).

In radially unconfined settings, however, crest concavity should not be used to infer bedform migration. Concave upward crescentic supercritical bedforms can migrate upstream when formed by currents spreading radially from a point source such as mouth of canyons, fans, and submarine volcanos. The bedforms on the southwest flank of the submarine Macauley Caldera are such an example (Pope et al., 2018).

7.15. Bedload and suspended load

Suspended to bedload ratio plays a role in bedform formation, but this has been underinvestigated in field studies. Cartigny (2012) conjectured that bedform stability diagrams might depend on the density of the turbidity current basal layer. Among other effects, under thick “high-density” currents ripples and dunes would be washed away and replaced with plane bed regime. These so-called “high-density” turbidity currents speculated to have near bed volumetric concentrations ranging from 0.3 to 0.5 (i.e., more than four times higher than the average equivalent basal layer concentration in our experimental density current dataset) could be partially explained as dense bedload driven by the current basal layer. Recent work in fluvial environments that may apply to density

currents is discussed in the Supplementary Material.

7.16. What has been excluded

Sediment bedform types that are mostly shaped by **internal waves** have been excluded: e.g., those in the Navarinsky Canyon head, Central Adriatic Shelf; Llobregat Prodelta, Valencia Slope (Karl and Carlson, 1982; Karl et al., 1986; Cattaneo et al., 2004; Urgeles et al., 2011; Ribó et al., 2016). Also excluded are bedforms associated with **tides**, such as in the Whittard Canyon, distal Monterey Canyon at 1850 m water depth (Lo Iacono et al., 2020; Wolfson-Schwehr et al., 2023); those associated with **contour currents** as in Fluvia-Muga, Uruguay and northern Argentina Slopes (Urgeles et al., 2011; Hernández-Molina et al., 2018; Principi et al., 2024); and **shallow water currents** as in the Ebro Prodelta (Urgeles et al., 2011). Likewise, features associated with **slope failure** or **creep** such as on the Sarno Prodelta, Corigliano Basin in the western Gulf of Taranto, or the western flank of Raoul Island (e.g., Sacchi et al., 2005; Rebesco et al., 2009; Pope et al., 2018) have been disregarded.

All of these phenomena result in transverse sediment bedforms or bedform-like features that are sometimes difficult to tell apart from the bedforms generated by bottom density flows that are addressed in this study. Criteria to distinguish bedforms created by contour and turbidity currents, and both of them from creep folds are provided by Wynn and Stow (2002) and Rebesco et al. (2009).

Finally, bedforms buried deep in the sedimentary record have been excluded when the observable bed slope is deemed to have changed due to deformation and tilting. The Early Cretaceous sediment waves, likely CS, in the Guinea Plateau described by Duarte et al. (2025) are such an example.

8. Conclusions

We carried out a comprehensive study of the bedforms created by density currents encompassing both experimental and field data and contrasted them with fluvial bedforms. We conclude that:

- All bedform types observed in rivers are also created through submarine processes, but in different proportions. Subcritical dunes in particular seem to be rare in the submarine environment, where supercritical bedforms prevail. This is probably due to the elevated Froude numbers associated with reduced gravity; scarce observations on deep and gentle-sloped submarine environments, and the reworking there by deep contour currents. This mirrors the scarcity of supercritical dunes in fluvial flows.
- In addition to the reduced gravity effect that favors supercritical flow, the additional degree of freedom provided by the excess density as a variable in density currents can be another reason for the prevalence of upstream migrating bedforms in the submarine environment.
- Bedform type similarities are found throughout a span of five orders of magnitude in bedform dimensions for subcritical and supercritical regime ripples/dunes, downstream- and upstream-migrating antidunes, and cyclic steps.
- When density currents are evaluated based on their basal (lower) layer characteristics, the same boundaries that distinguish fluvial bedforms also apply to subaqueous bedforms across established and newly introduced regime diagrams. As pointed out by Ohata et al. (2023), we argue that accurate prediction of bedforms formed by density currents is only possible when using metrics from the basal layer.
- The new regime diagrams contribute to bedform interpretation in the field, by suggesting a reduced number of unknown input parameters to establish paleoflow hydrodynamics.
- New criteria are proposed to interpret and distinguish bedform types and summarized in a practical flow diagram (Fig. 20) with direct application in sedimentology, geology, and engineering.
- We introduce simple guidelines to understand how changes in flow conditons, grain size, and slope may favor the development of one bedform over another.

Glossary

Basal layer	the lower part of the current, from the bed to the point of peak velocity u_p
C	canyons and channels
CS	cyclic step
D	dune formed under subcritical flow regime
DMA	downstream-migrating antidune
F	fans and islands
In phase	when the crests and troughs of the bedforms are mostly aligned with the crests and troughs of the interface (or the basal layer upper surface, which is the interface between the basal and upper layers).
Interface	surface between the upper layer and the ambient fluid
L	channel levees
LPB	lower-regime plane bed
Out of phase	the opposite of 'in phase'
R	ripple formed under subcritical flow regime
S	slopes, rises and basins
SD	dune formed under supercritical flow regime
SR	ripple formed under supercritical flow regime
Subcritical bedform	bedform formed under subcritical flow regime
Supercritical bedform	bedform formed under supercritical flow regime
SW	standing wave bedform
T	transitional bedform, e.g., from one type of bedform to another
UMA	upstream-migrating antidune
UMAT	upstream-migrating antidune transition to CS
Upper layer	the upper part of the current, from the point of peak velocity u_p to the interface with the ambient fluid
UPB	upper-regime plane bed

Notation

A	asymmetry parameter $=(L_{stoss}-L_{lee})/\lambda$
d_i	characteristic diameter in the ith grain size
d_g	geometric mean grain size $=(d_{84}d_{16})^{1/2}$
d_{50}	median sediment grain size
d^*	dimensionless grain size (Bonnefille) $=d_{50}\left(R_b g/\nu^2\right)^{1/3}=\left(Re_p\right)^{2/3}$
F_e	layer-averaged fractional excess density $=(\overline{\rho}-\rho_a)/\overline{\rho}$
F_{eb}	layer-averaged fractional excess density of the basal layer $=(\overline{\rho_b}-\rho_a)/\overline{\rho_b}$
Fr_d	densimetric Froude number of the current$=U/\sqrt{F_e g H}$
Fr_{db}	densimetric Froude number of the current basal layer $=U_b/\sqrt{F_{eb}gH_b}$
g	gravitational acceleration
H	layer-averaged flow thickness
H_i	flow thickness from the bed to the interface
H_b	basal flow thickness, measured from bed to u_p (for fluvial flows $H\approx H_b$)
$H_b{}^{*A}$	dimensionless basal flow thickness (Allen) $=H_b/d_{50}$
$H_b{}^{*B}$	dimensionless basal flow thickness (Bonnefille) $=H_b\left(R_b g/\nu^2\right)^{1/3}$
k_{sn}	skin roughness $=2.5\ d_{90}$
k	dimensionless bedform wavenumber $=2\pi H/\lambda$
k_b	dimensionless basal bedform wavenumber $=2\pi H_b/\lambda$
L_{lee}	length of the lee side of the bedform

L_{stoss}	length of the stoss side of the bedform
q	specific discharge $= UH$
q_b	basal specific discharge $= U_b H_b$
q_s	specific volume sediment transport rate (bedload and suspended)
u_{mig}	bedform migration rate
u	flow velocity
u_p	peak flow velocity
u_*	shear velocity $= \sqrt{\tau_b/\rho_b}$
u_{s*}	skin shear velocity $= \sqrt{\tau_{bs}/\rho_b}$
U	layer-averaged flow velocity
U_b	layer-averaged flow velocity of the basal layer
$U_b{}^{*B}$	dimensionless layer-averaged basal flow velocity (Bonnefille) $= U_b(R_b g\nu\ )^{-1/3}$
R_b	near-bed submerged specific density of sediment $= (\rho_s - \rho_b)/\rho_b$
Re_p	particle Reynolds number $= \sqrt{gR_b d_{50}}d_{50}/\nu = (d^*)^{3/2} = Re^*/(\tau^*)^{1/2}$
$Re*$	shear Reynolds number $= u_* d_{50}/\nu = Re_p(\tau^*)^{1/2}$
S	average bed slope
S_s	average stoss side slope $= S - \Delta/L_{stoss}$
T_i	inflow temperature (lab)
T_f	flume water temperature (lab)
z_0	bed roughness height
δ_{vs}	viscous sublayer $= 11.6\,\nu/u_{s*}$
θ_b'	mobility parameter of the basal flow $= U_b{}^2/\left[R_b d_{50}(18\log(4H_b/d_{90}))^2\right]$
κ	Von Karman coefficient $= 0.405$
Δ	bedform waveheight
Δ^{*A}	dimensionless bedform waveheight (Allen) $= \Delta/d_{50}$
λ	bedform wavelength
λ^{*A}	dimensionless bedform wavelength (Allen) $= \lambda/d_{50}$
λ^{*B}	dimensionless bedform wavelength (Bonnefille) $= \lambda\left(R_b g/\nu^2\right)^{1/3}$
λ^{*L}	dimensionless bedform wavelength (LaPotre) $= \lambda u_*/\nu$
ν	kinematic viscosity of the fluid
ρ	density of the flow
$\overline{\rho}$	layer-averaged flow density
$\overline{\rho_b}$	layer-averaged flow density of the basal layer
ρ_a	density of the ambient fluid above the interface
ρ_b	near-bed density of the saline/sediment-laden flow
ρ_s	density of the sediment
σ_g	geometric grain size standard deviation $= (d_{84}/d_{16})^{1/2}$
τ_b	bed shear stress
τ_{bs}	bed shear stress (skin friction component)
τ_{bf}	bed shear stress (drag component)
τ^*	dimensionless shear stress (Shields number of bed mobility) $= \tau_b/(\rho_b R_b g d_{50})$
$\tau_s{}^*$	skin shear fraction of τ^*
$\tau_s{}^*$	drag fraction of τ^*
χ	Yalin number $= Re^*\sqrt{\tau^*} = \tau^* Re_p$
ζ	bedform steepness $= \Delta/\lambda$

Declaration of competing interest

The authors have nothing to declare.

Acknowledgments

Philip Hill and Robert Kung for providing bathymetry of Fraser Delta. John Hughes Clarke and Christopher Stevenson for sharing data and insightful discussion on the Laurentian bedforms. Eve Lundsten and Charles Paull for providing bathymetry of Monterey Canyon. Galderic Lastras for providing additional data and insights of the Setubal Canyon. Fermín Palma for sharing additional Sloggett Canyon profiles and insights. Biwen Wang and Guangfa Zhong for explaining several datasets in the South China Sea. Koji Ohata, Rafael Manica, Francisco Nuñez-González, Mathieu Lapôtre and Silke Wieprecht for providing their own datasets of bedforms and guidance. William R. Brownlie for helping to understand his dataset. ENI and TOTAL for sharing data of Mozambique submarine canyons. Shell for supporting the publication of this study. Arnoud Slootman and an anonymous referee for providing comprehensive constructive critique and enhancing the final version of the manuscript.

Appendix A. Supplementary data

Supplementary data to this article can be found online at https://doi.org/10.1016/j.earscirev.2025.105322.

Data availability

Experimental data reported in this study are uploaded to the Zenodo Gravity Flows repository https://zenodo.org/communities/gravityflows/. The file lists all relevant, measured or calculated experimental parameters that have served as inputs to constructing the bedform diagrams. Further data can be made available upon request.

References

Alexander, J., Fielding, C., 1997. Gravel antidunes in the tropical Burdekin River, Queensland, Australia. Sedimentology 44, 327–337.
Allen, J.R., 1970. Physical Processes of Sedimentation. Unwin University Books, London, 248 p.
Allen, J.R., 1982. Sedimentary Structures: Their Character and Physical Basis, vol. 1. In: Developments in sedimentology series, vol. 30. Elsevier, New York, 593 p.
Allen, J.R.L., 1991. The Bouma division and the possible duration of turbidity currents. J. Sediment. Petrol. 61, 291–295.
Anderskouv, K., Surlyk, F., Huuse, M., Lykke-Andersen, H., Bjerager, M., Tang, C.D., 2010. Sediment waves with a biogenic twist in Pleistocene cool water carbonates, Great Australian Bight. Mar. Geol. 278 (1), 122–139.
Anderson, A.G., 1953. The characteristics of sediment waves formed by flow in open channels. In: Proceedings, 3rd Midwest Conference on Fluid Mechanics. University of Minnesota, pp. 379–395.
Arzola, R., Wynn, R.B., Lastras, G., Masson, D.G., Weaver, P.P.E., 2008. Sedimentary features and processes in submarine canyons: a case study from the Nazaré and Setúbal Canyons, west Iberian margin. Mar. Geol. 250, 64–88.
Ashley, G.M., 1990. Classification of large-scale subaqueous bedforms: a new look at an old problem. J. Sediment. Petrol. 60, 160–172.
Baas, J.H., Dam, R.L., Storms, J.E.A., 2000. Duration of deposition from decelerating high-density turbidity currents. Sediment. Geol. 136, 71–88.
Babakaiff, C.S., Hickin, E.J., 1996. Coherent flow structures in Squamish River Estuary, British Columbia, Canada. In: Ashworth, P.J., et al. (Eds.), Coherent Flow Structures in Open Channels. John Wiley, Hoboken, N. J, pp. 321–342.
Babonneau, N., Delacourt, C., Cancouët, R., Sisavath, E., Bachèlery, P., Mazuel, A., Jorry, S.J., Deschamps, A., Ammann, J., Villeneuve, N., 2013. Direct sediment transfer from land to deep-sea: insights into shallow multibeam bathymetry at La Réunion Island. Mar. Geol. 346, 47–57.
Bagnold, R.A., 1966. An approach to the sediment transport problem from general physics. Physiographic and hydraulic studies of rivers. In: Geological Survey Professional Paper 422–1. USA Gov. Printing Office, Washington, 42 p.
Bárcenas, P., Fernández-Salas, L.M., Macías, J., Lobo, F.J., y Díaz del Río, V., 2009. Estudio morfométrico comparativo entre las ondulaciones de los prodeltas de los rios de Andalucía Oriental. Rev. Soc. Geol. Esp. 22 (1–2), 43–56.
Bartholdy, J., Ernstsen, V.B., Flemming, W., Winter, C., Bartholomä, A., Kroon, A., 2015. On the formation of current ripples. Sci. Rep. 5. https://doi.org/10.1038/srep11390. Article number: 11390.
Bennett, S., Best, J., 1996. Mean flow and turbulence structure over fixed ripples and the ripple-dune transition. In: Ashworth, P.J., Bennett, S.J., Best, J.L., McLelland, S.J. (Eds.), Coherent Flow Structures in Open Channels. John Wiley, Hoboken, N.J, pp. 67–125.
Best, J., 2005. The fluid dynamics of river dunes: A review and some future research directions. J. Geophys. Res. 110, F04S0.
Blom, A., Ribberink, J.S., de Vriend, H.J., 2003. Vertical sorting in bed forms: Flume experiments with a natural and a trimodal sediment mixture. Water Resour. Res. 39 (2), 1025. https://doi.org/10.1029/2001WR001088.
Bo Pedersen, F., 1980. A Monograph on Turbulent Entrainment and Friction in Two Layer Stratified Flow, 397 pp. Inst. of Hydrodyn. and Hydraul. Eng., Tech. Univ. of Denmark, Kongens Lyngby.

Bonnefille, R., 1963. Essais de synthèse des lois de début dentraînement des sédiments sous laction dun courant en régime uniform. Bulletin Centre de Recherche Chatou 5, 67–72.
Bornhold, B.D., Prior, B.D., 1990. Morphology and sedimentary processes on the subaqueous Noeick River Delta, British Columbia, Canada. In: Colella, A., Prior, D.B. (Eds.), Coarse Grained Deltas. Blackwell Scientific Publications, Oxford, pp. 169–185.
Bouma, A.H., Treadwell, T.K., 1975. Deep-sea dune-like features. Mar. Geol. 19 (5), M53–M59.
Bradley, R.W., Venditti, J.G., 2017. Reevaluating dune scaling relations. Earth Sci. Rev. 165, 356–376.
Bridge, J.S., 2003. Rivers and Floodplains: Forms, Processes and Sedimentary Record. Blackwell Publishing, Oxford, UK, 491 p.
Bridge, J.S., Best, J.L., 1988. Flow, sediment transport and bedform dynamics over the transition from dunes to upper-stage plane beds: implications for the formation of planar laminae. Sedimentology 35, 753–763.
Brownlie, W.R., 1981. Prediction of Flow Depth and Sediment Discharge in Open Channels. Report No. KH-R-43A,. Keck Laboratory of Hydraulics and Water Resources, California Institute of Technology, Pasadena, California.
Carling, P.A., 1999. Subaqueous gravel dunes. J. Sediment. Res. 69, 534–545.
Carling, P.A., Shvidchenko, A.B., 2002. A consideration of the dune:antidune transition in fine gravel. Sedimentology 49, 1–15.
Carter, L., Carter, R.M., Nelson, C.S., Fulthorpe, C.S., Neil, H.L., 1990. Evolution of Pliocene to recent abyssal sediment waves on Bounty Channel levees, New Zealand. Mar. Geol. 95, 97–109.
Cartigny, M.J.B., 2012. Morphodynamics of Supercritical High-Density Turbidity Currents. Ph.D. Thesis.. Universiteit Utrecht, 161 p.
Cartigny, M.J.B., Postma, G., 2016. Turbidity current bedforms, p. In: Guillén, Jorge, et al. (Eds.), 29–33 in: Atlas of Bedforms in the Western Mediterranean. Springer, 320 p.
Cartigny, M.J.B., Postma, G., van den Berg, J.H., Mastbergen, D.R., 2011. A comparative study of sediment waves and cyclic steps based on geometries, internal structures and numerical modeling. Mar. Geol. 280 (1–4), 40–56.
Cartigny, M.J.B., Ventra, D., Postma, G., Den Berg, J.H., 2014. Morphodynamics and sedimentary structures of bedforms under supercritical-flow conditions: new insights from flume experiments. Sedimentology 61, 712–748.
Casalbore, D., Romagnoli, C., Bosman, A., Chiocci, F.L., 2014. Large-scale seafloor waveforms on the flanks of insular volcanoes (Aeolian Archipelago, Italy), with inferences about their origin. Mar. Geol. 355, 318–329.
Casalbore, D., Clare, M.A., Pope, E.L., et al., 2021. Bedforms on the submarine flanks of insular volcanoes: new insights gained from high resolution seafloor surveys. Sedimentology 68, 1400–1438.
Cattaneo, A., Correggiari, A., Marsset, T., Thomas, Y., Marsset, B., Trincardi, F., 2004. Seafloor undulation pattern on the Adriatic shelf and comparison to deep-water sediment waves. Mar. Geol. 213 (1–4), 121–148.
Cerrillo-Escoriza, J., Micallef, A., Lobo, F.J., et al., 2024. Bedform development in confined and unconfined settings of the Carchuna Canyon (Alboran Sea, western Mediterranean Sea): an example of cyclic steps in shelf-incised canyons. Mar. Geol. 478, 107429.
Charru, F., Andreotti, B., Claudin, P., 2013. Sand ripples and dunes. Annu. Rev. Fluid Mech. 45, 469–493. https://doi.org/10.1146/annurev-fluid-011212-140806.
Chaubert, J., Chauvin, J.L., 1963. Fomatiion des Dunes et des Rides dans les Modeles Fluviaux, Bulletin de Centre de Recherches et d'Essais de Chatou, 4, France.
Cheel, R.J., 1990. Horizontal lamination and the sequence of bed phases and stratification under upperflow-regime conditions. Sedimentology 37, 517–529.
Chen, Y., Parsons, D.R., Simmons, S.M., Williams, R., Cartigny, M.J.B., Hughes Clarke, J. E., Stacey, C.D., Hage, S., Talling, P.J., Azpiroz-Zabala, M., Clare, M.A., Hizzett, J.L., Heijnen, M.S., Hunt, J.E., Lintern, D.G., Sumner, E.J., Vellinga, A.J., Vendettuoli, D., 2021. Knickpoints and crescentic bedform interactions in submarine channels. Sedimentology 68, 1358–1377.
Chen, Y., Lu, Y., Wang, X., et al., 2024. Spatial distribution of bedforms and related flow processes around canyon mouths: Insights from the Rovuma Basin (offshore Mozambique). Basin Res. 36 e12887.
Cisneros, J., Best, J., van Dijk, T., et al., 2020. Dunes in the world's big rivers are characterized by low-angle lee-side slopes and a complex shape. Nat. Geosci. 13, 156–162.
Clare, M.A., Le Bas, T., Price, D.M., Hunt, J.E., Sear, D., Cartigny, M.J.B., Vellinga, A., Symons, W., Firth, C., Cronin, S., 2018. Complex and cascading triggering of submarine landslides and turbidity currents at volcanic islands revealed from integration of high-resolution onshore and offshore surveys. Front. Earth Sci. 6, 22.
Coleman, S.E., Melville, B.W., 1994. Bed-form development. ASCE J. Hydraul. Eng. 120 (5), 544–560.
Coleman, S.E., Melville, B.W., 1996. Initiation of bed forms on a flat sand bed. ASCE J. Hydraul. Eng 122, 301–310.
Coleman, S.E., Nikora, V.I., 2011. Fluvial dunes: initiation, characterization, flow structure. Earth Surf. Process. Landf. 36, 39–57.
Coleman, S.E., Fedele, J.J., García, M.H., 2003. Closed-conduit bed-form initiation and development. J. Hydraul. Eng. ASCE 129 (12), 956–965.
Colombini, M., Stocchino, A., 2011. Ripple and dune formation in rivers. J. Fluid Mech. 673, 121–131.
Covault, J.A., Kostic, S., Paull, C.K., Ryan, H.F., Fildani, A., 2014. Submarine channel initiation, filling and maintenance from sea-floor geomorphology and morphodynamic modelling of cyclic steps. Sedimentology 61, 1031–1054.
Czapiga, M.J., McElroy, B., Parker, G., 2019. Bankfull Shields number versus slope and grain size. J. Hydraul. Res. 57 (6), 760–769.
Damuth, J.E., 1979. Migrating sediment waves created by turbidity currents in the northern South China Basin. Geology 7, 520–523.
de Almeida, R.P., Galeazzi, C.P., Freitas, B.T., Janikian, L., Ianniruberto, M., Marconato, A., 2016. Large barchanoid dunes in the Amazon River and the rock record: implications for interpreting large river systems. Earth Planet. Sci. Lett. 454, 92–102.
de Cala, I., Ohata, K., Dorrell, R., Naruse, H., Patacci, M., Amy, L.A., Simmons, S., McLelland, S.J., McCaffrey, W.D., 2020. Relating the flow processes and bedforms of steady-state and waning density currents. Front. Earth Sci. 8, 535743. https://doi.org/10.3389/feart.2020.535743.
Dinehart, R.L., 1992. Evolution of coarse gravel bedforms: Field measurements at flood stage. Water Resour. Res. 28, 2667–2689.
Duarte, D., Erba, E., Bottini, C., et al., 2025. Early Cretaceous deep-water bedforms west of the Guinea Plateau revise the opening history of the Equatorial Atlantic Gateway. Glob. Planet. Chang. 249, 104777.
Eakins, B.W., Robinson, J.E., 2006. Submarine geology of Hana Ridge and Haleakala Volcano's northeast flank, Maui. J. Volcanol. Geotherm. Res. 151 (2006), 229–250.
Ediger, V., Velegrakis, A.F., Evans, G., 2002. Upper slope sediment waves in the Cilician Basin, northeastern Mediterranean. Mar. Geol. 192, 321–333.
Endo, N., Masuda, F., 1997. Small ripples in dunes regime and interpretation about dunes-missing in turbidite. J. Geol. Soc. Jpn. 103 (8), 741–746.
Engelund, F., 1970. Instability of erodible beds. J. Fluid Mech. 42, 225–244.
Engelund, F., Fredsoe, J., 1982. Sediment ripples and dunes. Annu. Rev. Fluid Mech. 14, 13–37.
Ercilla, G., Wynn, R.B., Alonso, B., Baraza, J., 2002a. Initiation and evolution of turbidity current sediment waves in the Magdalena turbidite system. Mar. Geol. 192, 153–169.
Engelund, F., Hansen, E., 1967. A Monograph on Sediment Transport in Alluvial Streams. Danish Technical Press, Copenhagen, pp. 63–p.
Ercilla, G., Alonso, B., Wynn, R.B., Baraza, J., 2002b. Turbidity current sediment waves on irregular slopes: observations from the Orinoco sediment-wave field. Mar. Geol. 192, 171–187.
Faugères, J., Gonthier, E., Mulder, T., Kenyon, N., Cirac, P., Griboulard, R., Berne, S., Lesuave, R., 2002. Multi-process generated sediment waves on the Landes Plateau (Bay of Biscay, North Atlantic). Mar. Geol. 182, 279–302.
Fedele, J.J., García, M.H., 2009. Laboratory experiments on the formation of subaqueous depositional gullies by turbidity currents. Mar. Geol. 258, 48–59.
Fedele, J.J., Guintzel, C., Hoyal, D., 2009. Experiments on bedforms created by density currents. In: River, Coastal and Estuarine Morphodynamics: RCEM 2009 – Vionnet et al. (eds.) © 2010, 2. Taylor & Francis Group, London, pp. 833–841. ISBN 978-0-415-55426-8, V.
Fedele, J.J., Hoyal, D.C., Draper, J.M., 2011. Supercritical bedforms under density currents. In: River Coastal and Estuarine Morphodynamics – RCEM, 5., 2011, Beijing, China. Proceedings. Regional Civil Society Engagement Mechanism, Beijing, pp. 1–9.
Fedele, J.J., Hoyal, D.C., Barnaal, Z., Tulenko, J., Awalt, S., 2016. Bedforms created by gravity flows. In: Autogenic Dynamics and Self-Organization in Sedimentary Systems, SEPM Special Publication No 106.
Fernandez, R., Best, J., Lopez, F., 2006. Mean flow, turbulence structure, and bed form superimposition across the ripple-dune transition. Water Resour. Res. 42, W05406. https://doi.org/10.1029/2005WR004330.
Fildani, A., Normark, W.R., Kostic, S., Parker, G., 2006. Channel formation by flow stripping: large-scale scour features along the Monterey East Channel and their relation to sediment waves. Sedimentology 53, 1265–1287.
Flemming, B., 2022. The limits to growth: how large can subaqueous, flow-transverse bedforms ultimately become? Ocean Dyn. 72, 801–815.
Flood, R.D., 1988. A lee wave model for deep-sea mudwave activity. Deep-Sea Res. 35, 973–983.
Flood, R.D., Piper, D.J.W., Klaus, A., et al., 1995. Proceedings of the Ocean Drilling Program, Initial Reports 155.
Flood, R.D., Shor, A.N., Manley, P.L., 1993. Morphology of abyssal mudwaves at project MUDWAVES sites in the Argentine Basin. Deep-Sea Res. Part II Top. Stud. Oceanogr. 40, 859–888.
Fonseca Ribeiro, R., 2018. Evolucao e Geomorfologia Do Canion Do Sao Francisco e Do Talude Adjacente, Com Base Em Dados de batimetría Multifeixe. Dissertacao de Mestrado. Universidade Federal da Bahia, 77p.
Fourrière, A., Claudin, P., Andreotti, B., 2010. Bedforms in a turbulent stream: formation of ripples by primary linear instability and of dunes by nonlinear pattern coarsening. J. Fluid Mech. 649, 287–328.
Fox, P.J., Heezen, B.C., Harian, A.M., 1968. Abyssal anti-dunes. Nature 220, 470–472.
Frings, R.M., 2007. From gravel to sand. Downstream fining of bed sediments in the lower river Rhine. PhD thesis. Utrecht University.Netherlands Geographical Studies 368, Royal Dutch Geographical Society, Utrecht, The Netherlands.
Gabel, S.L., 1993. Geometry and kinematics of dunes during steady and unsteady flows in the Calamus River, Nebraska, USA. Sedimentology 40, 237–269.
García, M.H., 1994. Depositional turbidity currents laden with poorly-sorted sediment. ASCE J. Hydraul. Eng. 120 (11), 1240–1263.
García, M.H., 2008. Sedimentation Engineering: Processes, Measurements, Modeling and Practice, ASCE Manual of Practice 110. American Society of Civil Engineers, 1132 p.
García, M.H., Parker, G., 1989. Experiments on hydraulic jumps in turbidity currents near a canyon-fan transition. Science 117 (4), 393–396.
García, M.H., Parker, G., 1993. Experiments on the entrainment of sediment into suspension by a dense bottom current. J. Geophys. Res. 98 (C3), 4793–4807.
Gilbert, G.K., 1914. The transportation of debris by running water. In: U.S. Geological Survey Professional Paper, 86, 263 p.

Gong, C., Wang, Y., Peng, X., Li, W., Qiu, Y., Xu, S., 2012. Sediment waves on the South China Sea Slope off southwestern Taiwan: implications for the intrusion of the Northern Pacific deep water into the South China Sea. Mar. Pet. Geol. 32, 95–109.
Guiastrennec-Faugas, L., Gillet, H., Silva Jacinto, R., et al., 2020. Upstream migrating knickpoints and related sedimentary processes in a submarine canyon from a rare 20-year morphobathymetric time-lapse (Capbreton submarine canyon, Bay of Biscay, France). Mar. Geol. 423, 106143.
Guy, H.P., Simons, D.B., Richardson, E.V., 1966. Summary of Alluvial Channel Data from Flume Experiments, Professional Paper 462-I, 1956–1961. U.S. Geological Survey, 96 p.
Hage, S., Cartigny, M.J.B., Clare, M.A., Sumner, E.J., Vendettuoli, D., Hughes Clarke, J. E., Hubbard, S.M., Talling, P.J., Lintern, D.G., Stacey, C.D., Englert, R.G., Vardy, M. E., Hunt, J.E., Yokokawa, M., Parsons, D.R., Hizzett, J.L., Azpiroz-Zabala, M., Vellinga, A.J., 2018. How to recognize crescentic bedforms formed by supercritical turbidity currents in the geologic record: insights from active submarine channels. Geology 46 (6), 563–566.
Haq, E., Youliang, J., Shahzad, K., Mashwani, S.A., Ullah, H., Zaheer, M., 2021. Architectural complexities and morphological variations of the sediment waves of Plio-Pleistocene channel levee backslope of the Indus Fan. Rudarsko-geološko-naftni zbornik (The Mining-Geology-Petroleum Engineering Bulletin) 39–54. https://doi.org/10.17794/rgn.2022.2.4.
Harbor, D.J., 1998. Dynamics of bedforms in the lower Mississippi River. J. Sediment. Res. 68 (5), 750–762.
Heijnen, M.S., Clare, M.A., Cartigny, M.J.B., Talling, P.J., Hage, S., Lintern, D.G., Stacey, C., Parsons, D.R., Simmons, S.M., Chen, Y., Sumner, E.J., Dix, J.K., Hughes Clarke, J.E., 2020. Rapidly-migrating and internally-generated knickpoints can control submarine channel evolution. Nat. Commun. 11. https://doi.org/10.1038/s41467–020-16861-x.
Heiniö, P., Davies, R.J., 2009. Trails of depressions and sediment waves along submarine channels on the continental margin of Espirito Santo Basin, Brazil. GSA Bull. 121, 698–711.
Hernández Moreira, R., 2016. Deposits Emplaced in Upper Regime (Doctoral dissertation).. University of South Carolina, 122p.
Hernández-Molina, F.J., Campbell, S., Badalini, G., Thompson, P., Walker, R., Soto, M., Conti, B., Preu, B., Thieblemont, A., Hyslop, L., Miramontes, E., Morales, E., 2018. Large bedforms on contourite terraces: Sedimentary and conceptual implications. Geology 46, 27–30.
Hernández-Moreira, R., Jafarinik, S., Sanders, S., Kendall, C.G.St.C., Parker, G. and Viparelli, E. 2020. Emplacement of massive deposits by sheet flow. Sedimentology, 67, 1951–1972. Associated dataset Dryad: doi: https://doi.org/10.5061/dryad.c59zw3r9b.
Hill, P.R., 2012. Changes in submarine channel morphology and strata development from repeat multibeam surveys in the Fraser River delta, western Canada. In: Li, M.Z., Sherwood, C.R., Hill, P.R. (Eds.), Sediments, Morphology and Sedimentary Processes on Continental Shelves, 44. Int. Assoc. Sedimentol. Spec. Publ, pp. 47–70.
Hill, P.R., Lintern, D.G., 2022. Turbidity currents on the open slope of the Fraser Delta. Mar. Geol. 445, 106738.
Hoffmann, G., Silver, E., Day, S., Morgan, E., Driscoll, N., Orange, D., 2008. Sediment waves in the Bismarck volcanic arc, Papua New Guinea. Spec. Pap., Geol. Soc. Am. 436, 91–126.
Hoffmann, G., Silver, E., Day, S., Driscoll, N., Orange, D., 2011. Deformation versus deposition of sediment waves in the Bismarck Sea, Papua New Guinea. Mass-transport deposits in deepwater settings. SEPM Spec. Publ. 96, 455–474.
Howe, J.A., 1996. Turbidite and contourite sediment waves in the northern Rockall Trough, North Atlantic Ocean. Sedimentology 43, 219–234.
Huang, H., Imran, J., Pirmez, C., Zhang, Q., Chen, G., 2009. The critical densimetric Froude number of subaqueous gravity currents can be nonunity and non-existent. J. Sediment. Res. 79, 479–485. https://doi.org/10.2110/jsr.2009.048.
Hughes Clarke, J.E., 2016. First wide-angle view of channelized turbidity currents links migrating cyclic steps to flow characteristics. Nat. Commun. https://doi.org/10.1038/ncomms11896.
Hughes Clarke, J.E., Shor, A.N., Piper, D.J.W., Mayer, L., 1990. Large-scale current-induced erosion and deposition in the path of the 1929 Grand Banks turbidity current. Sedimentology 37, 613–629.
Imran, J., Parker, G., Harff, P., 2002. Experiments on incipient channelization of submarine fans. J. Hydraul. Res. 40 (1), 21–32.
Ippen, A.T., Harleman, D.R.F., 1952. Steady-state characteristics of subsurface flow. Natl. Bur. Standards Circ. 521, 79–93.
Izumi, N., Parker, G., 2009. The bifurcation pattern of the flat bed and antidune transition. In: Proceedings, Annual Hydraulic Engineering Conference, 53. Japan Society of Civil Engineering, 6 p.
Jacobi, R.D., Rabinowitz, P.D., Embley, R.W., 1975. Sediment waves on the Moroccan continental rise. Mar. Geol. 19, 61–67.
Jafarinik, S., 2022. Suspended and bedload transport in an open channel laboratory flume [Dataset]. Dryad. https://doi.org/10.5061/dryad.34tmpg4nk.
Jerolmack, D.J., Mohrig, D., 2005. A unified model for subaqueous bed form dynamics. Water Resour. Res. 41, w12421.
Julien, P.Y., Klaassen, G.J., 1995. Sand-dune geometry of large rivers during fl oods. J. Hydraul. Eng. 121, 657–663.
Karl, H., Carlson, P., 1982. Large sand waves in Navarinsky Canyon head, Bering Sea. Geo-Mar. Lett. 2, 157–162.
Karl, H.A., Cacchione, D.A., Carlson, P.R., 1986. Internal-wave currents as a mechanism to account for large sand wave in Navarinsky Canyon head, Bering Sea. J. Sediment. Petrol. 56 (5), 706–714.
Kennedy, J.F., 1960. Stationary Waves and Antidunes in Alluvial Channels. Ph.D. Thesis.. California Institute of Technology, 172 p.
Kennedy, J.F., 1963. The mechanics of dunes and antidunes in erodible bed channels. J. Fluid Mech. 16 (4), 521–544.
Kidd, R.B., Lucchi, R.G., Gee, M., Woodside, J.M., 1998. Sedimentary processes in the Stromboli Canyon and Marsili Basin, SE Tyrrhenian Sea: results from side-scan sonar surveys. Geo-Mar. Lett. 18, 146–154.
Kolla, V., Moore, D.G., Curray, J.R., 1976. Recent bottom-current activity in the deep western Bay of Bengal. Mar. Geol. 21 (4), 255–270.
Koller, D.K., 2020. Formas de Fundo Experimentais Geradas Por Correntes de Densidade Salinas e de Turbidez: análise Do Escoamento e Do Leito móvel. PhD Thesis.. Universidade Federal do Rio Grande do Sul, Porto Alegre, 266 p. hdl.handle.net/10183/217497.
Koller, D.K., de Oliveira Borges, A.L., Puhl, E., Manica, R., 2017. Prediction of the bedforms generated by density currents based on fluvial phase diagrams. In: Revista Brasileira de Recursos Hídricos Brazilian Journal of Water Resources. RBRH, Porto Alegre, 22. https://doi.org/10.1590/2318-0331.0217160021 e49.
Koller, D.K., Manica, R., de Oliveira Borges, A., Fedele, J.J., 2019. Experimental bedforms by saline density currents. Braz. J. Geol. https://doi.org/10.1590/2317-4889201920180118.
Koller, D.K., Manica, R., Fedele, J.J., 2022. Comparative hydraulic and sedimentologic study of ripple formation using experimental turbidity currents and saline currents. J. Sediment. Res. 92, 601–618. https://doi.org/10.2110/jsr.2021.076.
Komar, P.D., 1971. Hydraulic jumps in turbidity currents. Geol. Soc. Am. Bull. 82, 1477–1488.
Komar, P.D., 1985. The hydraulic interpretation of turbidites from their grain sizes and sedimentary structures. Sedimentology 32 (3), 395–407.
Kostic, S., Parker, G., 2003. Progradational sand-mud deltas in lakes and reservoirs. Part 2. Experiment and numerical simulation. J. Hydraul. Res. 41 (2), 141–152.
Kostic, S., Sequeiros, O., Spinewine, B., Parker, G., 2010. Cyclic steps: a phenomenon of supercritical shallow flow from the high mountains to the bottom of the ocean. J. Hydro-environ. Res. 3, 167–172.
Kuang, Z., Zhong, G., Wang, L., Guo, Y., 2014. Channel-related sediment waves on the eastern slope offshore Dongsha Islands, northern South China Sea. J. Asian Earth Sci. 79, 540–551.
Kubo, Y., Yokokawa, M., 2001. Theoretical study no breaking waves of antidunes. Spec. Pubs. Intl. Assoc. Sediment. 31, 65–70.
Lamb, M.P., Parsons, J.D., Mullenbach, B.L., Finlayson, D.P., Orange, D.L., Nittrouer, C. A., 2008. Evidence for superelevation, channel incision, and formation of cyclic steps by turbidity currents in Eel Canyon, California. Geol. Soc. Am. Bull. 120 (3–4), 463.
Lapotre, M.G.A., Lamb, M.P., McElroy, B., 2017. What Sets the Size of Current Ripples? The Geological Society of America, Item 2017063. https://doi.org/10.1130/G38598.1.
Lastras, G., Arzola, R.G., Masson, D.G., Wynn, R.B., Huvenne, V.A.I., Huhnerbach, V., Canals, M., 2009. Geomorphology and sedimentary features in the central Portuguese submarine canyons, western Iberian margin. Geomorphology 103, 310–329.
Leat, P.T., Tate, A.J., Tappin, D.R., Day, S.J., Owen, M.J., 2010. Growth and mass wasting of volcanic centers in the northern South Sandwich arc, South Atlantic, revealed by new multibeam mapping. Mar. Geol. 275, 110–126.
Leat, P.T., Day, S.J., Tate, A.J., Martin, T.J., Owen, M.J., Tappin, D.R., 2013. Volcanic evolution of the South Sandwich volcanic arc, South Atlantic, from multibeam bathymetry. J. Volcanol. Geotherm. Res. 265, 60–77.
Lee, H.J., Syvitski, J.P.M., Parker, G., Orange, D., Locat, J., Hutton, E.W.H., Imran, J., 2002. Distinguishing sediment waves from slope failure deposits: field examples, including the "Humboldt slide", and modelling results. Mar. Geol. 192, 79–104.
Lefebvre, A., Paarlberg, A.J., Winter, C., 2016. Characterising natural bedform morphology and its influence on flow. Geo-Mar. Lett. 36, 379–393.
Levchenko, O.V., Roslyakov, A.G., 2010. Cyclic sediment waves on western slope of the Caspian Sea as possible indicators of main transgressive/regressive events. Quat. Int. 225 (2), 210–220.
Lewis, K.B., Barnes, P.M., 1999. Kaikoura Canyon, New Zealand: active conduit from near-shore sediment zones to trench-axis channel. Mar. Geol. 162, 39–69.
Lewis, K.B., Pantin, H.M., 2002. Channel-axis, overbank and drift sediment waves in the southern Hikurangi Trough, New Zealand. Mar. Geol. 192, 123–151.
Li, J., Li, W., Alves, T.M., Rebesco, M., Zhan, W., Sun, J., Mitchell, N.C., Wu, S., 2019. Different origins of seafloor undulations in a submarine canyon system, northern South China Sea, based on their seismic character and relative location. Mar. Geol. 413, 99–111.
Li, W., Li, S., Alves, T.M., Rebesco, M., Geng, Y., 2021. The role of sediment gravity flows on the morphological development of a large submarine canyon (Taiwan Canyon), north-east South China Sea. Sedimentology 68, 1091–1108.
Lintern, D.G., Hill, P.R., Stacey, C., 2016. Powerful unconfined turbidity current captured by cabled observatory on the Fraser River delta slope, British Columbia, Canada. Sedimentology 63, 1041–1064.
Liu, J., Sun, M., Gao, H., Li, X., 2019. Features and Origin of Turbidity Current Sediment Waves in the Huatung Basin off the Eastern Taiwan Island. Acta Geol. Sin. (English Edition) 93 (4), 1088–1096.
Lo Iacono, C., Guillén, J., Guerrero, Q., et al., 2020. Bidirectional bedform fields at the head of a submarine canyon (NE Atlantic). Earth Planet. Sci. Lett. 542, 116321.
Lobo, F.J., Goff, J.A., Mendes, I., et al., 2015. Spatial variability of prodeltaic undulations on the Guadalfeo River prodelta: support to the genetic interpretation as hyperpycnal flow deposits. Mar. Geophys. Res. 36, 309–333.
Lonergan, L., Jamin, N.H., Jackson, C.A.-L., Johnson, H.D., 2013. U-shaped slope gully systems and sediment waves on the passive margin of Gabon (West Africa). Mar. Geol. 337, 80–97.
Lonsdale, P., Hollister, C.D., 1979. Cut-off at an abyssal meander south of Iceland. Geology 7, 597–601.

Lu, Y., Shi, B., Maselli, V., Luan, X., Xu, X., Shao, D., Fan, G., Wang, H., Ding, L., 2021. Different types of gravity-driven flow deposits and associated bedforms in the Upper Bengal Fan, offshore Myanmar. Mar. Geol. 441, 106609. https://doi.org/10.1016/j.margeo.2021.106609.

Ma, X., Yan, J., Song, Y., Liu, X., Zhang, J., Traykovski, P.A., 2019. Morphology and maintenance of steep dunes near dune asymmetry transitional areas on the shallow shelf (Beibu Gulf, northwest South China Sea). Mar. Geol. 412 (2019), 37–52.

Maggi, M.R., Negretti, M.E., Martin, A., Naaim-Bouvet, F., Hopfinger, E.J., 2024. Experimental study of gravity currents moving over a sediment bed: suspension criterion and bed forms. Environ. Fluid Mech. https://doi.org/10.1007/s10652-024-09998-6.

Malinverno, A., Ryan, W.B.F., Auffret, G., Pautot, G., 1988. Sonar images of the path of recent failure events on the continental margin off Nice, France. Geol. Soc. Am. Spec. Pap. 229, 59–75.

Mantz, P.A., 1977. Incipient transport of fine grains and flakes by fluids—extended shields diagram. J. Hydraul. Eng. ASCE 103 (6), 601–615.

Masson, D.G., Arzola, R.G., Wynn, R.B., Hunt, J.E., Weaver, P.P.E., 2011b. Seismic triggering of landslides and turbidity currents offshore Portugal. Geochem. Geophys. Geosyst. 12, Q12011.

Masson, D.G., Huvenne, V.A.I., de Stigter, H.C, et al., 2011a. Sedimentary processes in the middle Nazare Canyon. Deep-Sea Research II 58, 2369–2387.

Mazières, A., Gillet, H., Castelle, B., Mulder, T., Guyot, C., Garlan, T., Mallet, C., 2014. High-resolution morphobathymetric analysis and evolution of Capbreton submarine canyon head (Southeast Bay of Biscay—French Atlantic Coast) over the last decade using descriptive and numerical modeling. Mar. Geol. 351, 1–12.

Mazuel, A., Sisavath, E., Babonneau, N., et al., 2016. Turbidity current activity along the flanks of a volcanic edifice: the Mafate volcaniclastic complex, La Réunion Island, Indian Ocean. Sediment. Geol. 335, 34–50.

McBride, E.F., Shepherd, R.G., Crawley, R.A., 1975. Origin of parallel, near horizontal laminae by migration of bed forms in a small flume. J. Sediment. Res. 45 (1), 132–139.

McCave, I.N., 2017. Formation of sediment waves by turbidity currents and geostrophic flows: a discussion. Mar. Geol. 390, 89–93.

McHugh, C.M.G., Ryan, W.B.F., 2000. Sedimentary features associated with channel overbank flow: examples from the Monterey Fan. Mar. Geol. 163 (1), 199–215.

McLean, S., 1990. The stability of ripples and dunes. Earth Sci. Rev. 29, 131–144.

Middleton, G.V., 1966. Experiments on density and turbidity currents, part II. Uniform flow of density currents. Can. J. Earth Sci. 3, 627–637. https://doi.org/10.1139/e66-044.

Middleton, G.V., Southard, J.B., 1984. Mechanics of sediment movement. In: Society of Economic Paleontologists and Mineralogists, Short Course, 3, p. 401, 246 p.

Migeon, S., 2000. Dunes Geantes et Levees Sedimentaires en Domain Marin Profond: Approches Morphologique, Sismique et Sedimentologique. Ph.D. thesis,. Univ. Bordeaux I, Bordeaux.

Migeon, S., Savoye, B., Faugeres, J.-C., 2000. Quaternary development of migrating sediment waves in the Var deep-sea fan: distribution, growth pattern, and implication for levee evolution. Sediment. Geol. 133, 265–293.

Migeon, S., Savoye, B., Zanella, E., Mulder, T., Fauge, J., Weber, O., 2001. Detailed seismic reflection and sedimentary study of turbidite sediment waves on the Var Sedimentary Ridge (SE France): significance for sediment transport and deposition and for the mechanisms of sediment-wave construction. Mar. Pet. Geol. 18, 179–208.

Miramontes, E., Eggenhuisen, J.T., Silva Jacinto, R., Poneti, G., Pohl, F., Normandeau, A., Campbell, D.C., Hernández-Molina, F.J., 2020. Channel-levee evolution in combined contour current–turbidity current flows from flume-tank experiments. Geology 48 (4), 353–357.

Mohrig, D., Smith, J.D., 1996. Predicting the migration rates of subaqueous dunes. Water Resour. Res. 32 (10), 3207–3217.

Mountjoy, J.J., Howarth, J.D., Orpin, A.R., Barnes, P.M., Bowden, D.A., Rowden, A.A., Schimel, A.C.G., Holden, C., Horgan, H.J., Nodder, S.D., Patton, J.R., Lamarche, G., Gerstenberger, M., Micallef, A., Pallentin, A., Kane, T., 2018. Earthquakes drive large-scale submarine canyon development and sediment supply to deep-ocean basins. Sci. Adv. 4 eaar3748.

Muñoz, A., Elvira, E., León, C., Acosta, J., Jiménez, P., 2017. Examples of sediment waves in and around submarine canyons of the North Alboran Sea. In: Guillén, J., et al. (Eds.), Atlas of Bedforms in the Western Mediterranean. Springer, pp. 247–252.

Nakajima, T., Satoh, M., 2001. The formation of large mudwaves by turbidity currents on the levees of the Toyama deep-sea channel, Japan Sea. Sedimentology 48, 435±463.

Nakajima, T., Satoh, M., Okamura, Y., 1998. Channel-levee complexes, terminal deep-sea fan and sediment wave fields associated with the Toyama Deep-Sea Channel system in the Japan Sea. Mar. Geol. 147, 25–41.

Nelson, J.M., Smith, J.D., 1989. Flow in meandering channels with natural topography. In: Ikeda, S., Parker, G. (Eds.), River Meandering, Water Resources Monograph No. 12. American Geophysical Union, Washington, DC, pp. 69–102.

Niño, Y., Lopez, F., García, M.H., 2003. Threshold for particle entrainment into suspension. Sedimentology 50 (2), 247–263.

Nittrouer, J.A., Allison, M.A., Campanella, R., 2008. Bedform transport rates for the lowermost Mississippi River. J. Geophys. Res. 113, F03004. https://doi.org/10.1029/2007JF000795.

Normandeau, A., Lajeunesse, P., St-Onge, G., Bourgault, D., Drouin, S.S.O., Senneville, S., Belanger, S., 2014. Morphodynamics in sediment-starved inner-shelf submarine canyons (Lower St. Lawrence Estuary, Eastern Canada). Mar. Geol. 357, 243–255.

Normandeau, A., Lajeunesse, P., Poiré, A.G., Francus, P., 2016. Morphological expression of bedforms formed by supercritical sediment density flows on four fjord-lake deltas of the South-Eastern Canadian Shield (Eastern Canada). Sedimentology 63, 2106–2129.

Normandeau, A., Bourgault, D., Neumeier, U., Lajeunesse, P., St-Onge, G., Gostiaux, L., Chavanne, C., 2019. Storm-induced turbidity currents on a sediment-starved shelf: Insight from direct monitoring and repeat seabed mapping of upslope migrating bedforms. Sedimentology 67, 1045–1068.

Normandeau, A., Lajeunesse, P., Ghienne, J.-F., Dietrich, P., 2022. Detailed seafloor imagery of turbidity current bedforms reveals new insight into fine scale near-bed processes. Geophys. Res. Lett. 49 e2021GL097389.

Normark, W.R., Hess, G.R., Stow, D.A.V., Bowen, A.J., 1980. Sediment waves on the Monterey Fan levee: a preliminary physical interpretation. Mar. Geol. 37 (1–2), 1–18.

Normark, W.R., Piper, D.J.W., Posamentier, H., Pirmez, C., Migeon, S., 2002. Variability in form and growth of sediment waves on turbidite channel levees. Mar. Geol. 192 (2002), 23–58.

Núñez-González, F., 2012. Bedload Transport of Sand-Gravel Mixtures with Antidunes: Flume Experiments. PhD Thesis,. Technical University of Catalonia.

Núñez-González, F., Martín-Vide, J.P., 2011. Analysis of antidune migration direction. J. Geophys. Res. 116, F02004. https://doi.org/10.1029/2010JF001761.

Ohata, K., Naruse, H., Yokokawa, M., Viparelli, E., 2017. New bedform phase diagrams and discriminant functions for formative conditions of bedforms in open-channel flows. J. Geophys. Res. Earth 122, 2139–2158.

Ohata, K., Naruse, H., Izumi, N., 2022. Upper and lower plane bed definitions revised. Prog. Earth Planet Sci. 9, 23.

Ohata, K., de Cala, I., Dorrell, R.M., Naruse, H., et al., 2023. Density stratification controls the bedform phase diagram of saline-gravity currents versus open-channel flows. Sedimentology 70, 1224–1250.

Ollier, G., Cochonat, P., Lénat, J.-F., Labazuy, P., 1998. Deep-sea volcaniclastic sedimentary systems: an example from La Fournaise volcano, Réunion Island, Indian Ocean. Sedimentology 45, 293–330.

Ono, K., Naruse, H., Yao, Q., Cai, Z., Fukuda, S., Yokokawa, M., 2023. Multiple scours and upward fining caused by hydraulic jumps: implications for the recognition of cyclic steps in the deepwater stratigraphic record. J. Sediment. Res. 93 (4), 243–255.

Palan, K., 2017. Submarine Canyon Evolution of the Southwest Cape Continental Margin. Master of Science. University of KwaZulu-Natal, 125p.

Palma, F.I., Bozzano, G., Principi, S., Isola, J.I., Ormazabal, J.P., Esteban, F.D., Tassone, A.A., 2021. Geomorphology and sedimentary processes on the Sloggett canyon, northwestern scotia sea, Argentina. J. S. Am. Earth Sci. 107, 103136.

Parker, G., 2005. 1D sediment transport morphodynamics with applications to rivers and turbidity currents. http://hydrolab.illinois.edu/people/parkerg/morphodynamics_e-book.htm.

Parker, G., Anderson, A.G., 1977. Basic principles of river hydraulics. J. Hydraul. Eng. 103 (9), 1077–1087.

Parker, G., García, M.H., Fukushima, Y., Yu, W., 1987. Experiments on turbidity currents over an erodible bed. J. Hydraul. Res. 25 (1), 123 147.

Parsons, D.R., Best, J.L., Hardy, R.J., Kostaschuk, R., Lane, S.N., Orfeo, O., 2005. Morphology and flow fields of three-dimensional dunes, Rio Paraná, Argentina: results from simultaneous multibeam echo sounding and acoustic Doppler current profiling. J. Geophys. Res. 110 (F4), F04S04. https://doi.org/10.1029/2004JF000231.

Paull, C.K., Ussler, W., Caress, D.W., Lundsten, E., Covault, J.A., Maier, K.L., Xu, J., Augenstein, S., 2010. Origins of large crescent-shaped bedforms within the axial channel of Monterey Canyon, offshore California. Geosphere 6 (6), 755–774.

Paull, C.K., Caress, D.W., Ussler, W., Lundsten, E., Meiner-Johnson, M., 2011. High-resolution bathymetry of the axial channels within Monterey and Soquel submarine canyons, offshore Central California. Geosphere 7 (5), 1077–1101.

Paull, C.K., Caress, D.W., Lundsten, E., Gwiazda, R., Anderson, K., McGann, M., Conrad, J., Edwards, B., Sumner, E.J., 2013. Anatomy of the La Jolla Submarine Canyon system; offshore southern California. Mar. Geol. 335, 16–34.

Piper, D.J.W., Normark, W.R., 2001. Sandy fans—from Amazon to Hueneme and beyond. AAPG Bulletin 85 (8), 1407–1438.

Piper, D.J.W., Savoye, B., 1993. Processes of late Quaternary turbidity current flow and deposition on the Var deep-sea fan, north-West Mediterranean Sea. Sedimentology 40, 557–582.

Piper, D.J.W., Shor, A.N., Farre, J.A., O'Connell, S., Jacobi, R., 1985. Sediment slides and turbidity currents on the Laurentian Fan: Sidescan sonar investigations near the epicenter of the 1929 Grand Banks earthquake. Geology 13, 538–541.

Piper, D.J.W., Shor, A.N., Hughes Clarke, J.E., 1988. The 1929 Grand Banks earthquake, slump and turbidity current. Geol. Soc. Am. Spec. Pap. 229, 77–92.

Pope, E.L., Jutzeler, M., Cartigny, M.J.B., Shreeve, J., Talling, P.J., Wright, I.C., Wysoczanski, R.J., 2018. Origin of spectacular fields of submarine sediment waves around volcanic islands. Earth Planet. Sci. Lett. 493, 12–24.

Porcile, G., Bolla Pittaluga, M., Frascati, A., et al., 2020. Typhoon-induced megarips as triggers of turbidity currents offshore tropical river deltas. Commun. Earth Environ. 1, 2.

Posamentier, H.W., Meizarwin, Wisman, P.S., Plawman, T., 2000. Deep-water depositional systems - ultra-deep Makassar Strait, Indonesia. In: Weimer, P., et al. (Eds.), Deep Reservoirs of the World. GCSSEPM Foundation 20th Annual bob F. Perkins Research Conference, Houston, TX, pp. 806–816.

Praeg, D., Schafer, C.T., 1989. Seabed features of the Labrador slope and rise near 55N revealed by SeaMARC I sidescan sonar imagery. In: Geological Survey of Canada Open File 2028 (28 pp).

Principi, S., Palma, F., Bran, D.M., Bozzano, G., Isola, J.I., Ormazabal, J.P., Esteban, F., Acosta, L., Tassone, A., 2024. Seafloor geomorphology of the northern argentine continental slope at 40-41° S mapped from high-resolution bathymetry. J. S. Am. Earth Sci. 134, 104748.

Raudkivi, A.J., 1997. Ripples on stream bed. J. Hydraul. Eng. ASCE 123 (1), 58–64.

Rebesco, M., Neagu, R.C., Cuppari, A., Muto, F., Accettella, D., Dominici, R., Cova, A., Romano, C., Caburlotto, A., 2009. Morphobathymetric analysis and evidence of submarine mass movements in the western Gulf of Taranto (Calabria margin, Ionian Sea). Int. J. Earth Sci. (Geol Rundsch). https://doi.org/10.1007/s00531-009-0429-1.
Rebesco, M., Hernández-Molina, F.J., Van Rooij, D., Wahlin, A., 2014. Contourites and associated sediments controlled by deep-water circulation processes: State-of-the-art and future Considerations. Mar. Geol. 352, 111–154.
Recking, A., Bacchi, V., Naaim, M., Frey, P., 2009. Antidunes on steep slopes. J. Geophys. Res. 114, F04025. https://doi.org/10.1029/2008JF001216.
Ribó, M., Puig, P. Araceli, Muñoz, A., et al., 2016. Morphobathymetric analysis of the large fine-grained sediment waves over the Gulf of Valencia continental slope (NW Mediterranean). Geomorphology 253, 22–37.
Richards, K.J., 1980. The formation of ripples and dunes on an erodible bed. J. Fluid Mech. 99, 597–618.
Russo, S., Bourget, J., Mulder, T., 2024. Giant sediment wave fields adjacent to debris-flow filled deep sea valleys: New evidence of cohesive flows transforming into dilute turbidity currents. Mar. Geol. 473, 107305.
Sacchi, M., Insinga, D., Milia, A., Molisso, F., Raspini, A., Torrente, M.M., Conforti, A., 2005. Stratigraphic signature of the Vesuvius 79 AD event off the Sarno prodelta system, Naples Bay. Mar. Geol. 222–223, 443–469.
Saint-Ange, F., Bachèlery, P., Babonneau, N., Michon, L., Jorry, S.J., 2013. Volcaniclastic sedimentation on the submarine slopes of a basaltic hotspot volcano: Piton de la Fournaise volcano (La Réunion Island, Indian Ocean). Mar. Geol. 337, 35–52.
Sanders, S., Jafarinik, S., Hernández Moreira, R., Johnson, R., Balkus, A., Ahmadpoor, M., et al., 2023. Influence of sand supply and grain size on equilibrium upper regime bedforms. J. Geophys. Res. Earth 128. https://doi.org/10.5061/dryad.tdz08kq2j e2022JF006820. Associated dataset Dryad:
Santos, R., Quartau, R., Brum da Silveira, A., et al., 2019. Gravitational, erosional, sedimentary and volcanic processes on the submarine environment of Selvagens Islands (Madeira Archipelago, Portugal). Mar. Geol. 415, 105945.
Schattner, U., Lazar, M., 2016. Hierarchy of source-to-sink systems—example from the Nile distribution across the eastern Mediterranean. Sediment. Geol. 343, 119–131.
Schindler, R.J., Robert, A., 2004. Suspended sediment concentration and the ripple-dune transition. Hydrol. Process. 18, 3215–3227.
Schindler, R.J., Robert, A., 2005. Flow and turbulence structure across the ripple-dune transition: an experiment under mobile bed conditions. Sedimentology 52. https://doi.org/10.1111/j.1365-3091.2005.00706x.
Schnyder, J.S.D., Eberli, G.P., Betzler, C., Wunsch, M., Lindhorst, S., Schiebel, L., Mulder, T., Ducassou, E., 2018. Morphometric analysis of plunge pools and sediment wave fields along western Great Bahama Bank. Mar. Geol. 397, 15–28.
Sequeiros, O.E., 2012. Estimating turbidity current conditions from channel morphology: a Froude number approach. J. Geophys. Res. 117, C04003.
Sequeiros, O.E., Spinewine, B., García, M.H., Beaubouef, R.T., Sun, T., Parker, G., 2009. Experiments on wedge-shaped deep sea sedimentary deposits in minibasins and/or on channel levees emplaced by turbidity currents. Part I. Documentation of the flow. J. Sediment. Res. 79 (7–8), 593–607.
Sequeiros, O.E., Spinewine, B., Beaubouef, R.T., Sun, T., García, M.H., Parker, G., 2010a. Characteristics of velocity and excess density profiles of saline underflows and turbidity currents flowing over a mobile bed. J. Hydraul. Eng. 136 (7).
Sequeiros, O.E., Spinewine, B., Beaubouef, R.T., Sun, T., García, M.H., Parker, G., 2010b. Bedload transport and bed resistance associated with density and turbidity currents. Mar. Geol. 57 (1463–1490), 2010.
Sequeiros, O.E., Mosquera, R.L., Pedocchi, F., 2018. Internal structure of a self-accelerating turbidity current. J. Geophys. Res. Oceans 123.
Sequeiros, O.E., Bolla Pittaluga, M., Frascati, A., Pirmez, C., Masson, D.G., Weaver, P., Crosby, A.R., Lazzaro, G., Botter, G., Rimmer, J.G., 2019. How typhoons trigger turbidity currents in submarine canyons. Sci. Rep. 9, 9220.
Shields, A., 1936. Anwendung der Aehnlichkeitsmechanik und der Turbulenzforschung auf die Geschiebebewegung. In: Mitteilungen der Preußischen Versuchsanstalt für Wasserbau (in German), vol. 26. Preußische Versuchsanstalt für Wasserbau, Berlin.
Shorrock, A.E., Strachan, L.J., Barnes, P.M., et al., 2025. Coeval transverse and axial sediment delivery to the Northern Hikurangi trough during the late quaternary. Basin Res. 37, e70019.
Simons, D.B., Richardson, E.V., 1966. Resistance to Flow in Alluvial Channels, Professional Paper 422J. U.S. Geological Survey, Washington, D.C.
Sisavath, E., Babonneau, N., Saint-Ange, F., Bachèlery, P., Jorry, S.J., Deplus, C., De Voogd, B., Savoye, B., 2011. Morphology and sedimentary architecture of a modern volcaniclastic turbidite system: the Cilaos fan, offshore La Réunion Island. Mar. Geol. 288 (1), 1–17.
Slootman, A., Cartigny, M.J.B., 2020. Cyclic steps: review and aggradation-based classification. Earth Sci. Rev. 201.
Slootman, A., Vellinga, A.J., Moscariello, A., Cartigny, M.J.B., 2021. The depositional signature of high-aggradation chute-and-pool bedforms: the build-and-fill structure. Sedimentology 2021 (68), 1640–1673.
Smith, D., Kvitek, R., Iampietro, P., Wong, K., 2007. Twenty-nine months of geomorphic change in upper Monterey Canyon (2002–2005). Mar.Geol. 236 (1–2), 79–94.
Smith, M.E., Werner, S.H., Buscombe, D., Finnegan, N.J., Sumner, E.J. and Mueller, E.R. 2018. Seeking the shore: evidence for active submarine canyon head incision due to coarse sediment supply and focusing of wave energy. Geophys. Res. Lett., 45, 12,403–12,413.
Sorokin, V.M., Roslyakov, A.G., 2019. The structure and composition of sediment waves in the Middle Caspian Sea. Mosc. Univ. Geol. Bull. 74 (2), 197–205.
Southard, J.B., Boguchwal, L.A., 1990. Bed configurations in steady unidirectional water flows. Part 2. Synthesis of flume data. J. Sediment. Petrol. 60 (5), 658–679.
Spinewine, B., Sequeiros, O.E., García, M.H., Beaubouef, R.T., Sun, T., Savoye, B., Parker, G., 2009. Experiments on wedge-shaped deep sea sedimentary deposits in minibasins and/or on channel levees emplaced by turbidity currents. Part II. Morphodynamic evolution of the wedge and of the associated bedforms. J. Sediment. Res. 79 (7–8), 608–628.
Spinewine, B., Sequeiros, O.E., Sun, T., Parker, G., 2010. Experiments and analytical solution for a prograding wedge-shaped deposit produced by turbidity currents transporting gravel mixtures, River. In: Vionnet, et al. (Eds.), Coastal and Estuarine Morphodynamics: RCEM 2009, 1. Taylor & Francis Group, London, pp. 249–255. ISBN 978-0-415-55426-8.
Stacey, M.W., Bowen, A.J., 1988. The vertical structure of turbidity currents and a necessary condition for self-maintenance. J. Geophys. Res. 93 (C4), 3543–3553.
Stacey, C.D., Hill, P.R., Talling, P.J., Enkin, R.J., Hughes Clarke, J.E., 2019. How turbidity current frequency and character varies down a Fjord-delta system: combining direct monitoring, deposits and seismic data. Sedimentology 66, 1–31.
Straub, K.M., Mohrig, D., McElroy, B., Buttles, J., Pirmez, C., 2008. Interactions between turbidity currents and topography in aggrading sinuous submarine channels: a laboratory study. Geol. Soc. Am. Bull. 120, 368–385.
Sun, Y., Wang, D., Canals, M., Alves, T.M., Wang, W., Zhu, Y., Qin, Y., Zeng, F., Zheng, Y., 2023. Bedform evolution along a submarine canyon in the South China Sea: new insights from an autonomous underwater vehicle survey. Sedimentology. https://doi.org/10.1111/sed.13152. Online Version of Record before inclusion in an issue.
Symons, W.O., Sumner, E.J., Talling, P.J., Cartigny, M.J.B., Clare, M.A., 2016. Large-scale sediment waves and scours on the modern seafloor and their implications for the prevalence of supercritical flows. Mar. Geol. 371, 130–148.
Taki, K., Parker, G., 2005. Transportational cyclic steps created by flow over an erodible bed. Part 1. Experiments. J. Hydraul. Res. 43 (5), 488–501.
Talling, P.J., Cartigny, M.J.B., Pope, E., et al., 2023. Detailed monitoring reveals the nature of submarine turbidity currents. Nat. Rev. Earth Environ. 4, 642–658.
Tek, D.E., McArthur, A.D., Poyatos-Moré, M., et al., 2022. Controls on the architectural evolution of deep-water channel overbank sediment wave fields: insights from the Hikurangi channel, Offshore New Zealand. N. Z. J. Geol. Geophys. 65 (1), 141–178.
Trincardi, F., Normark, W.R., 1988. Sediment waves on the Tiber Prodelta slope: interaction of deltaic sedimentation and currents along the shelf. Geo-Mar. Lett. 1988 (8), 149–157.
Tubau, X., Paull, C.K., Lastras, G., et al., 2015. Submarine canyons of Santa Monica Bay, Southern California: Variability in morphology and sedimentary processes. Mar. Geol. 365, 61–79.
Tzevahirtzian, A., Zaragosi, S., Bachèlery, P., Biscara, L., Marchès, E., 2021. Submarine morphology of the Comoros volcanic archipelago. Mar. Geol. 432, 106383.
Urgeles, R., Cattaneo, A., Puig, P., Liquete, C., De Mol, B., Amblas, D., Sultan, N., Trincardi, F., 2011. A review of undulated sediment features on Mediterranean prodeltas: distinguishing sediment transport structures from sediment deformation. Mar. Geophys. Res. 32, 49–69.
van den Berg, J.H., van Gelder, A., 1993. A new bedform stability diagram, with emphasis on the transition of ripples to plane bed in flows over fine sand and silt. Spec. Publ. Int. Assoc. Sedimentol. 17, 11–21.
van Landeghem, K.J.J., Baas, J.H., Mitchell, N.C., Wilcockson, D., Wheeler, A.J., 2012. Reversed sediment wave migration in the Irish Sea, NW Europe: a reappraisal of the validity of geometry-based predictive modelling and assumptions. Mar. Geol. 295–298, 95–112.
van Rijn, L.C., 1984. Sediment transport, Part II: suspended load transport. J. Hydraul. Eng. 110 (11), 1613–1641.
Vanoni, V.A., 1974. Factors determining bed form of alluvial streams. J. Hydraul. Eng. ASCE 100 (HY3), 363–378.
Vanoni, V.A., 1975. Discussion. Factors determining bed form of alluvial streams. J. Hydraul. Div. 101 (HY11), 1435–1440.
von Lom-Keil, H., Spieß, V., Hopfauf, V., 2002. Fine-grained sediment waves on the western flank of the Zapiola Drift, Argentine Basin: evidence for variations in late Quaternary bottom flow activity. Mar. Geol. 192, 239–258.
Wang, B., Zhong, G., Wang, L., Hu, P., Cartigny, M.J., Li, Y., Kuang, Z., 2025. Downslope transition of supercritical turbidity-current bedforms linked to minimal slope changes in the South China Sea abyssal plain. Sedimentology Submitted. ID: 6024e883-4b2a-4fa0-9124-f1ed1c7daea5.
Warnke, F., Schwenk, T., Miramontes, E., Spiess, V., Wenau, S., Bozzano, G., Baqués, M., Kasten, S., 2023. Evolution of complex giant seafloor depressions at the northern Argentine continental margin (SW Atlantic Ocean) under the influence of a dynamic bottom current regime. Front. Earth Sci. 11, 1117013.
West, L.M., Perillo, M.M., Olariu, C., Steel, R.J., 2019. Multi-event organization of Deepwater sediments into bedforms: Long-lived, large-scale antidunes preserved in Deepwater slopes. Geology 47, 391–394.
Wieprecht, S., 2001. Entstehung und Verhalten von Transportkorpern bei grobem Sohlenmaterial. Universitat der Bundeswehr Munchen, Institut fur Wasserwesen, Mitteilungen Heft 75/2001. Oldenbourg Verlag, 153 pp (in German).
Wolfson-Schwehr, M., Paull, C.K., Caress, D.W., Gwiazda, R., Nieminski, N.M., Talling, P. J., et al., 2023. Time-lapse Seafloor surveys reveal how turbidity currents and internal tides in Monterey Canyon interact with the seabed at centimeter-scale. J. Geophys. Res. Earth 128. https://doi.org/10.1029/2022JF006705 e2022JF006705.
Wunsch, M., Betzler, C., Lindhorst, S., Lüdmann, T., Eberli, G.P., 2017. Sedimentary dynamics along carbonate slopes (Bahamas archipelago). Sedimentology 64 (3), 631–657.
Wynn, R.B., Stow, D.A.V., 2002. Classification and characterization of deep-water sediment waves. Mar. Geol. 192, 7–22.
Wynn, R.B., Masson, D.G., Stow, D.A.V., Weaver, P.P.E., 2000a. Turbidity current sediment waves on the submarine slopes of the western Canary Islands. Mar. Geol. 163, 185–198.

Wynn, R.B., Weaver, P.P.E., Ercilla, G., Stow, D.A.V., Masson, D.G., 2000b. Sedimentary processes in the Selvage sediment-wave field, NE Atlantic: new insights into the formation of sediment waves by turbidity currents. Sedimentology 47, 1181–1197.

Wynn, R.B., Piper, D.J.W., Gee, M.J.R., 2002. Generation and migration of coarse-grained sediment waves in turbidity current channels and channel-lobe transition zones. Mar. Geol. 192, 59–78.

Xu, J.P., 2010. Normalized velocity profiles of field-measured turbidity currents. Geology 38 (6), 563–566.

Xu, J.P., Noble, M.A., Rosenfeld, L.K., 2004. In-situ measurements of velocity structure within turbidity currents. Geophys. Res. Lett. 31, L09311. https://doi.org/10.1029/2004GL019718.

Xu, J.P., Wong, F.L., Kvitek, R., Smith, D.P., Paull, C.K., 2008. Sandwave migration in Monterey Submarine Canyon, Central California. Mar. Geol. 248, 193–212.

Xu, J.P., Sequeiros, O.E., Noble, M.A., 2014. Sediment concentrations, flow conditions, and downstream evolution of two turbidity currents, Monterey Canyon, USA. Deep-Sea Res. I 89, 11–34.

Yalin, M.S., 1964. Geometrical properties of sand waves. J. Hydraul. Eng. ASCE 90 (5), 05–119.

Yalin, M.S., 1965. Closure to discussion of Geometrical properties of sand waves. J. Hydraul. Eng. ASCE 91 (5), 184–190.

Yokokawa, M., Okuno, K., Nakamura, A., Muto, T., Miyata, Y., Naruse, H., 2009. Aggradational cyclic steps: Sedimentary structures found in flume experiments. In: Proceedings, 33rd IAHR Congress: Water Engineering for a Sustainable Environment, 2009 by International Association of Hydraulic Engineering & Research (IAHR), pp. 5547–5554. ISBN: 978-94-90365-01-1.

Yokokawa, M., Takahashi, Y., Yamamura, H., Kishima, Y., Parker, G., Izumi, N., 2011a. Phase diagram for antidunes and cyclic steps based on suspension index, non-dimensional Chezy resistance coefficient and Froude number. In: Proceedings, River, Coastal and Estuarine Morphodynamics: RCEM2011. Tsinghua University Press, Beijing, pp. 1789–1794.

Yokokawa, M., Tsuji, A., Kishimoto, K., Mizokami, Y., Murokawa, T., Muraoka, S., Naruse, H., 2011b. Bedform existence diagrams for open channel flow: Lightweight plastic versus quartz. American Geophysical Union, Fall Meeting 2011, Abstract id. EP23A-0726.

Zanke, U., 1976. On the Effect of Bed material, Currents and Water Depth on the Parameters of Ripples and Dunes in Open Channels, vol. 44. Mitt. des Franzius-Instituts der TU Hannover, Hannoverm, Germany (In German).

Zanke, U., Roland, A., 2021. On ripples—a boundary layer-theoretical definition. Water 13, 892. https://doi.org/10.3390/w13070892.

Zeng, J., Lowe, D.R., Prior, D.B., Wiseman, W.J., Bornhold, B.D., 1991. Flow properties of turbidity currents in Bute Inlet, British Columbia. Sedimentology 38 (6), 975–996.

Zhang, S., Zhu, J., Jia, Y., Li, S., Chen, R., Chen, X., Ou, X., Li, Q., 2022. Submarine small-scale features of cyclic steps in the Penghu Canyon: implications for the migration of Canyon. J Mar Sci Eng 10, 1301.

Zhang, H., Zhong, G., Zhang, L., Wang, B., Lei, Z., Guan, Y., Yao, Y., 2024. The Guangya submarine fan in the South China Sea: a distinctive channelized slope-through fan. Geomorphology 452, 109116.

Zhong, G., 2025. Supercritical turbidity-current bedforms and associated morphologies in the South China Sea. Sci. Bull. https://doi.org/10.1016/j.scib.2025.04.007.

Zhong, G., Cartigny, M.J.B., Kuang, Z., Wang, L., 2015. Cyclic steps along the South Taiwan Shoal and West Penghu submarine canyons on the northeastern continental slope of the South China Sea. GSA Bull. 127 (5/6), 804–824.

Zhou, W., Chiarella, D., Zhuo, H., Wang, Y., Tang, W., Zou, M., Xu, Q., 2021. Genesis and evolution of large-scale sediment waves in submarine canyons since the Penultimate Glacial Maximum (ca. 140 ka), northern South China Sea margin. Mar. Pet. Geol. 134, 105381.